UNIVERSITÀ DI MODENA E REGGIO EMILIA
DEPARTMENT OF SCIENCES AND METHODS FOR ENGINEERING

DOCTORAL THESIS IN
INDUSTRIAL INNOVATION ENGINEERING
XXXIII CYCLE

Development and engineering of printed piezoelectric microphones

---

Candidate:
Yuri RICCI

Advisor:
Prof. Giovanni VERZELLESI

Co-Advisor:
Prof. Luca LARCHER

Director of the School:
Prof. Franco ZAMBONELLI

Thesis submitted in fulfillment of the requirements
for the degree of Doctor of Philosophy

UNIVERSITÀ DI MODENA E REGGIO EMILIA
Department of Sciences and Methods for Engineering

Abstract

Doctor of Philosophy

Development and engineering of printed piezoelectric microphones

by Yuri RICCI

This thesis presents a study of piezoelectric (PE) microphones fabricated using 3D-printing. The study was conducted as part of a project of industrial interest, motivated by the advantages of printing techniques over traditional manufacturing methods, namely low cost, high flexibility, and throughput. The exploratory research regarding the advantages and limitations of printing techniques for piezoelectric microphone development resulted in an architecture exploiting a pillar-based design concept. The design is refined according to equivalent multiphysics models and Finite Element Method (FEM) simulations, in order to provide competitive performance in terms of sensitivity, bandwidth, or both. When possible, validation is performed with experimental measurements on fabricated prototypes.

The proposed design implements a known sensitivity enhancement strategy, involving both a pillar-based mechanical structure and the electrode patterning of the piezoelectric film. A PE microphone with a single pillar is designed for 3D-printing. The mechanical parts of the sensor are printed as a single element, allowing for simple device fabrication. An original study is conducted to analyze the acoustic propagation in the microphone annular aperture and derive an equivalent circuit model. Then, a complete multiphysics model of the microphone is developed and validated, providing a useful tool for further technological development. A laser-trimmed prototype is fabricated as a result of the engineering process. The sensor is characterized by appreciable sensitivity and bandwidth and is among the first working examples of 3D-printed PE microphones.

UNIVERSITÀ DI MODENA E REGGIO EMILIA
Dipartimento di Scienze e Metodi dell'Ingegneria

Sommario

Dottorato di Ricerca

Sviluppo e ingegnerizzazione di microfoni piezoelettrici stampati

di Yuri RICCI

Questa tesi presenta uno studio di microfoni piezoelettrici (PE) fabbricati con tecniche di stampa 3D. Lo studio è stato condotto nell'ambito di un progetto di interesse industriale, motivato dai vantaggi delle tecniche di stampa rispetto ai metodi di produzione tradizionali, quali basso costo, alta flessibilità e produttività. La ricerca esplorativa in merito ai vantaggi e ai limiti delle tecniche di stampa per lo sviluppo di microfoni piezoelettrici ha dato origine ad una architettura che sfrutta un design concettuale basato su una struttura a pilastri. La progettazione è stata perfezionata mediante modelli multifisici equivalenti e simulazioni con il metodo degli elementi finiti (FEM), al fine di fornire prestazioni competitive in termini di sensibilità, larghezza di banda o entrambi. Quando possibile, la convalida è stata eseguita con misurazioni sperimentali sui prototipi fabbricati.

Il design proposto implementa una nota strategia di miglioramento della sensibilità che coinvolge sia una struttura meccanica a pilastri che la sagomatura degli elettrodi del film piezoelettrico. E' stato progettato un microfono PE con un singolo pilastro per la stampa 3D. Le parti meccaniche del sensore sono stampate in un unico elemento, consentendo una fabbricazione semplificata dello stesso. E' stato condotto uno studio originale per analizzare la propagazione acustica nell'apertura anulare del microfono e derivare un modello circuitale equivalente. Quindi, è stato sviluppato e validato un modello multifisico completo del microfono, fornendo un utile strumento per un ulteriore sviluppo tecnologico. Il processo di ingegnerizzazione ha portato alla fabbricazione di un prototipo tagliato al laser. Il sensore è caratterizzato da sensibilità e larghezza di banda apprezzabili, collocandosi tra i primi esempi funzionanti di microfono PE stampato in 3D.

Contents

List of Figures

List of Tables

Introduction

A microphone is an electroacoustic transducer able to convert acoustic energy (i.e. sound) into electric energy (i.e. voltage). Microphones are employed in many sensing applications, owing to the ability of acoustic waves to propagate in different elastic media (i.e. gas, liquid and solid) and over a wide range of frequencies, extending beyond the audible spectrum. Typical applications include telephony, hearing aids, Public-Address (PA) systems, underwater acoustics, medical ultrasound, body vibrations pickup (i.e. musical instruments) and acoustic field measurements. Microphones are thus diversified and specialized, to account for the broad range of available applications, each characterized by its own requirements.

Microphones for airborne sound can be classified according to the type of electromechanical transduction and the fabrication technology. The most prominent types of electromechanical transduction mechanisms adopted for microphone development are the electromagnetic transduction, the electrostatic transduction and the piezoelectric transduction. Each transduction principle is adopted by many distinct microphone designs, fabricated according to different technologies, both at the macroscale and the microscale. In the following, for each transduction mechanism, the prominent microphone solutions are described.

Microphones adopting the electromagnetic transduction principle exploit the voltage signal generated across the two ends of a conductor, which vibrates within the fixed magnetic field of a permanent magnet. According to electromagnetic induction, the generated voltage is proportional to the velocity of the conductor itself. The conductor is put into motion by the acoustic wave, either directly or indirectly. In the latter case, an additional mechanical element is interposed for motion transmission (e.g. diaphragm). The dynamic microphone is the most prominent exponent of this category.

The dynamic microphone is constituted by a coil of wire, inserted between the magnetic poles of a permanent magnet, and rigidly connected to a diaphragm exposed to the acoustic field. The acoustic stimulus makes the diaphragm and the coil to vibrate as a rigid body. Dynamic microphones are robust, moderately cheap and resistant to contaminants, like moisture. Moreover, they do not require a power supply or battery for operation. For these reasons, they represent the ideal solution for applications in which versatility and sturdiness are desirable, such as for on-stage use in live concerts. Nevertheless, they are typically not accurate and sensitive as other solutions, such as condenser microphones. The presence of a permanent magnet and a coil of wire makes them bulky and prevents miniaturization. Finally, they are characterized by a complex structure, which translates in a delicate and convoluted manufacturing process.

Microphones adopting the electrostatic transduction principle exploit a variable capacitor as their core element. For this reason, they are often called condenser microphones. In its simplest form, a condenser microphone is constituted by a thin metallic diaphragm and a fixed back-plate, separated by a short distance. The two elements

are electrically insulated and constitute the two plates of the variable capacitor. During operation, the acoustic wave causes a displacement of the diaphragm from its rest position, modulating the distance from the back-plate. The microphone is generally polarized with a fixed DC bias voltage, with guarantees an almost constant electric charge on the armatures during operation. Hence, the varying distance causes a modulation of the electrical capacitance and the open-circuit output voltage.

Condenser microphones are characterized by high sensitivity and large operating bandwidth. For this reason, they are used extensively as measuring instruments of sound pressure (e.g. sound level meters) and as studio microphones for high-fidelity music pickup. Moreover, they can be sufficiently small so as to not disturb the sound field during the measurement. Condenser microphones are however rather expensive, particularly in the high-end sector. They also need a power source for both the capacitor polarization and the signal conditioning circuitry. Finally, the are quite delicate and prone to failures.

The electret condenser microphone (ECM) is a type of condenser microphone in which the constant electric charge, necessary for a proper device operation, is provided by a permanently charged polymer, known as electret. Traditional ECM microphones adopt an electret foil as the acoustic diaphragm itself. In more advanced designs, the functions of the electret and the diaphragm are separated, and the electret is inserted either below the diaphragm or over the back-plate. In this case, a thin metallic diaphragm is usually employed, which guarantees superior mechanical characteristics.

Traditional ECM microphones are easy to manufacture, cheap, and characterized by appreciable performance. For this reason, they are widely used in consumer electronics devices, such as cell-phones, computers, headsets and small recording tools. Advanced solutions are suitable for high-end applications, such as measuring instruments. Electret microphones do not require polarization and, for this reason, are often labeled as "prepolarized". Nevertheless, they still need a power source for the signal conditioning circuitry.

The Micro-Electro-Mechanical-System (MEMS) capacitive microphone is the micro-scale version of the conventional condenser microphone. MEMS microphones are realized according to lithographic methods, similar to those adopted for the fabrication of integrated circuits. As a result, complete microphones with a size of a few millimeters squared can be easily attained. The revolutionary aspect of MEMS microphones lies more on the fabrication process rather than the operating principle. However, strong research efforts in this direction led to significant evolutions also from an architectural perspective, such as the double diaphragm configuration for differential readout and noise floor reduction [1].

MEMS capacitive microphones represent a mature technology, offering high sensitivity, low noise levels, flat frequency response and environmental stability. Moreover, MEMS microphones are very small and indicated for space-limited applications. They are appealing to many fields, including the industrial, medical and automotive sectors. They also find application in consumer electronics, where they are increasingly competing with ECMs. Nevertheless, micro-scale manufacturing is a complex and expensive process. Cost mitigation requires high production volumes, with a large number of sensors for each silicon wafer.

Microphones adopting the piezoelectric transduction principle exploit the natural

capability of a special class of materials, called piezoelectric materials, to convert mechanical energy into electrical energy and vice versa. The generation of an electric charge under the application of a mechanical stress is known, in particular, as direct piezoelectric effect. The converse piezoelectric effect consists in the generation of an internal mechanical stress under the application of an electric field. The direct piezoelectric effect is thus suitable for sensors, including microphones, while the converse piezoelectric effect is indicated for actuators, such as loudspeakers.

Piezoelectric microphones for airborne sound experienced several major evolutionary steps in almost a century. Early piezoelectric microphones were constituted by a diaphragm exposed to the acoustic field and mechanically connected to the piezoelectric element on the back side. The predominant piezoelectric element was a rochelle salt crystal, hence the common name of crystal microphones [2], [3]. Unfortunately, crystal microphones are delicate, sensitive to humidity and temperature, and characterized by a poor frequency response. For these reasons, they could not rival with dynamic or condenser microphones and rapidly disappeared from the market. A breakthrough in the construction of piezoelectric microphones was the discovery of synthetic piezoelectric polymers, especially of polyvinylidene fluoride (PVDF) [4], [5]. Starting from the late sixties, microphones with curved piezoelectric films started to be investigated [6]–[8]. The curved film implements the functions of both the membrane and the transducer. The curvature imposed on the piezoelectric membrane allows preserving the phase correspondence between the sound wave and the electrical signal, avoiding signal distortions.

Only recently, however, the integration of piezoelectric materials with MEMS fabrication accelerated considerably the development of the technology, leading also to competitive market solutions. The typical design consists of a small and thin vibrating membrane, constituted by a piezoelectric film sandwiched between electrodes and backed by an additional supporting layer [9]–[11]. More elaborated solutions include composite diaphragms with multiple layers [12] and piezoelectric films in cantilever configuration [13]. Piezoelectric materials compatible with MEMS fabrication include lead zirconium titanate (PZT), zinc oxide (ZnO) and aluminum nitride (AlN).

Piezoelectric microphones of new generation are rugged, dustproof and waterproof, with very low power requirements and a wide dynamic range. The main drawbacks are still represented by the limited sensitivity and signal-to-noise ratio, although the performance gap with competing technologies is constantly reducing. They mainly represent a valid alternative to condenser microphones for targeted applications. Piezoelectric solutions can be advantageous when reliability is critical, such as for microphone arrays. Condenser microphones, on the contrary, are sensitive to environmental contaminants, such as water and dust. Piezoelectric microphones can generally withstand very high pressure levels, while capacitive microphones are limited by design and may incur in membrane failures or collapses towards the back-plate. Finally, piezoelectric microphones do not need a polarization voltage. MEMS piezoelectric microphones represent an emerging technology able to compete with other established solutions, as demonstrated by novel commercial products like the Vesper suite [13]. However, as already mentioned previously, MEMS fabrication relies on expensive semiconductor lithography equipment, which demands for significant production volumes for cost mitigation. The development chain is also negatively affected. A limited number of carefully

planned redesigns can be considered, due to the cost of every process run [14]. Moreover, each development cycle can last weeks or even months.

Emerging 3D-printing and electronic printing techniques represent a viable alternative to the described rigid production scheme, allowing for the flexible and rapid development of novel, low-cost sensors. In addition, the rapid prototyping allows for the effective exploration of alternative custom designs, facilitating the entire development from the conception to the final product.

Three-dimensional (3D) printing comprises a family of techniques for the additive fabrication of 3D objects, in a layer-by-layer fashion. Compared to traditional manufacturing, subtractive in nature, 3D-printing is cheap, fast, and efficient, both in terms of energy consumption and processing of raw materials, with minimal wastes [15]. In recent years, several 3D-printing methods have emerged, based on different fabrication strategies such as material extrusion, photocuring, powder bed fusion and sheet lamination. Thermoplastics are the traditional and still most common 3D-printed materials, including Nylon and ABS. Recently, however, the compatibility has been extended also to metals, ceramics and composites. 3D-printing technologies have been successfully adopted for the design and fabrication of many different devices, particularly in the sensors field, including force [16] and pressure sensors [17], radiofrequency LC-tank sensors [18] and antennas [19]. Notable implementations related to the acoustic domain include a capacitive acoustic resonator [20], a thick membrane for low-frequency sound absorption [21] and the additive manufacturing of ceramic components with piezoelectric properties, demonstrated through sound generation in the MHz range [22]. A 3D-printed piezoelectric microphone has been recently designed [23]. A high-resolution 3D-printer has been adopted for the realization of a suspended piezoelectric membrane, similarly to MEMS-based designs. Unfortunately, only a proper mechanical characterization of the sensor is provided.

Thesis organization

This thesis presents a study of piezoelectric microphones fabricated according to 3D-printing techniques. The thesis is organized as follows:

The first chapter discusses the design of a novel 3D-printed piezoelectric microphone. The design involves both a pillar-based mechanical structure and the electrode patterning of the adopted piezoelectric film, matching the pillars geometry. The combination of these two design features improves the voltage sensitivity of the device, as demonstrated by [24]. The mechanical parts of the sensor are designed to be printed as a single element, allowing for a simple device realization, as published in [25].

The second chapter presents an original study of the thermoviscous acoustic propagation in annular waveguides [26]. The study is aimed at analyzing the acoustic behavior within the annular aperture of the proposed design (i.e. vent). The work culminates in the definition of a simple circuit model with lumped elements. The circuit can be adopted to speed up and simplify the analysis and engineering of devices having annular structural elements, including the proposed microphone.

The third chapter presents a multiphysics lumped-element model of the proposed microphone, coupling the acoustic, mechanical and electrical domains through circuit

analogies. The end result is an efficient and insightful model, useful for device tuning and optimization. The realized model is finally validated against finite-element-method (FEM) simulations.

The fourth chapter describes the fabrication and acoustic characterization of a single-pillar 3D-printed microphone trimmed by laser cutting. The prototype implements the insights obtained from the developed model, concerning in particular the annular aperture. The resulting microphone represents one of the first working examples of 3D-printed piezoelectric microphones with end-to-end characterization, as published in [27]. The analysis is completed with further experimental validation, demonstrating the importance of the aperture size on the resulting performance.

Original contributions and publications

A punctual description of the core original contributions of this thesis work, in order of appearance, is summarized in the following:

1. The design and practical feasibility evaluation of a novel 3D-printed pillar-based piezoelectric microphone (section 1.4.2). The work is published in the following conference proceeding [25]:

   A. Sorrentino, Y. Ricci, D. Castagnetti, and L. Larcher, "Design, prototyping and validation of a new PVDF acoustic sensor," in *Proceedings of 30th International Conference on Adaptive Structures and Technologies, ICAST 2019*, 2019, pp. 71–72

2. The demonstration of the approximation validity of the annular acoustic waveguide with the rectangular layers waveguide, assuming thermoviscous propagation (section 2.2.3).

3. The original derivation and validation of a lumped-element circuit model describing the thermoviscous acoustic wave propagation in waveguides having annular cross-section (section 2.3.2).

   The work in 2 and 3 is currently submitted in a regular journal article [26]:

   Y. Ricci, P. La Torraca, and L. Larcher, "Circuit model for thermoviscous propagation in annular waveguides," *SUBMITTED TO: Journal of the Acoustical Society of America (Status: Accept subject to minor revisions)*, 2021

4. The derivation of an effective piezoelectric coefficient for orthotropic thin films in clamped conditions (section 3.3.2).

5. The original derivation and validation of a complete multiphysics circuit model of the microphone (section 3.4). The circuit model is derived starting from both original component circuit models ("vent", see chapter 2) and fundamental well-known component models.

6. The fabrication and acoustic characterization of a working single-pillar 3D-printed microphone, trimmed by laser cutting. The work is published in a regular journal article [27]:

Y. Ricci, A. Sorrentino, P. La Torraca, L. Cattani, M. Cotogno, G. Cantarella, L. Orazi, D. Castagnetti, P. Lugli, and L. Larcher, "Design and Fabrication of a Pillar-Based Piezoelectric Microphone Exploiting 3D-Printing Technology," *IEEE Sensors Letters*, vol. 5, no. 2, pp. 1–4, Feb. 2021, ISSN: 2475-1472. DOI: 10.1109/LSENS.2021.3053209

Chapter 1

Design of 3D-Printed Piezoelectric Microphone

Lee In this chapter, the pillar-based piezoelectric microphone design for 3D-printing is described and motivated. First, the technological framework is defined, including the analysis of piezoelectric materials, 3D-printing fabrication techniques and prominent piezoelectric microphone architectures. Next, the aforementioned technologies are discussed, resulting in a motivated selection suitable for 3D-printing fabrication. Finally, a proper design is established.

1.1 Piezoelectricity

The piezoelectric effect is the ability of piezoelectric materials to convert mechanical energy into electrical energy and vice versa. The generation of an electric charge under the application of a mechanical stress is known as direct piezoelectric effect. The converse phenomenon, consisting in the generation of an internal mechanical stress under the application of an electric field, is known as inverse piezoelectric effect.

Piezoelectric materials are a special class of dielectric materials which can be additionally polarized through the application of a mechanical stress [28]. The piezoelectric effect is strongly coupled to the material crystal structure. Almost all materials having a crystal structure without a center of symmetry (i.e. noncentrosymmetric) exhibit piezoelectricity. Of the 32 existing crystal classes, 21 are noncentrosymmetric, 20 of which exhibit piezoelectricity [29].

A further classification can be made between non polar and polar piezoelectric materials. Non polar piezoelectrics are characterized by randomly oriented dipole moments, with a null total moment. In this case, the application of a mechanical stress causes the separation of the positive and negative centers of the crystal, creating a net polarization. Polar piezoelectrics exhibit a net dipole moment in the absence of mechanical stimuli. In addition, they show pyroelectricity, consisting in the ability to generate an electric field upon application of a temperature gradient.

Ferroelectrics are a class of polar piezoelectric materials in which the spontaneous polarization can be permanently modified upon application of an external electric field. The acquired polarization state is then maintained when the electric field is removed.

The polarization of ferroelectrics by means of a strong electric field is often required to activate a meaningful piezoelectric effect. Many ferroelectric materials are not monocrystalline, meaning that they do not show a uniform polarization with a single

orientation. Instead, they are characterized by local polarization regions, or domains, oriented toward different directions. The reorientation of the polarization domains is performed through a process known as poling, consisting in the application of a strong electric field.

1.1.1 Constitutive equations

The constitutive equations of linear piezoelectric materials can be expressed in several related forms. The most commonly adopted is the "strain-voltage" form, which can be written according to Einstein notation as [30]:

$$D_i = d_{im}\sigma_m + e^{\sigma}_{ij}E_j \tag{1.1}$$

$$\varepsilon_k = s^{E}_{km}\sigma_m + d_{jk}E_j \tag{1.2}$$

in which $i, j = 1..3$ and $m, k = 1..6$. In the equations, D_i are the 3 electric displacement components, d_{im} are the 18 piezoelectric coefficients in "strain-voltage" form (i.e. strain constants), σ_m are the 6 mechanical stress components, e_{ij} are the 6 electrical permittivity components, E_j are the 3 electric field components, ε_k are the 6 mechanical strain components and s_{km} are the 36 elastic compliance components. The superscripts σ and E indicate that the given quantity is measured at constant stress and electric field, respectively. The piezoelectric coefficients d implement the transduction between the mechanical and the electrical domains.

The constitutive equations can be also conveniently expressed in matrix form as:

$$\begin{bmatrix} \boldsymbol{D} \\ \boldsymbol{\varepsilon} \end{bmatrix} = \begin{bmatrix} \boldsymbol{d} & \boldsymbol{e^{\sigma}} \\ \boldsymbol{s^{E}} & \boldsymbol{d^{T}} \end{bmatrix} \begin{bmatrix} \boldsymbol{\sigma} \\ \boldsymbol{E} \end{bmatrix} \tag{1.3}$$

Conventionally, index 3 is identified with the poling direction. For thin film piezoelectric materials, the poling direction corresponds to the thickness direction. As a consequence, indices 1 and 2 correspond to the in-plane directions, as shown in Fig. 1.1.

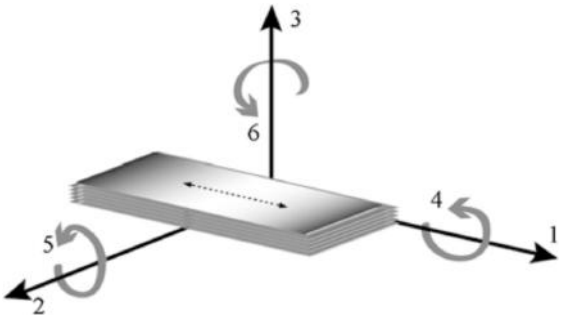

FIGURE 1.1: Conventional tensor directions of the constitutive equations for thin film piezoelectrics. Source: [28]

Sensing applications are based on the direct piezoelectric effect, meaning that only equation 1.1 is generally considered, with the appropriate boundary conditions. A scalar form (1-D) is obtained by imposing a set of mechanical and electrical simplifying assumptions, which eliminate the couplings between orthogonal directions. When

piezoelectric thin films are considered, electrodes are located only on the top and bottom faces of the film, hence $\boldsymbol{E} = E_3$ and $\boldsymbol{e} = e_{33}$. Moreover, a uniaxial stress condition without lateral deformation is generally assumed, hence $\boldsymbol{\sigma} = \sigma_i$ and $\boldsymbol{s_E} = s_{ii}$.

When the piezoelectric element is uniaxially stressed, the short-circuit charge is given by imposing $E = 0$ in the scalar form of Eq. 1.1:

$$Q = d_{3i}\sigma_i A \tag{1.4}$$

where σ_i is the uniaxial stress in direction i and A the cross-section area with electrodes.

The open-circuit voltage is given by imposing $D = 0$, hence:

$$V_{OC} = \frac{d_{3i}\sigma_i t}{e_{33}} \tag{1.5}$$

where t is the thickness of the piezoelectric element in direction 3. A piezoelectric voltage coefficient g can be conveniently defined as:

$$g_{3i} = \frac{d_{3i}}{e_{33}} \tag{1.6}$$

so that the open-circuit voltage expression simplifies further:

$$V_{OC} = g_{3i}\sigma_i t \tag{1.7}$$

The voltage coefficients g directly provide the voltage generated by a piezoelectric element under a given mechanical stress [31]. For this reason, they enable a direct performance comparison of piezoelectric materials for voltage-based sensing applications.

1.1.2 Piezoelectric materials

The most commonly adopted piezoelectric materials for transducer applications are of ceramic and polymeric type. Ceramic piezoelectric materials include lead zirconium titanate (PZT), barium titanate (BTO), aluminum nitride (AlN) and zinc oxide (ZnO). Polymeric materials include Polyvinylidene fluoride (PVDF), Parylene-C and poly-L-lactide (PLLA).

PZT [32], [33], ZnO [9], [12], [34]–[36] and AlN [37], [38] represent the most commonly adopted piezoelectric materials for MEMS microphone fabrication. PZT is a polycrystalline ceramic ferroelectric material, characterized by large piezoelectric coefficients. For this reason, it has been historically a popular choice for sensing, actuation and energy harvesting applications [39]. However, PZT is a lead-based compound and goes against restrictions in several countries concerning the adoption of toxic materials [40]. AlN and ZnO are alternative piezoelectric solutions gaining increasing interest for application in MEMS microphones, also in consideration of their voltage coefficients, higher than PZT (see Table 1.1).

PVDF occupies a prominent position among polymeric piezoelectric materials, being characterized by several advantages such as high piezoelectric coefficients, low acoustic impedance, wide frequency response, resistance to chemicals and excellent mechanical properties [41]. PVDF is strongly ferroelectric in its β crystalline phase

[42], commonly obtained by a combination of mechanical stretching and electrical poling [43]. As a result, PVDF is generally produced in the shape of thin-films. PVDF is adopted in non-litographic implementations, including microphones with curved piezoelectric films [6]–[8] and microphones having pillar structure [44], [45]. Table 1.1 shows a comparison of common piezoelectric materials properties.

1.2 3D-Printing

1.2.1 3D-Printing techniques

The predominant 3D-printing techniques for device fabrication can be classified into the following main categories: fused deposition modeling (FDM), photocuring (SLA, DLP), laser sintering and laser melting (SLS, SLM) and photopolymer jetting (Ployjet).

FDM involves the extrusion of a melted thermoplastic filament through a nozzle. The 3D object is realized by depositing the material on the fabrication platform in a layer-by-layer fashion. The deposition of each layer requires a cooling time to let the previous layer solidify. FDM 3D printers employ filaments of thermoplastic material, including acrylonitrile butadiene styrene (ABS), polyamide (PA) and polylactic acid (PLA). FDM is widely adopted, due to its versatility and limited cost. However, the FDM printers resolution is generally low when compared to other technologies.

Photocuring adopts ultraviolet (UV) light to cure and solidify polymers in liquid state. The process is repeated in a layer-by-layer fashion until the final object is obtained. The strategy embraces two very similar technologies: stereo lithography (SLA) and digital light processing (DLP). In SLA, a container is filled with photosensitive liquid resin, which is solidified when exposed to a given ultraviolet light wavelength. A moving laser scans directly the liquid surface according to the desired pattern, leaving as a result a cured layer. The moving platform is then shifted of an amount equivalent to one layer thickness, allowing for a new scan. In the process, each cured layer sticks to the preceding layer, until the 3D model is obtained.

In DLP, each point of the current layer is cured simultaneously. This is performed through the adoption of a light source and a digital micromirror device, which selectively reflects the source light toward the desired destination points, creating the target curing image on the photosensitive resin. SLA and DLP are generally characterized by very high resolutions and are able to produce 3D-printed objects with fine details. On the downside, a model can only be realized with a single material.

		PZT PIC 151	**ZnO**	**AlN**	**PVDF**	**ParyleneC**
Density	[Kg/m^3]	7800	5610	3230	1800	1290
Young Modulus	[GPa]	60	201	308	2.5 to 3.2	2.8
Dielectric Constant $\epsilon_{r_{33}}$	-	2400	11	10.5	12	3.15
d_{31}	[pC/N]	-210	-5	-1.73	6 to 20	-
d_{33}	[pC/N]	500	12.4	5.5	-13 to -28	2.0
g_{33} [a]	[Vm/N]	0.023	0.127	0.059	-0.12 to -0.26	0.072

[a] Coefficients g_{33} are derived from Eq. 1.6

TABLE 1.1: Comparison of common piezoelectric materials properties. Source: [46], unless otherwise noted.

SLS or SLM selectively melt material in powder form. At each iteration, a coat of powder is deposited on the building platform. A laser scans the surface according to the desired pattern, selectively melting the powder to form a layer of the object. The platform is then lowered, and a new coat of powder is deposited on top of the previous layer for sintering. The process is repeated on a layer-by-layer fashion until the 3D model is obtained. The most common powdery material are thermoplastics. However, other types of materials are also available, including plastics, ceramics and metals. The main advantage of SLA and SLM is the ability to create high density and high strength products, able to meet military standards.

Ployjet adopts ultraviolet (UV) light to cure and solidify photosensitive resins. An inkjet nozzle sprays the resin in liquid form on a mobile platform, which is then cured by UV light. The final product is obtained through layer-by-layer fabrication. Ployjet is characterized by very high resolutions, but generally produces delicate objects with weak parts.

1.2.2 3D-Printing performance

The quality of a 3D-printed object is affected by the capabilities of the 3D-printing process and the printer itself. The main parameters to consider are the resolution and the accuracy.

The resolution provides a measure of the level of detail at which a design can be actually printed and is mainly dictated by the minimum possible movements of the printing head. Higher resolutions result in smoother objects, with finer details and higher perceived quality. It is worth noticing that higher resolutions do not imply smaller errors. A printed object may be characterized by incredibly fine details. Still, the actual measurements may be out of tolerance with respect to those defined at design time.

Since the manufacturing process occurs in three dimensions, both a planar (XY) and a vertical (Z) resolution can be defined. The XY resolution, also called minimum feature size, is strictly correlated to the minimum dimension of a printed detail. The Z resolution, also called layer thickness, corresponds to the minimum vertical movement of the printing head (or build platform) and is thus equivalent to the thickness of one layer of deposited material, according to the manufacturing process. The vertical resolution is easily determined and thus generally reported, while the planar resolution is measured through complex microscopic imaging techniques and thus not always indicated.

The accuracy determines the closeness of a measurement to the true value. The accuracy depends on both systematic (repeatable) errors and random errors. In 3D printing, the true values are specified in the CAD design of the model. Therefore, the accuracy of a 3D printed object is higher if it resembles closely the quotes specified in the digital counterpart.

The 3D-printing process is also characterized by several geometrical restrictions which limit the range of printable geometries. Features that are spatially too close in the 3D CAD design, for instance, are likely to be fused together when printed as a physical object. The technological limits of the printer are thus translated into the definition of a set of restrictions related to specific geometrical details or conditions. These limitations determine, in the first place, the feasibility of a target design. Their evaluation is therefore a priority with respect to the inspection of selectable printing parameters (e.g. infill). In addition, geometrical limitations should be considered at design time, for a

target technique and printer, to avoid the design of critical features which may deteriorate the overall quality of the result. Important geometrical restrictions to consider are the wall thickness and the clearance.

The wall thickness refers to the distance between one surface of the model and the opposite sheer surface. Elements printed below the wall thickness specification will likely to fail. In addition, most printing techniques require a curing phase or post-processing after printing, which may be critical for very thin details. SLA, for instance, generates peel forces during the fabrication process, which may warp low-thickness walls.

Clearance refers to the distance between two non-contacting model features that are close together in the design. These features may fuse together in the printed object if the clearance specification is not respected. Table 1.2 presents a comparison of printing performance of the main 3D-printing techniques.

1.3 Architectural solutions of piezoelectric microphones

1.3.1 Fundamental microphone specifications

In the following, a brief description of the fundamental microphone specifications is provided. Such overview is intended to clarify the piezoelectric microphones results from the subsequent literature review. In addition, it provides a basis for the technical considerations expressed throughout this thesis work.

The fundamental microphone specification is represented by its *frequency response*. The microphone frequency response denotes the relative variations of the electrical output according to the frequency of the acoustic input. The typical frequency response is shown in Fig. 1.2. The frequency region that is approximately constant is known as the flat band. Within this region, the microphone behaves as an almost ideal sensor. The magnitude of the output electrical signal is proportional to the magnitude of the input pressure signal, for each frequency, hence avoiding alterations of the frequency content of the input sound.

The magnitude of the frequency response within the flat band is known as *sensitivity*. The sensitivity is measured in V/Pa (or dB re. 1 V/Pa), and corresponds to the constant ratio between the output voltage and the input pressure, for frequencies lying within the flat band. Of course, the microphone sensitivity at frequencies lying outside

		FDM Fortus 250mc	**SLA Form 2**	**SLS Fuse 1**	**Polyjet Objet260**
Resolution (Z)	[µm]	178-330	25-200	100	16-32
Accuracy	[µm]	241	50	-	80-200
Wall Thickness (Supported)	[µm]	635-1194	400	750	600
Clearance	[µm]	310-660	500	250	300
Material	-	Thermoplastics	Photoresin	Thermoplastics	Multiple

TABLE 1.2: Comparison of performance of common 3D-Printing techniques (data gathered from printer datasheets)

the flat band is variable, and cannot be expressed as a single scalar value. Generally, manufacturers denote the sensitivity at a specific frequency within the flat band. For instance, the company Brüel & Kjær usually expresses the sensitivity of its microphones at 250 Hz.

The frequency response curve is generally normalized with respect to the flat-band sensitivity (as in Fig. 1.2). Hence, a complete description requires both the frequency response curve and the sensitivity specification. The frequency response without normalization includes both types of information and is usually called sensitivity frequency response.

The microphone *bandwidth* is defined as the range of frequencies for which the frequency response is equal to the sensitivity value to within a certain tolerance. Hence, in principle, the tolerance should be expressed together with the bandwidth. A typical tolerance is $\pm 3dB$ with respect to the sensitivity value [47]. The lower limit of the bandwidth is generally affected by the conditioning circuitry and the microphone venting (for the vent, see chapters 2 and 3). The upper limit of the bandwidth, instead, is determined by the fundamental resonance of the vibrating elements, which usually correspond to the moving diaphragm.

The complete bandwidth specification, including tolerance, is generally reported only in high-end commercial grade microphones. When research studies are considered, the bandwidth specification is less strict and tolerances are basically never reported. In the following, the microphone bandwidths reported by the authors of research works are considered. For the microphone measurements performed in chapter 4, instead, a tolerance is properly defined.

The frequency response may be also equalized through properly designed electronics, integrated with the sensing element. The equalization may, for instance, correct for unwanted peaks and dips in the microphone frequency response. In addition, standard equalization procedures exists, like A-weighting, which account for psychoacoustic effects. Such types of equalization correct the microphone response from the perspective of human perception, characterized by uneven sensitivity at different sound frequencies.

In the following, the frequency response characterizing the sensing element alone is considered, without any further equalization procedure. The focus of this thesis work is an early-stage evaluation of the feasibility of 3D-printing for microphone fabrication. Hence, the emphasis is put on the capabilities of the transducer, focusing its physical behavior. Most of the research works about microphones, including the literature review which follows, adopt the same principle. As a result, the performance can be consistently compared.

1.3.2 Microphones with bending diaphragm

Piezoelectric microphones adopting a diaphragm structure in bending motion represent by far the most common type. The standard design consists of a thin vibrating membrane, generally clamped, and constituted by a piezoelectric film sandwiched between electrodes and backed by an additional supporting layer. The membrane bends when the acoustic stimulus is applied, generating a mechanical stress on the piezoelectric element and thus an electrical response. In the following, an overview of piezoelectric microphones with a diaphragm structure is provided.

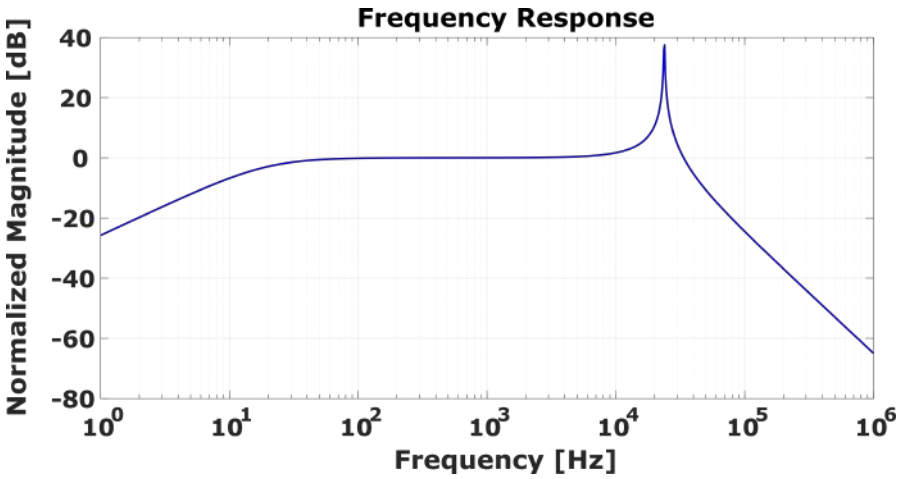

FIGURE 1.2: Typical microphone frequency response

Many similar solutions involving clamped diaphragms are present in literature, usually in combination with MEMS fabrication technology. Devices with both circular [10], [11], [33], [36], [38] and square diaphragms [12], [32], [34], [35] have been designed.

The MEMS microphone of Fig. 1.3 with a circular diaphragm is described in [9]. The simple design consists of a sputtered zinc oxide (ZnO) piezoelectric layer on top of a thin, circular and clamped silicon diaphragm. The diaphragm is etched from the back side of the silicon wafer upon completion of the deposition process. The diaphragm has a diameter of 3 mm and a thickness of 30 µm, while the ZnO layer has a thickness of 3 µm. The study reports a sensitivity of 250 µV/Pa for the given device in the bandwidth 10 Hz-10 kHz.

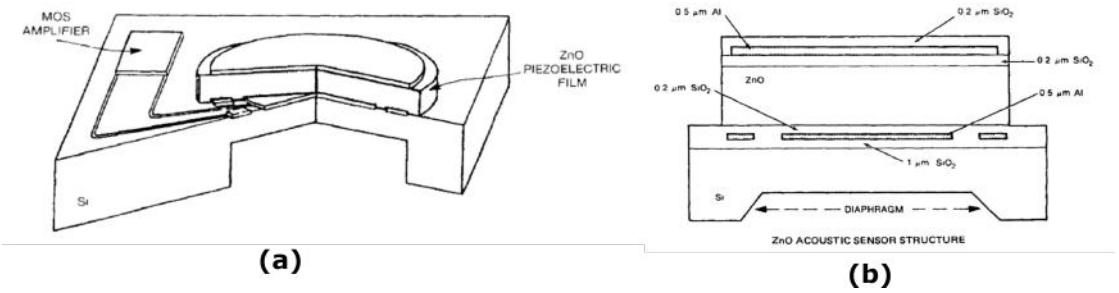

FIGURE 1.3: MEMS Piezoelectric microphone with zinc oxide (ZnO) piezoelectric film on circular diaphragm and integrated signal conditioning. (a) 3D representation. (b) Cross-sectional view. Source: [9]

The piezoelectric layer and electrodes positioning varies according to the expected stress distribution during operation. In circular diaphragms, the maximum stress occurs at the center and at the periphery. In [10], [11], the piezoelectric and electrode layers are disposed according to an annular geometry to capture the peripheral stress. In square diaphragms the maximum stress occurs instead at the corners, as analyzed in [36].

A cantilever diaphragm configuration has been also investigated [13], [48]–[50]. In this solution, the diaphragm is clamped to a rigid support only on one side, while the remaining part is free to deflect.

Fig. 1.4 depicts a piezoelectric microphone with a square cantilever diaphragm, presented in [48]. The diaphragm has a square section area of 2 x2 mm^2 and a thickness of 4.5 ¯m. The piezoelectric ZnO layer is RF magnetron sputtered on top of a low pressure chemical vapor deposited (LPCVD) low-stress silicon nitride support layer. The study reports a very high sensitivity of 30 mV/Pa for the given device, enabled by the significant compliance of the diaphragm. However, the ample displacements reduce the bandwidth to a range comprised between 100 Hz and 890 Hz. In [49], an improvement of the same base design led to a bandwidth of 1.8 KHz while maintaining the sensitivity unaltered.

The most recent and successful development involving cantilever diaphragms is maybe represented by the commercial Vesper suite [13]. The typical diaphragm of Vesper microphones is realized with four triangular cantilevers clamped to a squared-shape frame and deflecting at the center. Of course, the fabrication details are not available to the public.

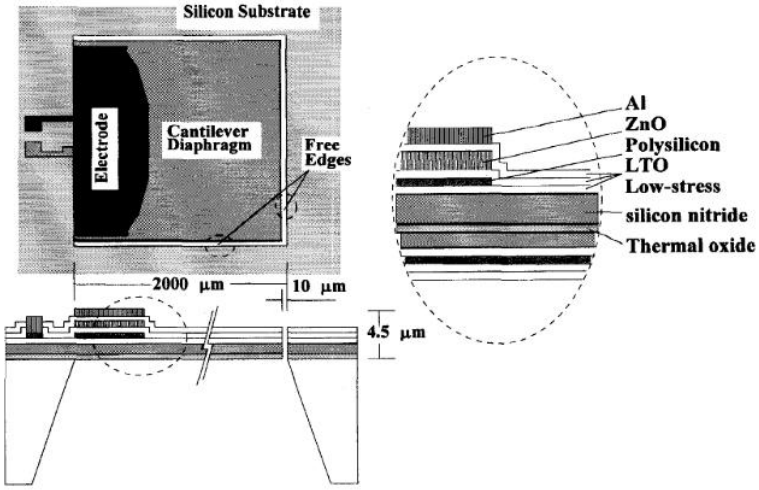

FIGURE 1.4: MEMS Piezoelectric microphone with square diaphragm in cantilever configuration and zinc oxide (ZnO) piezoelectric film. Source: [48].

1.3.3 Microphones with pillar structure

The piezoelectric microphone with pillar structure adopts a combined strategy to increase the voltage sensitivity of the device. The sensitivity is enhanced through the combination of a pillar-based mechanical structure and the electrode patterning of the piezoelectric element. The two design features allow improving the voltage sensitivity of the device by the ratio of the area exposed to the acoustic field and the stressed area of the piezoelectric component. The mechanism is described in more detail in section 1.4. In the following, an overview of the existing piezoelectric microphones with pillar structure is provided.

The microphone of Fig. 1.5 is described in [45]. The microphone uses a commercial piezoelectric film of Polyvinylidene Fluoride (PVDF) as the starting active element, with uniform electrodes already printed on both surfaces.

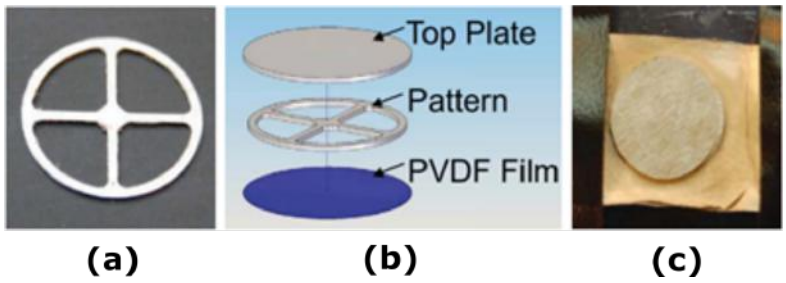

FIGURE 1.5: Realization of pillar-based piezoelectric microphone in [45]. (a) Aluminum sample with crosshair pattern, implementing the pillar function. (b) Exploded view of the components. (c) Assembled device.

The microphone manufacturing is relatively simple. An aluminum specimen having crosshair pattern is glued with M-bond 200 adhesive on the upper side of the piezoelectric film. The specimen implements the function of rigid pillar. The excess parts of the upper electrode are removed through acetone, realizing the electrode patterning. A rigid plate is then glued on the top of the aluminum sample. Finally, contacts are made with copper strips, and the assembly is glued to a stiff substrate.

Unfortunately, the microphone is characterized by a reduced sensitivity of 27.8 µV/Pa, mainly due to the low ratio between the area of the top plate and the section area of the aluminum sample, corresponding to the piezoelectric film solicited area. The manufacturing technique presents a limit: the gluing of the aluminum specimen with cyanoacrylate adhesive does not allow sufficient construction precision, necessary to ensure a high area ratio and thus a competitive sensitivity.

The microphone of Fig. 1.6 is described in [44]. In this configuration the pillars themselves are made of piezoelectric material, performing the twofold function of signal generation and force concentrators.

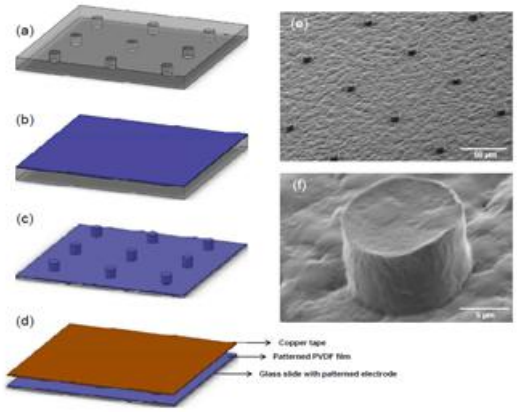

FIGURE 1.6: Realization of pillar-based piezoelectric microphone in [44]. (a) PDMS mold. (b) Spin-Coating of the PVDF solution on the mold. (c) Optical alignment of the PVDF patterned film with the upper electrode. (d) Application of the copper tape. (e) and (f) SEM images of the piezoelectric pillars.

The realization is rather complex due to the ad-hoc manufacturing of the patterned

piezoelectric film. The fabrication steps are the following 1) the pillars pattern is reproduced with a photolithographic technique on a silicon matrix 2) the matrix is used to create a mold in PDMS 3) the PVDF in liquid solution is deposited on the mold with a spin-coating technique, obtaining the patterned piezoelectric film 4) the pattern is reproduced with a photolithographic technique on a glass substrate to realize the upper electrode 5) an optical alignment is carried out to match the PVDF pillars and the electrode pattern 6) a copper tape is applied on the PVDF pillars to make the lower electrode 7) the PVDF is polarized 8) the assembly is glued on a rigid substrate.

The overall process is complex and delicate, with some particularly critical phases, including the optical alignment and the polarization of the piezoelectric material.

1.3.4 Microphone architectures and 3D-Printing

Piezoelectric microphones with a diaphragm structure rely on the generation of mechanical stress within the piezoelectric material during bending [12], [51]. The effectiveness of this structure is thus tightly coupled to the mechanical characteristics of the diaphragm.

Generally, the diaphragm deflection is lower than the thickness of the membrane itself, so that thin-plate theory can be adopted for stress analysis [51]. According to thin plate theory, a transverse load generates a stress profile as in Fig. 1.7, with a peak stress at the top (or bottom) surface of the form:

$$\sigma_{pk} = Pk\frac{a^2}{t^2} \tag{1.8}$$

where P is the uniform load, k is a constant which depends on the considered radial position (center or border) and stress component (radial or tangential), a and t are the diaphragm radius and thickness, respectively. Notice that the mechanical stress undergoes a phase inversion in the through-thickness direction, regardless of the radial position. Hence, a purely piezoelectric diaphragm would be subject to a nearly zero net stress. A laminated solution is instead required, where the piezoelectric layer is backed by an additional support layer. In this way, the neutral axis is shifted outside the piezoelectric element, generating a net tension or compression in the cross-section of the piezoelectric film [12].

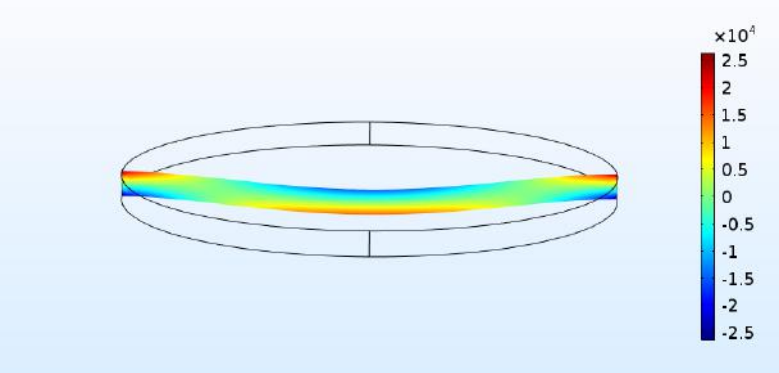

FIGURE 1.7: Stress profile (radial component) in the middle cross-section of a clamped circular plate under uniform load.

Author	Architectural Solution	Sensitivity	Bandwidth
[9]	Clamped Diaphragm MEMS (ZnO)	250 µV/Pa	10 Hz - 10 kHz
[34]	Clamped Diaphragm MEMS (ZnO)	920 µV/Pa	100 Hz - 18 kHz
[49]	Clamped Diaphragm MEMS (ZnO)	30 mV/Pa	50 Hz - 1.8 kHz
[32]	Clamped Diaphragm MEMS (PZT)	38 mV/Pa	10 Hz - 20 kHz
[33]	Clamped Diaphragm MEMS (PZT)	97.9 nV/Pa - 920 nV/Pa	-
[10]	Clamped Diaphragm MEMS (PZT)	1.66 µV/Pa	100 Hz - 6.7 kHz
[37]	Clamped Diaphragm MEMS (AlN)	-	1 kHz - 6 kHz
[36]	Clamped Diaphragm MEMS (ZnO)	39.6 µV/Pa (Avg.)	-
[11]	Clamped Diaphragm MEMS (AlN)	39 µV/Pa	69 Hz - 20 kHz
[35]	Clamped Diaphragm MEMS (ZnO)	382 µV/Pa	30 Hz - 8 kHz
[38]	Clamped Diaphragm MEMS (AlN)	0.68 mV/Pa	20 Hz - ~8 kHz
[12]	Clamped Diaphragm (Composite) MEMS (ZnO)	1 mV/Pa	200 Hz - 10 kHz
[48]	Cantilever Diaphragm MEMS (ZnO)	30 mV/Pa	100 Hz - 0.89 kHz
[49]	Cantilever Diaphragm MEMS (ZnO)	30 mV/Pa	50 Hz - 1.8 kHz
[50]	Cantilever Diaphragm MEMS (AlN)	111 µV/Pa	1 Hz - ~10 kHz
[13]	Cantilever Diaphragm MEMS (ZnO)	12.6 mV/Pa	100 Hz - 10 kHz
[44]	Pillars (PVDF)	189.3 µV/Pa	-
[45]	Pillars (PVDF)	27.8 µV/Pa	10 Hz -20 kHz

TABLE 1.3: Summary of common piezoelectric microphone solutions.

It is evident that large, thin diaphragms are required to increase the sensitivity. Unfortunately, large diaphragms would decrease substantially the mechanical resonance frequency, and thus the microphone bandwidth. As a result, the solution finds practical application at MEMS scale, where small radii and very thin diaphragms are adopted, with a thickness in the order of tens of micrometers.

The fabrication of very thin diaphragms with 3D-printing is limited by both the printer resolution and the geometrical restrictions. The wall thickness specification, in particular, limits the thickness of fabricated diaphragms to several hundreds of micrometers, an order of magnitude greater than the MEMS counterpart. Unfortunately, the sensitivity compensation by means of bigger radii is inevitably accompanied by a drop in the mechanical resonance frequency. The 3D-printing fabrication method does not allow, in fact, the resonance tuning through the application of a controlled diaphragm tension [52].

A further limitation is represented by the coupling of the piezoelectric layer with the 3D-printed support layer, required to shift the neutral axis during vibration. An effective stress transfer requires a tight coupling between the two elements. A manual adhesion after printing is not practical, also considering the fragility of the component. Hence, the piezoelectric element should be printed and potentially poled in-situ. Although feasible, it introduces significant complexity in the overall fabrication process.

The described limitations are not present in the pillar-based approach, which exploits the piezoelectric element in compression, as shown in Fig. 1.8b. According to this strategy, a rigid top plate acts as a rigid diaphragm and transfers the incident force, coming from the acoustic pressure field, to the pillars in contact with the piezoelectric material. The pillars concentrate the aforementioned force on a confined area of the piezoelectric film, generating on the active surface an electric charge proportional to the applied mechanical stress. One of the electrodes is patterned according to the pillars geometry, reducing the equivalent electrical capacitance formed by the two electrodes and the interposed film. The combination of the mechanical pillar structure and the electrode patterning improves the voltage sensitivity of the device by the ratio of two areas, namely the area exposed to the acoustic field and the stressed area of the piezoelectric element. See section 1.4 for a more detailed description of the mechanism.

The pillar-based solution allows for a simplified overall mechanical structure, with a reduced number of critical features. The dimensional constraints concerning the diaphragm thickness of the bending-based solution can be relaxed, resulting in a thicker plate suitable for the pillar-based strategy. In addition, the area ratio principle can be implemented with a variety of geometries, according to the the capabilities of 3D-printing.

The analyzed piezoelectric microphones in 1.3.3 are characterized by a limited area ratio (i.e. sensitivity) or present a complex fabrication process. In this sense, 3D-printing may provide an edge over existing solutions, by reducing the complexity while maintaining, or even increasing, the sensitivity.

In the following, the pillar-based approach is analyzed in more detail, and a 3D-printing compatible design is described.

1.4 3D-Printed pillar-based microphone design

1.4.1 Pillar-based design concept

The simplest configuration of a piezoelectric pressure sensor is shown in Fig. 1.8a, where the piezoelectric material is simply put between two conductive electrodes, forming a capacitive element. A pressure stimulus perpendicular and uniform on the sensor surface induces stress and strain in the piezoelectric material, generating opposite charges on the two electrodes. In such configuration, the voltage sensitivity of the sensor can only be improved by changing the piezoelectric material or increasing the piezoelectric material thickness [53] [54]. Assuming for simplicity a uniaxial stress state of the piezoelectric film, the open-circuit voltage is:

$$V_{fl} = \frac{d_{33}\sigma_3 t}{e} = P\frac{d_{33}t}{e} \tag{1.9}$$

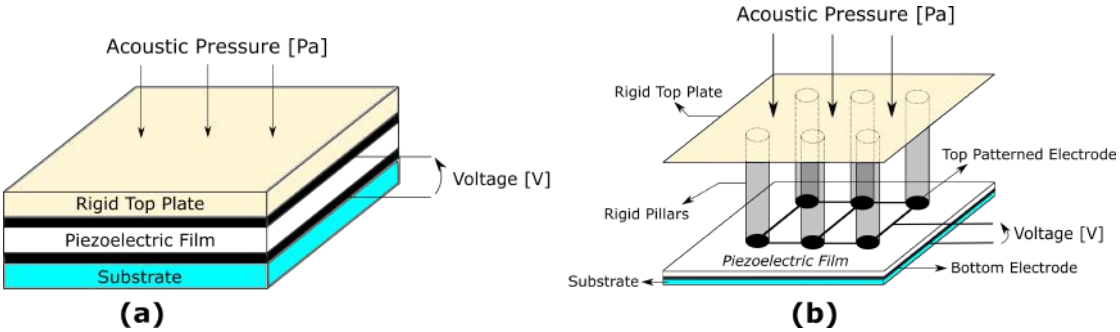

FIGURE 1.8: Piezoelectric sensor with (a) flat configuration and (b) pillar structure with patterned electrodes.

The pillar-based structure shown in Fig. 1.8b enables a new degree of freedom for improving the sensor voltage sensitivity. As anticipated in section 1.3.4, the pillars concentrate the force exerted on the top plate to a limited area of the piezoelectric film. The film generates on the active area an electric charge proportional to the applied mechanical stress. One of the electrodes is patterned according to the pillars geometry, reducing the equivalent electrical capacitance of the sensor. The combination of the pillar structure and the patterned electrode allows improving the voltage sensitivity of the device according to the ratio between the area exposed to the acoustic pressure and the stressed area of the piezoelectric film.

A uniform acoustic pressure P exerted on the top plate surface results in an equivalent force $F = P \cdot A_{tp}$, in which A_{tp} is the plate cross-sectional area. If the pillars are symmetrically distributed with respect to the top plate, the piezoelectric active area is subject to a uniform mechanical stress equal to:

$$\sigma_3 = \frac{F}{A_{ps}} = \frac{PA_{tp}}{A_{ps}} = PA_r \tag{1.10}$$

where A_{ps} is the total pillars cross-sectional area and A_r is the area ratio.

The patterned electrode allows matching the cross-sections of the electrical and mechanical active areas. In other terms, the electric charge generated by the piezoelectric effect is confined within the mechanically stressed area. As a result, the combination of

the piezoelectric active areas can be treated as a single piezoelectric element, with total cross-section area A_{ps} and known mechanical stress. The open-circuit voltage can then be computed according to the piezoelectric constitutive equation by imposing $D = 0$, resulting in:

$$V_{pl} = \frac{d_{33}\sigma_3 t}{e} = P\frac{d_{33}A_r t}{e} = A_r V_{fl} \tag{1.11}$$

The electrode patterning is critical for the sensitivity improvement mechanism. A pillar structure with full electrodes would reduce the open-circuit output voltage, due to the spreading of the generated image charge over the entire electrode area. The generated image charge is equal to:

$$Q = d_{33}\sigma_3 A_{ps} = Pd_{33}A_{tp} = Fd_{33} \tag{1.12}$$

The equivalent capacitance formed by the electrodes with the interposed film is:

$$C = \frac{eA}{t} \tag{1.13}$$

where A is the cross-sectional area of the full electrode. Hence, the open-circuit voltage would be:

$$V_{fe} = \frac{Q}{C} = \frac{Pd_{33}t}{e}\frac{A_{tp}}{A} \tag{1.14}$$

It is evident that the pillar structure is beneficial only when $A << A_{tp}$. The optimal condition is obtained when $A = A_{ps}$, leading to $V_{fe} = V_{pl}$. On the contrary, when $A = A_{tp}$, the sensitivity degenerates to the flat configuration, with $V_{fe} = V_{fl}$.

1.4.2 3D-Printed pillar-based microphone design

The proposed design of a pillar-based piezoelectric microphone compatible with 3D printing is presented in Fig. 1.9.

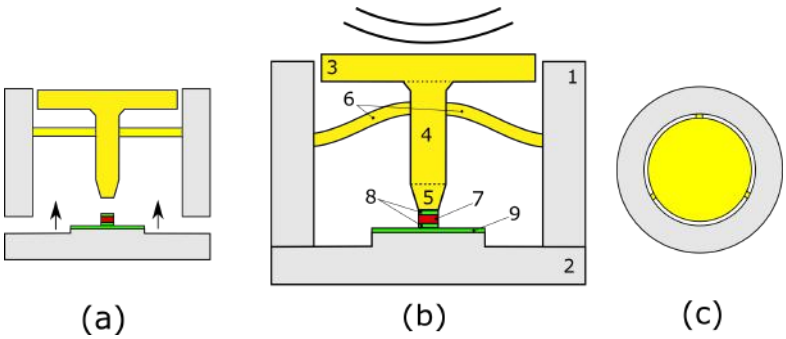

FIGURE 1.9: Design of 3D-printed single-pillar piezoelectric microphone. Cross-sectional view: (a) during preload and (b) assembled with preload. (c) Top View. Stationary part (grey): 1) chassis and 2) rigid enclosure with preload boss. Moving part (yellow): 3) top plate, 4) pillar body, 5) pillar tip and 6) flexural spring (preloaded). 7) Piezoelectric element (red). Electrical part (green): 9) rigid substrate with 8) electrodes. The preload excursions and the spring bending are exaggerated for clarity.

Description

The design comprises a stationary part, a moving part and an electrical part. The stationary part consists of a hollow chassis (see Fig. 1.9b part 1) and a rigid enclosure to the base (2). The chassis contains the moving part, deputed to the mechanical solicitation of the piezoelectric layer. The moving part comprises a top plate (3), exposed to the acoustic field on the external side. A single pillar (4) is rigidly connected to the internal side of the top plate. The other end of the pillar is placed in contact with the piezoelectric layer.

The force impressed on the plate by the acoustic load is transferred to the piezoelectric element by the pillar. To this purpose, the plate is not connected to the chassis to avoid detrimental force transmission losses. A custom flexural spring (6) provides stability to the moving part and the correct preload. The preload guarantees constant contact between the pillar and the piezo. The spring consists of three small beams, radially disposed and angularly equidistant, which connect the pillar to the chassis. The preload spring is designed to be sufficiently compliant to allow an effective force transmission to the piezoelectric element. In addition, the entity of preload is tuned so as to establish a static operating point below the non-linear region of the piezoelectric film, thereby avoiding alterations of the dynamic behaviour. The rigid enclosure at the bottom enables the preload mechanism.

The electrical part consists of a rigid substrate (9) containing two sensor terminals. The piezoelectric material (7) is placed between the mechanical moving part and the rigid substrate. Both the electrodes (8) cover only the active area, corresponding to the pillar tip section area. The sensor open-circuit output voltage is generated between the bottom and top electrodes.

Fabrication details

The mechanical part consisting of chassis, top plate, pillar and preload spring is 3D-printed as a single unit. The rigid enclosure can be conveniently realized through a Printed Circuit Board (PCB), implementing the electrical part of the sensor and simultaneously providing a rigid substrate for the 3D-printed moving part.

Piezoelectric layer

The piezoelectric layer should be compatible with the voltage sensitivity improvement strategy of the pillar-based design. According to table 1.1, PVDF represents an optimal choice, due to its high g_{33} voltage coefficient. In addition, PVDF is available in convenient thin-film configurations, suitable for the proposed design. Indeed, thin-films can be easily integrated with the rigid enclosure during assembly.

Chapter 2

Circuit Model of Acoustic Propagation in Annular Waveguides

A critical component of the proposed microphone design is represented by the aperture around the top plate, connecting the internal cavity to the external ambient. To some extent, such aperture can be regarded as a microphone acoustic vent [47]. The vent is generally a narrow air channel which ensures that the static pressure within the internal cavity follows the pressure of the environment. On a properly designed microphone, the dynamic sound pressure fluctuations are not equalized until very low frequencies. As a result, a net force is produced on the diaphragm. Similarly, the aperture around the piezoelectric microphone plate should not allow significant dynamic pressure equalization effects, which would be detrimental for the proper working of the device.

In this chapter, the microphone aperture is assimilated to a thin waveguide with annular cross-section and analyzed accordingly. A circuit model of the acoustic wave propagation within the waveguide is derived, suitable for the development of a complete microphone model in Chapter 3.

2.1 Thermoviscous propagation

Classical acoustic wave propagation models ignore the viscosity and thermal conductivity phenomena. These effects become relevant when acoustic waves propagate in small conduits, like thin layers or narrow tubes [55]. A thermoviscous propagation model is required whenever the frequency-dependent boundary layers, in which viscous and thermal effects occur, extend in a significant section of the waveguide. This analysis is required over an always increasing number of applications, due to the progressive miniaturization of devices, such as inkjet print heads [56], hearing aids [57], MEMS devices [58], [59], and microphones [60], [61].

Thermoviscous acoustics has been extensively studied, leading to the development of several analytical models. However, the analytical solution of the full set of constitutive equations is extremely complex and generally possible only for very simple geometries, like cylindrical tubes or spherical resonators [62], [63]. Analytical solutions of more complex geometries can be obtained using approximated methods. Among all, the Low Reduced Frequency (LRF) approximation of the wave equation allows greatly reducing the model complexity while retaining very good accuracy, by separating the propagation and the constrained directions of the waveguide [64]. The LRF model is

widely adopted for simple geometries, having circular, triangular or rectangular cross-section [65], [66].

In the following, the LRF model is applied to waveguides with annular cross-section in order to derive a novel circuit model of the thermoviscous acoustic wave propagation. The exact analytical solution of the LRF wave propagation model in annular waveguides is shown to be very complex and difficult to manage for practical purposes. The model is thus simplified, approximating the complex propagation in annular waveguides with the simpler propagation in rectangular layers. A T-Network circuit composed of nonlinear and frequency dependent impedances is defined from the exact solution of the LRF model. Finally, a novel lumped-element circuit is obtained from the approximation of the T-network impedances as networks of linear electrical components.

2.2 LRF Models for annular waveguides

2.2.1 Annular waveguide geometry and assumptions

The annular waveguide geometry modelled in this work is depicted in Fig. 2.1. The acoustic wave propagation takes place in the annulus delimited by the inner radius r_i and the outer radius r_o, extending along the waveguide length L. This region can be equally described by the annulus with w and the mean radius r_m (i.e. the radius halfway between the inner and the outer radii).

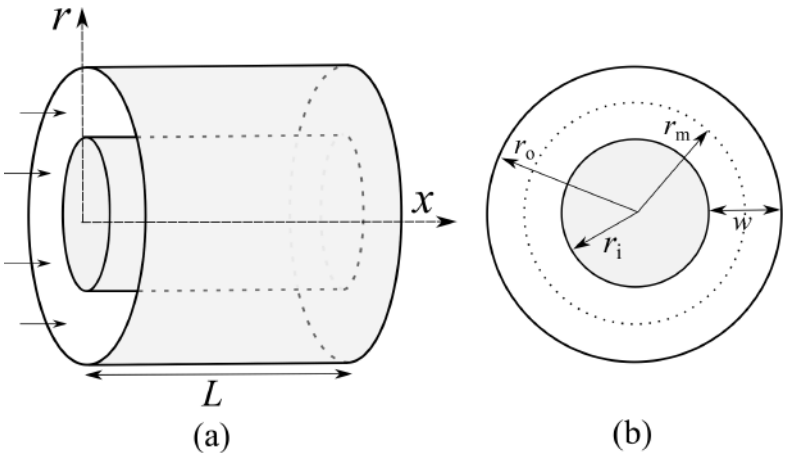

FIGURE 2.1: Annular waveguide geometry. (a) 3D representation of a waveguide segment of length L and (b) annulus corresponding to the horizontal cross section. The cross-section is characterized by the inner radius r_i and outer radius r_o or, equivalently, by the mean radius r_m and width w. The acoustic wave propagation takes place in the annulus delimited by the inner radius r_i and the outer radius r_o, along direction x and for the entire length L

A continuum flow regime, with no-slip and isothermal boundary conditions at the walls is considered. The assumption is satisfied when the waveguide width w is above a given threshold. When the width becomes too small, in fact, the velocity of the fluid

at the solid boundary deviates from the velocity of the boundary itself, violating the no-slip assumption. The Knudsen number K_n, which determines the flow regime according to the gas rarefaction, can be adopted for the definition of the validity range of w. The Knudsen number is defined as:

$$K_n = \frac{\lambda}{l} \tag{2.1}$$

where λ represents the molecular mean free path length and l the characteristic length, which characterizes the length scale of the waveguide cross-section [67]. In this work, l is defined as twice the hydraulic radius (i.e. $l = w$).

The continuum flow regime assumption is valid approximately when $K_\mathrm{n} < 0.01$ [68]. Considering air as a medium for wave propagation, the mean free path λ is approximately 60 nm [69]. According to Eq. 2.1 and under the hypothesis $l = w$, the validity of the ongoing analysis is thus restricted to $w > 6\,\mu\mathrm{m}$.

The system geometry and boundary conditions are considered to be axisymmetric (i.e. variations of the physical quantities occur only in the radial and axial directions).

2.2.2 LRF wave propagation model in annular waveguides

The Helmholtz wave equation governing the thermoviscous acoustic wave propagation, developed according to the LRF model, is given by [70]:

$$\frac{\partial \tilde{P}^2}{\partial x^2} - k^2 \Gamma^2 \tilde{P} = 0 \tag{2.2}$$

$$\Gamma = \sqrt{\frac{\gamma + (\gamma - 1) B(s_t)}{B(s)}} \tag{2.3}$$

Refer to table 2.1 for the definition of the symbols encountered within the analytical expressions.

The term Γ accounts for viscous and thermal effects in the wave propagation. The function B encapsulates the geometry related effects, and thus is a characteristic of the specific waveguide cross-section. For the one-dimensional propagation in the annular waveguide of Fig. 2.1, the function B becomes (see Appendix A):

Symbol	Description	Unit
P	Pressure	[Pa]
v	Particle velocity	[m/s]
ρ	Density	[kg/m^3]
k	Wave number	[1/m]
s	Shear wave number	[1/m]
s_t	Thermal wave number	[1/m]
γ	Adiabatic index	-

TABLE 2.1: Definition of symbols encountered within the analytical expressions.

$$B_A(z) = \frac{2}{r_o^2 - r_i^2} \frac{i}{\sqrt{iz}} [F_1(z) + F_2(z)] - 1 \tag{2.4}$$

$$F_1(z) = A_1(z)[r_o J_1(i\sqrt{iz}r_o) - r_i J_1(i\sqrt{iz}r_i)] \tag{2.5}$$

$$F_2(z) = A_2(z)[r_o Y_1(i\sqrt{iz}r_o) - r_i Y_1(i\sqrt{iz}r_i)] \tag{2.6}$$

$$A_1(z) = \frac{Y_0(i\sqrt{iz}r_i) - Y_0(i\sqrt{iz}r_o)}{Y_0(i\sqrt{iz}r_o)J_0(i\sqrt{iz}r_i) - Y_0(i\sqrt{iz}r_i)J_0(i\sqrt{iz}r_o)} \tag{2.7}$$

$$A_2(z) = \frac{J_0(i\sqrt{iz}r_o) - J_0(i\sqrt{iz}r_i)}{Y_0(i\sqrt{iz}r_o)J_0(i\sqrt{iz}r_i) - Y_0(i\sqrt{iz}r_i)J_0(i\sqrt{iz}r_o)} \tag{2.8}$$

where J_0, Y_0, J_1 and Y_1 are the Bessel functions of the first and second kind and of order 0 and 1, respectively.

2.2.3 Simplification of the Propagation Model for Lumped Model Development

When the mean radius of the annular cross-section r_m is much larger than its width w (i.e. $w/r_m \to 0$), then the annular geometry of Fig. 2.1 is well approximated by the semi-infinite, plain, rectangular layer depicted in Fig. 2.2, with thickness $t = w$ and same length L.

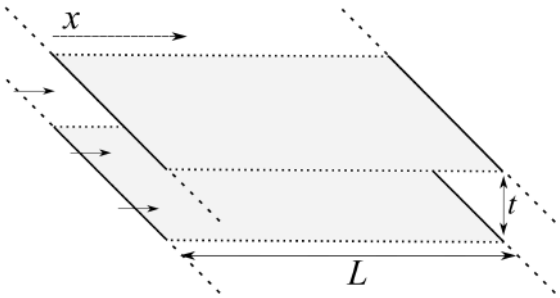

FIGURE 2.2: Waveguide with rectangular layers geometry. The waveguide is characterized by the length L and the thickness t, the latter corresponding to the distance between the walls. The acoustic wave propagation takes place in the volume delimited by the two walls, along direction x and for the entire length L.

In this geometry the wave propagation is one-dimensional, taking place in the volume delimited by the two walls, along the layer length. According to the LRF model [70], the function B becomes:

$$B_Y(z) = \frac{2\tanh(\frac{\sqrt{itz}}{2})}{\sqrt{itz}} - 1 \tag{2.9}$$

The validity of this geometrical approximation is analyzed comparing the functions for the annular cross-section B_A and the rectangular layer B_Y. Figure 2.3 shows the

comparison of the real and imaginary parts of the two functions against the adimensional shear wave number $\tilde{s} = ls$, with $w = t = l$. Considering $\tilde{s}$ allows evaluating B_{A} and B_{Y} regardless of the waveguides geometrical properties (i.e. the annulus w/r_{m} ratio and the layer thickness t, respectively).

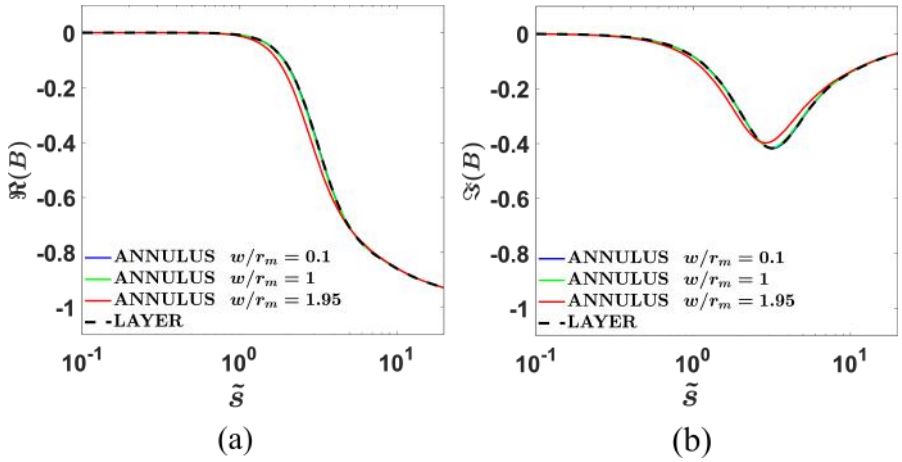

FIGURE 2.3: Comparison of the annulus and rectangular layers functions B_A and B_Y, respectively, as a function of the adimensional shear wave number $\tilde{s} = ls$, with $w = t = l$. Real part (a) and imaginary part (b).

Interestingly, the simpler B_{Y} well approximate B_{A} up to the physical limit of the geometrical ratio $w/r_{\mathrm{m}} = 2$, corresponding to the degeneration of the annular cross-section in a cylindrical cross-section. Thus, the acoustic propagation in a waveguide with annular cross-section can be conveniently approximated, for most practical purposes, with the propagation in a plain, rectangular layer.

2.3 Circuit model

2.3.1 T-Network Circuit Model

According to transmission line theory [71], an acoustic waveguide can be modeled as a two-port network, characterized by its length L, its propagation constant q, and its characteristic impedance Z_0. To each of the two ports is associated a pressure-velocity pair, as shown in Fig. 2.4a. The network is described as:

$$\begin{bmatrix} \tilde{P}_1 \\ \tilde{P}_2 \end{bmatrix} = \begin{bmatrix} \frac{Z_0}{\tanh(qL)} & \frac{Z_0}{\sinh(qL)} \\ \frac{Z_0}{\sinh(qL)} & \frac{Z_0}{\tanh(qL)} \end{bmatrix} \cdot \begin{bmatrix} \tilde{v}_1 \\ \tilde{v}_2 \end{bmatrix} \tag{2.10}$$

The thermoviscous acoustic wave propagation described by Eq. 2.2 presents the same form as the wave equation of a lossy electrical transmission line [71]. Hence, the propagation constant q and the characteristic impedance Z_0 within the matrix 2.10 are the following (see Appendix B for a full derivation of q and Z_0):

$$q = k\sqrt{\frac{\gamma + (\gamma - 1)B(s_t)}{B(s)}} \tag{2.11}$$

$$Z_0 = -\frac{i\omega\rho_0}{qB(s)} \tag{2.12}$$

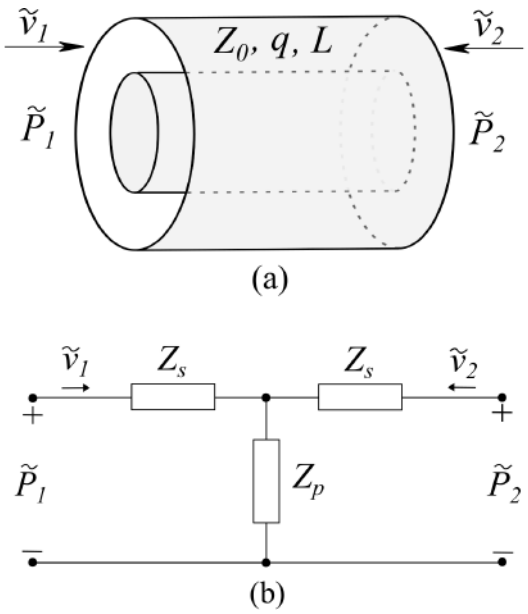

FIGURE 2.4: (a) Two-port network representation of an acoustic waveguide section of length L. A pressure-velocity pair is associated with each end (port). The waveguide is characterized by the length L the propagation constant q and the characteristic impedance Z_0. (b) Equivalent T-Network model of the waveguide, characterized by the impedances Z_s and Z_p.

where ω is the angular frequency, and ρ_0 is the density of the propagation medium (e.g. air). It is worth noting that both Eqs. 2.11 and 2.12 depends on the B function of the specific acoustic waveguide (i.e. on its cross-section geometry).

The transmission line modeling the thermoviscous acoustic wave propagation can also be conveniently represented with the equivalent T-network circuit shown in Fig. 2.4b, characterized by a series impedance Z_s and a parallel impedance Z_p:

$$Z_s = iZ_0[\cot(iqL) - \csc(iqL)] \tag{2.13}$$

$$Z_p = iZ_0 \csc(iqL) \tag{2.14}$$

The equivalent T-network circuit describes the acoustic wave propagation in annular waveguides, according to the exact LRF solution, by adopting the function B_A of Eq. 2.4 in Eqs. 2.13 and 2.14. Due to the nonlinear functions involved in their calculations, the obtained impedances Z_s and Z_p are frequency-dependent and nonlinear. Moreover, the complexity of the geometrical function B_A hampers the simplification of the impedances through analytical approximation techniques (e.g. Taylor's Series) and their representation as networks of linear electrical components. As a result, the model becomes complex and computationally intensive.

As shown in Section 2.2.3 and depicted in Fig. 2.3, the rectangular layer function B_Y provides an accurate approximation of the annular waveguide function B_A. Using the function B_Y of Eq. 2.9 in Eqs. 2.13 and 2.14, a simpler yet accurate approximation of the equivalent T-network circuit of the annular waveguide is derived. Even in this case, the obtained impedances Z_s and Z_p are frequency dependent and nonlinear. However,

their simpler expression allows for their approximation as networks of simple linear electrical components, with frequency-independent values (resistance, capacitance and inductance). The resulting lumped-element circuit model can then be implemented in software applications dedicated to electrical circuit simulation, allowing for convenient system level integrations.

2.3.2 The new lumped-element circuit model

The circuit model with linear electrical components is obtained from the T-Network model (Fig. 2.4b) for the waveguide having rectangular layers geometry, through approximation of the impedances Z_s and Z_p of Eqs. 2.13 and 2.14. The impedances are simplified through a rational or polynomial approximation of the involved nonlinear functions. A Laurent series expansion is applied to the cotangent and the cosecant functions in Eqs. 2.13 and 2.14. The hyperbolic tangent of the function B_Y is instead approximated, in the whole domain, by a set of Padé rational functions. With these assumptions, the impedances Z_s and Z_p finally become (see Appendix C):

$$Z_s = R_{s,1} + i\omega L_{s,1} + \frac{i\omega R_{s,2} L_{s,2}}{R_{s,2} + i\omega L_{s,2}} \tag{2.15}$$

$$Z_p = Z_{p,1} + Z_{p,2} \tag{2.16}$$

$$Z_{p,1} = \frac{1}{i\omega C_{p,1}} + \frac{R_{p,3}}{1 + i\omega C_{p,2} R_{p,3}} \tag{2.17}$$

$$Z_{p,2} = R_{p,1} + i\omega L_{p,1} + \frac{i\omega R_{p,2} L_{p,2}}{R_{p,2} + i\omega L_{p,2}} \tag{2.18}$$

where:

$$R_{s,1} = \frac{6\mu L}{t^2} \tag{2.19}$$

$$L_{s,1} = \frac{\rho_0 L}{2} \tag{2.20}$$

$$R_{s,2} = \frac{9\mu L}{t^2} \tag{2.21}$$

$$L_{s,2} = \frac{\rho_0 L}{10} \tag{2.22}$$

$$R_{p,3} = \frac{t^2 Pr P_0 \rho_0 (\gamma - 1)}{12 \gamma \mu L} \tag{2.23}$$

$$C_{p,1} = \frac{L}{P_0} \tag{2.24}$$

$$C_{p,2} = \frac{L}{P_0(\gamma - 1)} \tag{2.25}$$

$$R_{p,1} = -\frac{2\mu L}{t^2} \tag{2.26}$$

$$L_{p,1} = -\frac{\rho_0 L}{6} \tag{2.27}$$

$$R_{p,2} = -\frac{3\mu L}{t^2} \tag{2.28}$$

$$L_{p,2} = -\frac{\rho_0 L}{30} \tag{2.29}$$

The resulting network is shown in Fig. 2.5. Refer to table 2.2 for the definition of symbols encountered within the expressions. It is worth noting that the network is substantially different than the solutions found in literature [69], [72], [73].

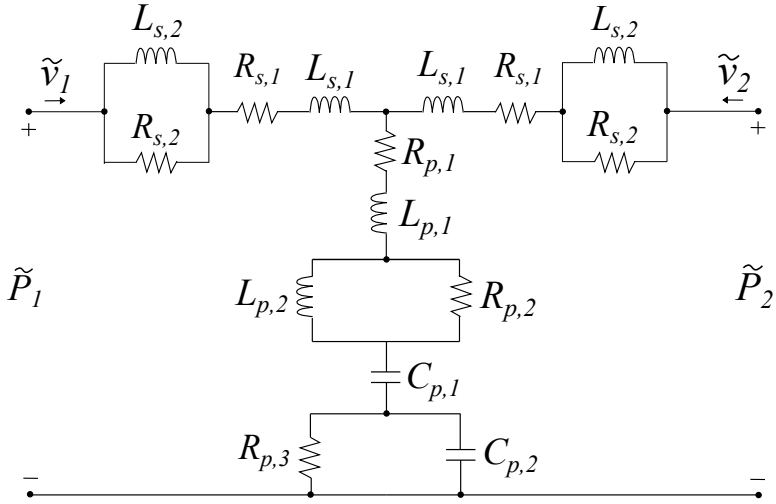

FIGURE 2.5: Simplified circuit model of a waveguide section of length L having rectangular layers geometry. The T-network impedances Z_s and Z_p are approximated as networks of linear electrical components.

The lumped element model is valid when:

$$\lambda \geqslant 2\pi L \tag{2.30}$$

where λ is the acoustic wavelength given by:

$$\lambda = \frac{2\pi}{Im(q)} \tag{2.31}$$

The condition derives from the Laurent power series expansion of the nonlinear functions in Eqs. 2.13 and 2.14, which provides accurate results only for small values of the argument and in agreement with the adopted expansion order.

A given waveguide of length L can also be approximated by a sequence of N network segments, each modeling a waveguide section of length $L' = L/N$. When multiple shorter segments are cascaded, a wider frequency range is likely to be correctly approximated, according to Eq. 2.30.

2.4 Simulation results

2.4.1 Description of the FEM Simulation Model

A FEM model of the waveguide with annular cross-section has been developed in COMSOL Multiphysics 5.3a. A two-dimensional (2D) axisymmetric model is selected to ensure low computational complexity, in agreement with the system geometry. The model consists of a rectangular air domain corresponding to the vertical cross-section to be revolved, in which thermoviscous acoustics equations are solved, as shown in Fig. 2.6.

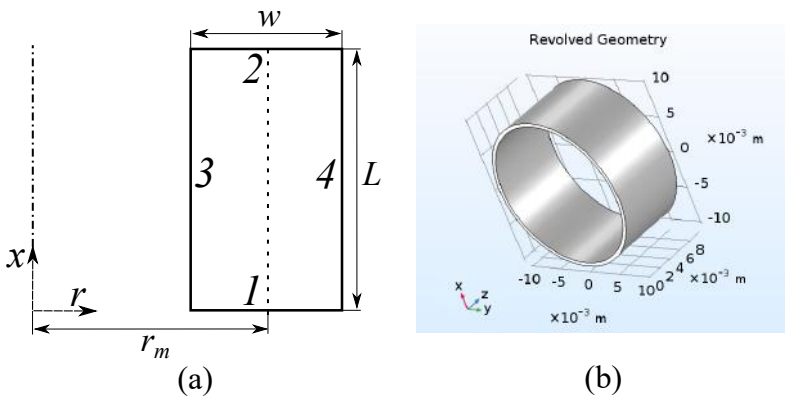

FIGURE 2.6: Axisymmetric rectangular domain implemented in COMSOL Multiphysics for the simulation of the annular waveguide. The edges of the domain constitute the input port 1, output port 2, and waveguide walls 3 and 4. (b) 3D annular waveguide representation obtained from the revolution of the rectangular domain about the axis of symmetry. The solution is computed only in the rectangular domain.

The bottom (1) and top (2) sides correspond to the input port and output port of the T-network, respectively. A pressure load of 1 Pa is applied to the input port, while a pressure release (0-pressure) or wall (0-velocity) boundary condition is applied to the output port, depending whether an open-ended or closed end configuration is modelled. A no-slip and isothermal boundary condition is applied to the waveguide walls (3) and (4).

2.4.2 Validation of the lumped-element circuit model

The input specific acoustic impedance of the lumped-element circuit model of Fig. 2.5 is validated against FEM simulations. The validation concerns both the open-ended (0-pressure) and closed-end (0-velocity) boundary conditions.

The specific acoustic impedance at the input port, with an open-ended boundary condition at the output port (short-circuit), is equal to:

$$Z_{OPEN} = \frac{Z_s \cdot Z_p}{Z_s + Z_p} + Z_s \tag{2.32}$$

When a closed-end boundary condition is applied at port 2 (open-circuit) the impedance becomes:

$$Z_{CLOSED} = Z_s + Z_p \tag{2.33}$$

COMSOL Multiphysics computes the solution for pressure and velocity at every meshing node. The input impedance is derived as the ratio between the average pressure and the average axial velocity at the entrance of the waveguide, corresponding to side 1 in Fig. 2.6. The estimation of Z_{OPEN} requires a pressure release boundary condition applied at the other end of the waveguide (side 2). The estimation of Z_{CLOSED} requires instead a wall boundary condition.

Figure 2.7 shows the input specific acoustic impedance as a function of frequency, for both the open-end and closed-end boundary conditions. The physical parameters adopted in all computations are listed in Table 2.2. The considered waveguide has mean radius r_{m} and length L equal to 10 mm.

Different values of the width w are considered, corresponding to different configurations of inner radius r_{i} and outer radius r_{o}. The value of w equal to 10 µm roughly corresponds to the lower limit fulfilling the modeling assumption of continuum flow regime. The frequency range satisfies the LRF validity conditions for all geometries (see A). The curves from the lumped-element circuit of Fig. 2.5 are kept consistent by imposing $t = w$. Hence, such common geometrical dimension will be denoted henceforth as the characteristic length l. The length L of the annular waveguide is approximated with both a single network segment of length L and a circuit composed of 50 cascaded segments of length $L' = L/50$ each.

For the sake of clarity, a modified logarithmic transformation is applied to the reactance data (y-axis) [74]. The transformation better separates the curves within the plots, while preserving the data with negative sign (phase information).

2.5 Discussion

The linear circuit (Fig. 2.5) models the behavior of the annular waveguide with good accuracy, particularly when multiple network segments are cascaded, as depicted in Fig. 2.7.

As mentioned in Section 2.3.2, the single network segment inherently imposes a trade-off between the waveguide length L and the frequency bandwidth for which the approximation is acceptable. According to Fig. 2.7, the approximation is excellent in the low-frequency region, where the condition expressed by Eq. 2.30 is satisfied (N=1). The validity also extends to large values of the characteristic length l. It is worth noting that existing circuit solutions present modelling deficiencies, which negatively affect the behavior at low frequency, particularly in a closed-end configuration and for increasing

Symbol	Description	Value	Unit
P_0	Equilibrium pressure	$101.32 \cdot 10^3$	[Pa]
T_0	Equilibrium temperature	298.15	[K]
ρ_0	Equilibrium density	1.18	[kg/m^3]
μ	Dynamic viscosity	$18.6 \cdot 10^{-6}$	[Pa s]
Pr	Prandlt number	0.707	-
γ	Adiabatic index	1.4	-

TABLE 2.2: Parameter values used for both FEM and circuital simulations

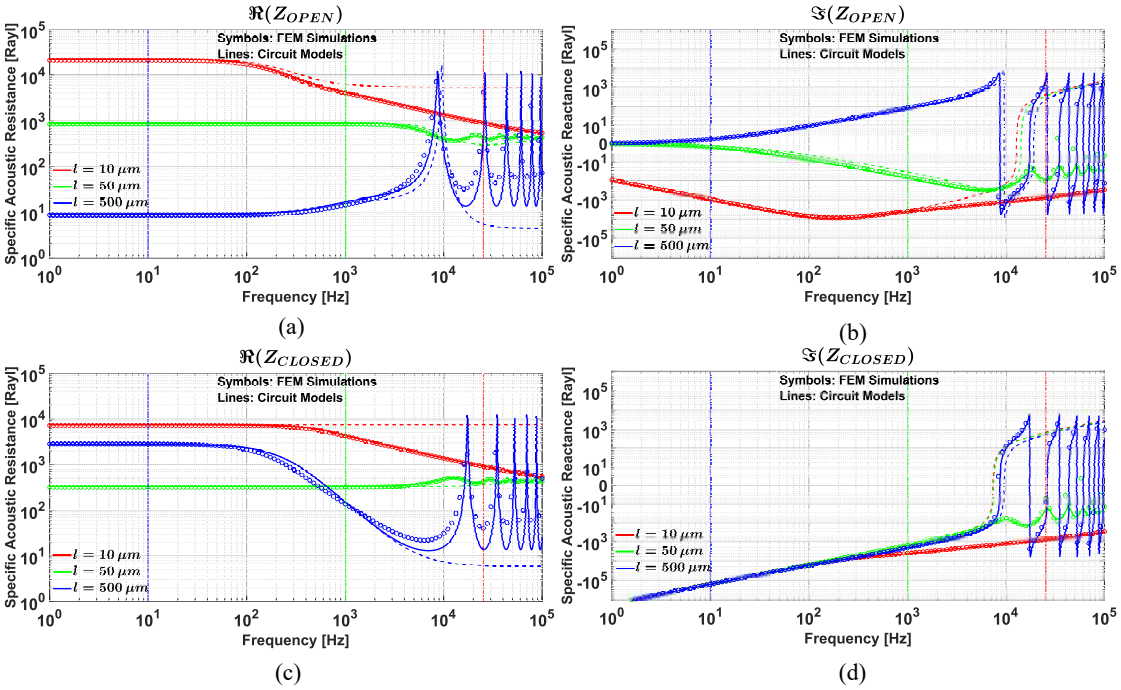

FIGURE 2.7: Circuit models (lines) and FEM-simulated (symbols) input specific acoustic impedance as a function of frequency. The annular waveguide has mean radius r_{m} and length L equal to 10 mm. The curves are computed according to the lumped-element circuit of Fig. 2.5, considering both 1 circuit segment of length L (dashed line) and 50 cascaded circuit segments, each of length $L' = L/50$ (solid line). Three configurations of annular waveguide width w and layer thickness t are considered, with $w = t = l$. The vertical lines correspond to $\tilde{s} = 1$. Open-ended boundary condition (top) with real part (a) and imaginary part (b). Closed-end boundary condition (bottom) with real part (c) and imaginary part (d).

l [69]. To this regard, the electrical resistance $R_{p,3}$ in the parallel branch of Fig. 2.5 exhibits a square dependence on l and is required for a correct approximation.

When multiple segments are cascaded, the equivalent waveguide length modelled by each segment reduces, and the validity of the resulting circuit is potentially extended also at higher frequencies. With reference to Fig. 2.7, the network segments are short enough to satisfy Eq. 2.30 in the whole analyzed bandwidth. It is worth noting here that the technique adopted to approximate the function B_Y during the derivation of the circuit greatly affects the quality of the result. The approximation of B_Y in the whole domain, through the Padé approximants, allows extending the validity of the circuit up to the frequency region in which wave propagation becomes inviscid and adiabatic, dominated by a reactive behavior with the presence of resonances (i.e. large $\tilde{s}$; approximately $\tilde{s} > 10$). The curves of Fig. 2.7 show that the resonance peaks are indeed correctly captured (N=50). On the contrary, existing circuital solutions are typically valid at low frequency and for small values of l (i.e. small $\tilde{s}$; approximately $\tilde{s} < 1$), since the hyperbolic tangent in B_Y is approximated with a low-order Taylor expansion **olson1947**, [72]. Due to this limit, the cascading of the network segments does not automatically translate in approximation improvements, for larger values of $\tilde{s}$.

The circuit developed in this work improves, or at limit preserves, the low-frequency accuracy of existing solutions. When $\tilde{s}$ is small (i.e. $\tilde{s} < 1$) , the circuit of Fig. 2.5 can be simplified by removing specific electrical components that locally behave as open-circuits, namely $R_{s,2}$, $R_{p,2}$, and $C_{p,2}$. The resulting circuit is equivalent to the one that would be obtained with a Taylor series expansion of the hyperbolic tangent in B_Y (with proper order). The performance of the circuit may slightly decrease for higher values of $\tilde{s}$, in agreement to the approximation quality of B_Y performed by the Padé approximants. While a punctual definition of the discrepancy is unpractical, the simulations demonstrate that the results are satisfactory also at higher frequencies.

In summary, the circuit represents a valid model of a short waveguide with annular geometry, within the bandwidth satisfying Eq. 2.30. The correct waveguide behavior at higher frequencies is well approximated by cascading multiple network segments, further motivating the validity of the circuit model.

The proposed circuit model presents several advantages with respect to a FEM-based simulation approach. The model can be implemented in circuit simulators, or even simple mathematical tools or programming languages, allowing for a fast evaluation of the waveguide behavior. The analysis of the effects of geometrical parameters variations is also simplified. On the contrary, the simulation of a specific physical design with a FEM tool represents a time consuming process, hampering the rapid inspection of alternative designs. Finally, a circuit model can be effectively used to integrate the waveguide component at a system level, adopting electroacoustic and electromechanical analogies [69]. The device engineering process is thus accelerated, in agreement with the previous considerations.

Chapter 3

Modeling of 3D-Printed Piezoelectric Microphone

In this chapter, a multiphysics lumped-element circuit model of the 3D-printed piezoelectric microphone is derived. The circuit model is meant to be a complementary tool with respect to the Finite Element Method (FEM) approach. FEM techniques provide accurate solutions by numerically solving coupled differential equations in several physical domains. However, they are generally computationally intensive and do not provide physical insights.

The circuit model exchanges fidelity for efficiency and transparency, allowing for a deeper understanding of the behavior of each element within the system. This allows, in turn, for an insightful inspection of the effects of geometrical parameters variations. Circuit models can also be implemented in a variety of tools and circuit simulators, allowing for a fast evaluation of the system performance.

3.1 Acoustic modeling

In this section, the electrical circuit modeling the acoustic domain is described. The acoustic domain is represented by the microphone internal cavities characterized by the presence of air, namely, the annular waveguide and the chamber hosting the pillar, as shown in Fig. 3.1. The annular waveguide will be called vent hereafter for convenience.

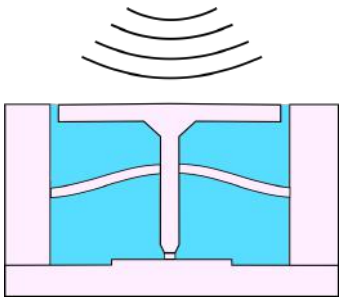

FIGURE 3.1: Acoustic domain

First, the circuit models of the vent and the inner chamber are described, treating them as individual components. Then, the coupling between the vent and the chamber is analyzed. Some considerations are drawn from such analysis, allowing for a simplification of the equivalent circuit model of the coupled elements. Finally, the complete circuit model of the acoustic domain of the microphone is presented.

3.1.1 Modeling of vent

A circuit model of the vent is derived from the study performed in chapter 2. The circuit analyzed in Fig. 2.5 relates the acoustic pressure and the particle velocity within the annular waveguide. Particle velocity corresponds to the local velocity of each fluid particle within the waveguide, irrespective of the waveguide cross-section. When analyzing a single acoustical component, the pair constituted by pressure and particle velocity allows for a convenient normalization of the cross-section, enabling the analysis of the insightful specific acoustic impedance.

A vent circuit model suitable for system-level integration is obtained by imposing the volume velocity as the flow quantity, as shown in Fig. 3.2. The volume velocity is defined as the rate of flow of the medium through a cross-sectional area:

$$U = Av \tag{3.1}$$

where U is the volume velocity, A the cross-sectional area and v the particle velocity. The volume velocity represents the correct flow quantity when modeling the interconnection of multiple components through an equivalent circuit, due to a twofold motivation. First, the volume velocity represents the quantity that is preserved at junctions between different acoustical elements having different cross-sections, due to conservation of mass. This is in analogy to electrical currents in the electrical domain, in which continuity is guaranteed by conservation of charge [69]. Secondly, volume velocity and pressure constitute power conjugate variables. The pressure-volume velocity pair is thus suitable for an effective multiphysics coupling by means of ideal transformers [69].

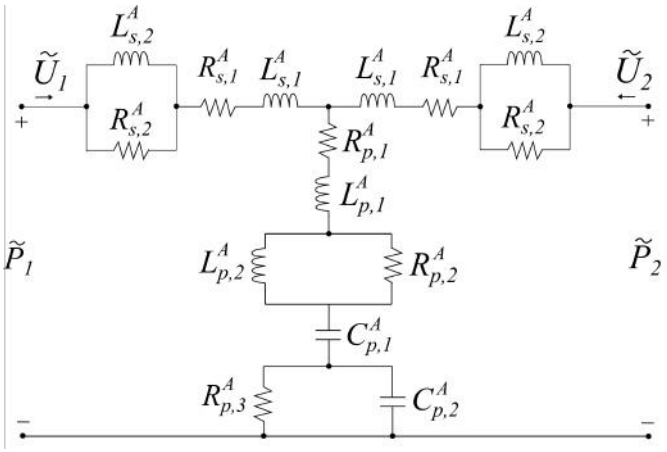

FIGURE 3.2: Circuit model of the vent.

The volume velocity within the annular vent is given by:

$$U_v = A_v v = \pi(r_o^2 - r_i^2)v \tag{3.2}$$

where U_v is the vent volume velocity and A_v the vent cross-sectional area. Hence, the specific acoustic impedances of Fig. 3.2 are transformed into acoustic impedances (A) as $Z_i^A = Z_i/A_v$. In terms of components values, $R_i^A = R_i/A_v$, $L_i^A = L_i/A_v$ and $C_i^A = C_i \cdot A_v$.

The vent is modeled through a single circuit segment, as shown in Fig. 3.2. As discussed in 2.3.2, the lumped-element approximation is valid when the vent length l_v modeled by the circuit is smaller than the acoustic wavelength ($l_v \leq 2\pi\lambda$). When thermoviscous effects are considered, the wavelength λ is described by a rather complex analytical form, which depends also on the vent width w (see 2.31).

When $l_v < 1$ mm, the lumped condition is satisfied up to approximately 20 kHz and for w>10 µm, covering the requirements of microphone applications. For the analysis which follows, we are going to assume $l_v = 1$ mm, unless otherwise stated. All the derived considerations are inherently valid also for shorter vent lengths.

3.1.2 Modeling of chamber

The boundary layer thickness at the lower limit of the audio bandwidth (20 Hz) is less than half a millimeter. Hence, the chamber can be considered sufficiently large such that thermoviscous losses are negligible for the whole bandwidth of interest, allowing for the simpler free-air propagation model.

The chamber can be modeled as a tube rigidly closed on one end, as shown in Fig. 3.3. The input acoustic impedance is given by [69]:

$$Z_c^A = \frac{-j\rho_0 c}{\pi r_c^2} cot(kl_c) \tag{3.3}$$

where ρ_0 is the density of air, r_c is the chamber radius, $k = w/c_0$ the wave number and l_c the chamber length. The truncated series expansion of the expression leads to:

$$Z_c^A = -j\frac{\rho_0 c_0^2}{V} + jw\frac{l_c\rho_0}{3\pi r_c^2} \tag{3.4}$$

where V is the chamber volume. The approximation is valid for $kl_c << 1$ or, equivalently, when the chamber length l_c is smaller than the acoustic wavelength λ. When the condition is met, the chamber can be approximated by the series of an acoustic compliance and mass, given by:

$$C_c^A = \frac{V}{\rho_0 c_0^2} = \frac{V}{\gamma P_0} \tag{3.5}$$

$$M_c^A = \frac{l_c\rho_0}{3\pi r_c^2} \tag{3.6}$$

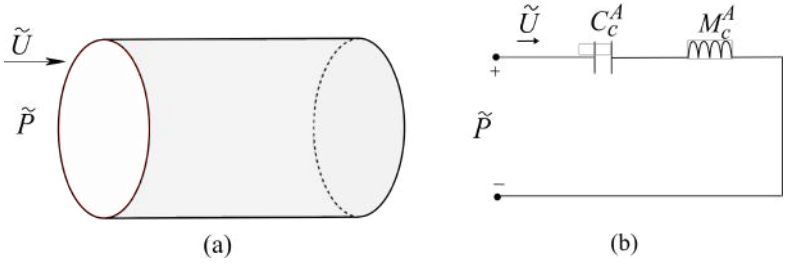

FIGURE 3.3: Circuit model of the acoustic chamber.

3.1.3 Acoustic coupling between the vent and the chamber

The general acoustic circuit representing the vent-chamber coupling is represented in Fig. 3.4. An input acoustic pressure is applied at the primary port of the vent, while the chamber represents the vent terminating impedance (i.e. load) at the secondary port. To a first approximation, the circuit impedances of Fig. 3.4 are those of the vent and chamber circuit models analyzed independently. The vent acoustic impedances Z_s^A and Z_p^A are obtained starting from the specific acoustic impedances of Eqs. 2.15 and 2.16 respectively, in which the simple impedance conversion described in section 3.1.1 is performed (Fig. 3.2). The chamber impedance Z_c^A is given by Eq. 3.4 (Fig. 3.3b).

In this section, the acoustic coupling between the vent and the chamber is analyzed in more detail. The analysis allows deriving an optimized version of the acoustic circuit, presenting some refinements and simplifications with respect to the simple cascading of the vent and chamber circuit models of Fig. 3.4.

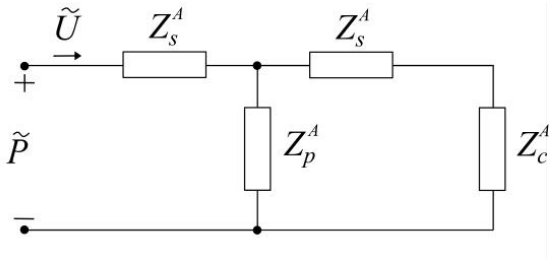

FIGURE 3.4: Equivalent circuit of vent-chamber coupling.

End correction

The junction between the vent and the chamber constitutes a significant cross-sectional area discontinuity for the acoustic flow, causing edge effects at the boundary. The air particles leaving the vent do not instantaneously disperse, but maintain their organized status for a certain distance within the chamber. The net effect is that the vent behavior is actually extended beyond its physical length, due to non-ideal boundary conditions. This phenomenon can be implemented within the lumped circuit model through an *end correction*, consisting in the adjustment of the equivalent vent acoustic mass by adding a short length term [69], [75]. The entity of the correction depends on the boundary type. For instance, a tube radiating in open air would require less correction than a tube terminating in an infinite baffle (i.e. flanged tube), since the air particles would disperse more rapidly.

The end-correction of the vent is performed by approximating its geometry with a flanged slit, consisting of plain, parallel layers terminating in an infinite baffle. The added length becomes [76]:

$$\Delta l_v \approx 0.85w \tag{3.7}$$

The length Δl_v is added to all the acoustic mass expressions (i.e. inductances) of the vent circuit of Fig. 3.2. The parallel layers geometrical approximation is shown to be valid in section 3.1.1. The infinite baffle assumption results in a conservative correction,

since the vent is actually closed on the external side at the joint. However, FEM simulations show that the approximation is valid, representing a very good compromise between analytical complexity and correctness of the result.

Simplification of coupled circuit

As shown in the equivalent circuit of Fig. 3.4, the chamber implements the vent load impedance. The entity of the load greatly affects the overall acoustic behavior, as demonstrated by the vent analysis with the closed-end and open-end boundary conditions in section 3.1.1. In the following, the equivalent circuit is analyzed in more detail, in order to assess whether a simplification can be made when the load takes the form of an acoustic chamber.

Figure 3.5 shows a comparison of the impedance magnitude of the vent parallel branch $|Z_p^A|$ and the load branch $|Z_s^A + Z_c^A|$. A significant magnitude difference of the confronted impedances, in parallel configuration, may enable circuital simplifications. In particular, if $|Z_s^A + Z_c^A| << |Z_p^A|$, the vent parallel branch can be neglected.

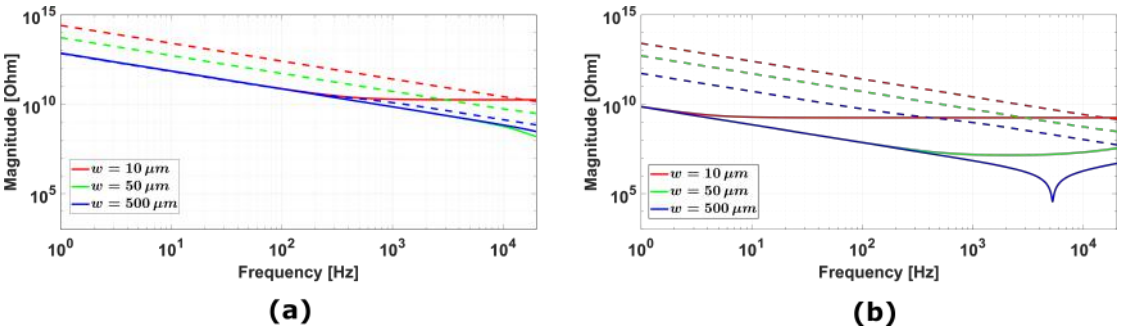

FIGURE 3.5: Acoustic impedance analysis of the vent-chamber coupling according to the circuit of Fig. 3.4. The magnitude $|Z_p^A|$ (dashed line) is compared to $|Z_s^A + Z_c^A|$ (solid line), for varying vent widths (w) and chamber dimension (r_c, l_c). (a) Chamber with $r_c = l_c = 0.1$ cm and (b) Chamber with $r_c = l_c = 1$ cm

In the low-frequency region, the acoustic impedance of the chamber $|Z_c^A|$ is mainly that of a compliance (i.e. capacitance), having the characteristic slope of 20 dB/decade. In this region, $|Z_s^A + Z_c^A| << |Z_p^A|$, unless extremely small chambers are considered, with a volume comparable to that of the vent (e.g. $r_c = l_c$=1 mm and w=500 µm). More insights can be gained by the low-frequency equivalent circuit of Fig. 3.6. The analytical expression of the two involved capacitances is very similar, differing only by a factor $\gamma \approx 1.4$. As a result, the vent and chamber volumes represent the main discriminant. For practical chamber volumes, the condition $|Z_s^A + Z_c^A| << |Z_p^A|$ is thus satisfied at low frequency.

At high frequencies, the inertial effects modeled by the vent and chamber inductances becomes increasingly relevant, eventually dominating over the low-frequency elastic behavior. Fortunately, as shown in Fig. 3.5, this turnaround occurs in the higher end of the audio spectrum or above, without significant behavioral shifts. The confronted impedances become comparable only for very narrow vent widths w at high

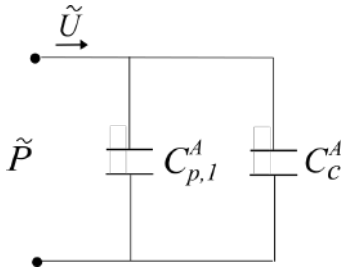

FIGURE 3.6: Equivalent circuit of the vent-chamber coupling at low frequency.

frequencies. In this case, significant viscous losses in the vent increase the series resistance, leading to $|Z_s^A| \approx |Z_p^A|$. This effect is independent from the chamber, as demonstrated by the figure plots. Fortunately, the impedances become comparable only at the limit of the audio bandwidth, also for values of w close to the limit of validity of the developed vent circuit model (see section 3.1.1).

By virtue of all the previous considerations, the impedance term Z_p^A can be neglected for the given application domain.

3.1.4 Final microphone acoustic circuit

Figure 3.7 depicts the final acoustic circuit of the microphone, where:

$$R_{v1}^A = \frac{12\mu l_v}{w^2 A_v} \tag{3.8}$$

$$L_{v1}^A = \frac{\rho_0 (l_v + \Delta l_v)}{A_v} \tag{3.9}$$

$$R_{v2}^A = \frac{18\mu l_v}{w^2 A_v} \tag{3.10}$$

$$L_{v2}^A = \frac{\rho_0 (l_v + \Delta l_v)}{5 A_v} \tag{3.11}$$

P_d denotes the difference between the external acoustic pressure and the chamber pressure.

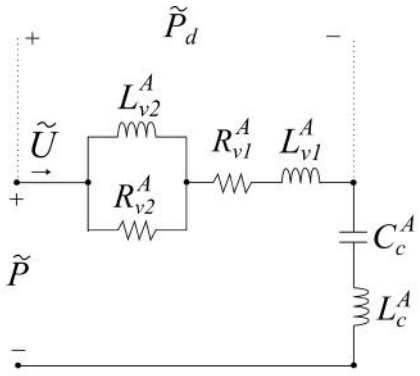

FIGURE 3.7: Circuit model of the microphone acoustic domain.

Model validation

A FEM model of the acoustic domain, constituted by the vent and the chamber, has been developed in COMSOL Multiphysics 5.3a for the validation of the circuit of Fig. 3.7. A two-dimensional (2D) axisymmetric model is selected, in agreement with the system structure. The geometry consists of two adjacent rectangular air domains, corresponding to the vertical cross-sections of the vent and the chamber, respectively. Thermo-viscous acoustics equations are solved in the vent, while the simpler pressure acoustics equations are considered for the chamber. A multiphysics coupling is added at the joint between the two domains.

Figure 3.8 compares the chamber pressure (i.e. load voltage) computed according to the circuit of Fig. 3.7 with the results provided by the FEM simulations. Two different chambers are considered, with dimensions compatible with the target 3D-printed microphone application. A pressure load of 1 Pa is applied at the entrance of the vent. The plots show a good overall agreement between the circuit and the FEM simulations, validating the model refinement process for the target application.

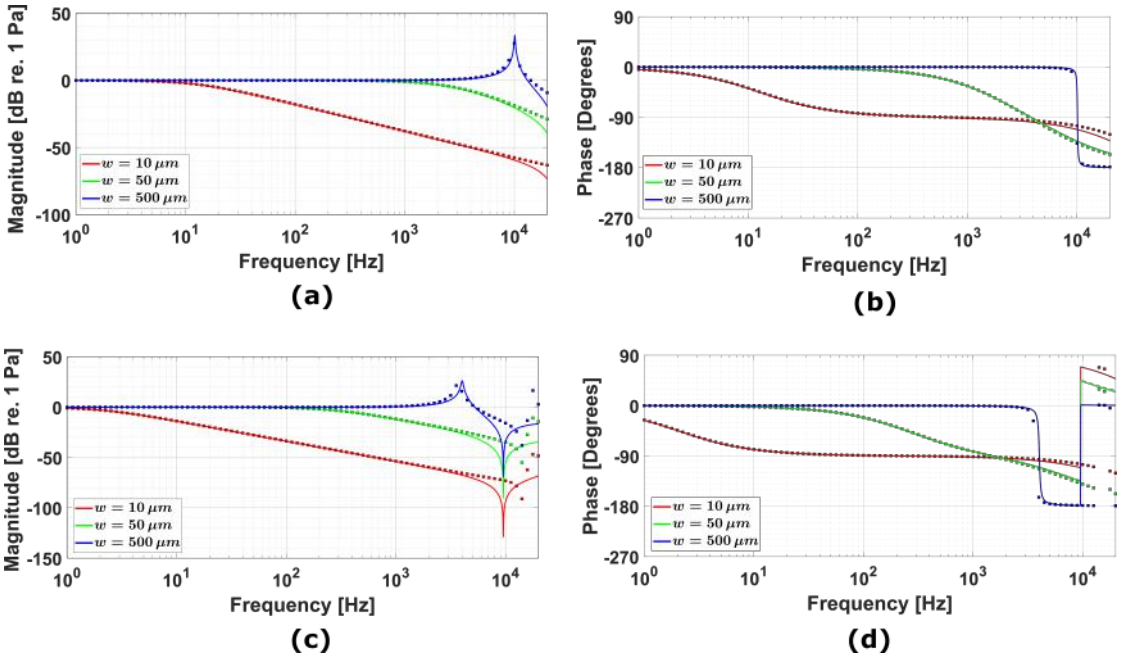

FIGURE 3.8: Circuit model (lines) and FEM-simulated (symbols) chamber acoustic pressure as a function of frequency. A pressure load of 1 Pa is applied to the vent entrance. Pressure magnitude (a) and phase (b) with chamber dimensions $r_c = l_c = 0.4$ cm. Pressure magnitude (c) and Phase (d) with chamber dimensions $r_c = l_c = 1$ cm

Slight discrepancies can however be observed above 10 kHz for the bigger chamber. The problem is not related to the coupling, but rather to the chamber model itself (see section 3.1.2). A chamber size of a few centimeters represents the upper bound for the definition of a valid lumped-element model, since the chamber dimensions become comparable to the acoustic wavelength at frequencies lying within the audio bandwidth. As a consequence, increasing the chamber size further would decrease the bandwidth of good approximation. A detailed inspection of FEM simulations revealed the onset of complex pressure patterns at high frequencies, confirming the hypothesis.

Fortunately, the observed discrepancy is not problematic in practice. The quantity of interest for a proper operation of the microphone is the differential pressure, determining the net force acting on the plate. Hence, it represents also the quantity that is tightly coupled to the mechanical domain in the complete multiphysics model. The differential pressure is the difference between the external acoustic pressure, acting on top face of the plate, and the chamber pressure, acting on the bottom face. At high frequencies, the chamber pressure decreases and becomes negligible compared to the external pressure, limiting the effects of modeling discrepancies. The dB-magnitude of the differential pressure can be defined as:

$$P_d = 20 \cdot log_{10}(|P_i - P_c|) \tag{3.12}$$

where P_i is the external pressure and P_c the chamber pressure (both harmonic). Figure 3.9 shows the differential pressure magnitude acting on an idealized fixed top plate, with a harmonic load of 1 Pa applied to both the vent and the plate. As shown in the figure, the effect of the previously described modeling discrepancy at high frequencies is negligible.

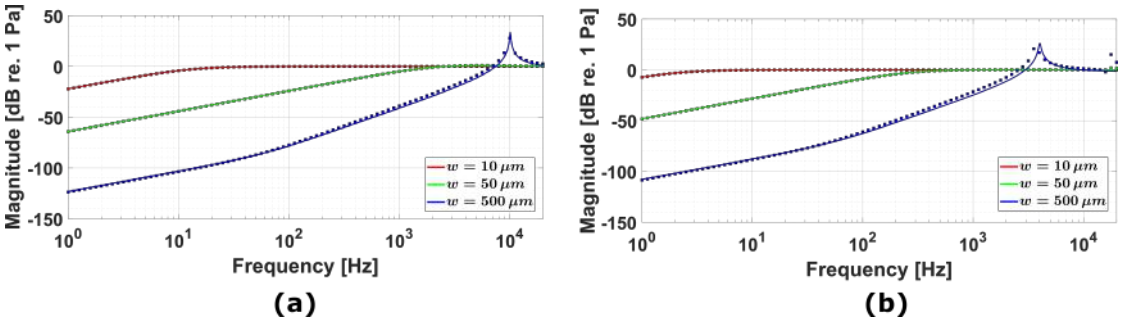

FIGURE 3.9: Circuit model (lines) and FEM-simulated (symbols) differential pressure magnitude on the top plate as a function of frequency. A pressure load of 1 Pa is applied to both the vent entrance and the plate (the latter assumed fixed). (a) chamber dimensions $r_c = l_c = 0.4$ cm and (b) chamber dimensions $r_c = l_c = 1$ cm

Figure 3.9 already shows that a functional microphone requires a very small vent width w. The ideal working condition is obtained when $P_d \approx P_i$. Assuming $P_i = 1$ Pa, as in figure, then the optimal condition becomes $P_d = 0$ dB. Increasing the vent width w progressively reduces the bandwidth where the operation is optimal. A bigger chamber size tends instead to increase such bandwidth, since more acoustic flow is required to fill the volume and build up the internal pressure or, equivalently, to "charge" the capacitance.

3.2 Mechanical modeling

In this section, the electrical circuit modeling the mechanical domain is derived. A purely mechanical lumped-element model constituted by springs, masses and dampers is first described. The obtained model is then translated into the electrical equivalent to perform the multiphysics coupling.

The microphone mechanical domain is represented by the moving 3D-printed structure and the compressed elements underneath, as shown in Fig. 3.10. The involved parts are the top plate, the pillar, the preload spring and the piezoelectric film.

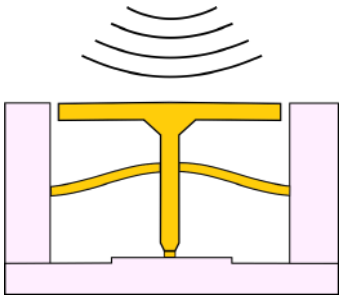

FIGURE 3.10: Mechanical domain

3.2.1 General modeling considerations

Mechanical lumped-element models can be categorized according to the number of Degrees Of Freedom (DOF), corresponding to the total number of displacement coordinates required to describe the vibration of the system. The given number of coordinates should describe the position of all the model masses, at any instant of time. For this reason, the number of DOF is also equivalent to the allowed movements of the lumped masses [77].

Generally, a Single Degree Of Freedom (SDOF) model is sufficient to provide a reasonable description of the system, as shown in Fig. 3.11a. In the model, one mass is connected to a rigid wall by means of a spring and eventually a dash pot. One coordinate is sufficient to describe the system vibration, occurring in a single direction.

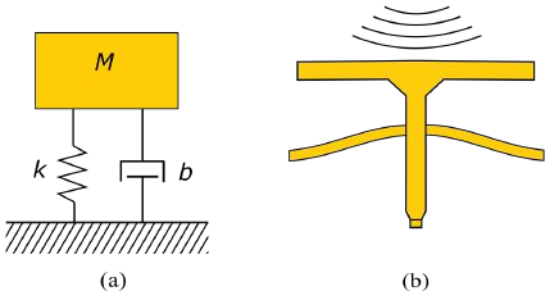

FIGURE 3.11: (a) SDOF mechanical model and (b) identification of the lumped mass in the microphone design.

A SDOF model is sufficient to describe the microphone dynamics if the elements of the moving structure having most of the mass approximately displace in a single direction and with the same entity. In this case, the entire moving mass can be lumped together, and the common displacement can be modeled with a single equivalent spring. This is a reasonable approximation, for instance, when a perfectly rigid top plate is assumed. In this case, most of the moving mass is concentrated in the plate and the pillar, which undergo a nearly common displacement during vibration 3.11b. The motion is also affected by the nearly massless elements underneath, which participate as a simple equivalent spring.

Unfortunately, the top plate is unlikely to behave as a rigid body. Instead, the limited flexural rigidity causes the plate to bend at the border during vibration. The flexural rigidity provides a measure of bending resistance, defined as:

$$D = \frac{Y_p t_p^3}{12(1-\nu_p^2)} \tag{3.13}$$

where Y_p and ν_p are the plate material Young Modulus and Poisson's ratio, respectively, while t_p is the plate thickness. It is evident that the plate resistance to bending depends on both the material and the geometry. The thermoplastic materials typical of 3D-printing are characterized by a low Young Modulus ($\approx 1-2\,GPa$), making the plate susceptible to bending, unless very thick (and massive) structures are adopted.

The bending phenomenon can be modeled through a two DOF system, as shown in Fig. 3.12a. The mass and spring realizing the additional degree of freedom are coupled to the plate border. During plate bending, in fact, the periphery undergoes a significant displacement, greater than the section close to the axis of symmetry, as shown in Fig. 3.12b. The additional lumped elements enable the modeling of the described motion, with important consequences on the vibration dynamics, particularly concerning the resonances and the microphone bandwidth.

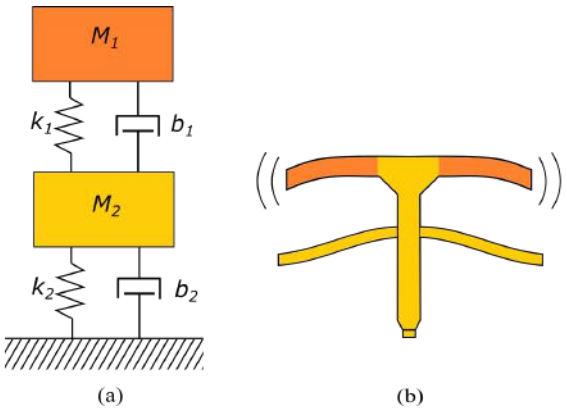

FIGURE 3.12: (a) Two DOF mechanical model and (b) identification of the lumped masses within the microphone design.

In the following, the simpler SDOF mechanical model is first described, assuming a rigid plate. Next, the plate bending behavior is modeled through a further SDOF mechanical system. Finally, the two models are properly combined, allowing for the definition a two DOF system accounting for the plate bending phenomenon.

The models will also include lumped-elements associated with damping. However, damping properties are generally estimated from experimental measurements, meaning that dampers values are expected to be fitted accordingly. It is worth noticing that the knowledge of the damping properties would allow, in turn, for the analysis of the thermo-mechanical noise of the system, exploiting the same types of mechanical models just described [78].

3.2.2 SDOF mechanical model of the microphone with rigid plate

To a first approximation, the microphone can be modeled as in Fig. 3.13a. The entire mass of the moving structure is lumped together, realizing the SDOF model. The

springs are coupled to different sections of the moving structure, according to their physical configuration (Fig. 3.13b). As stated previously, an infinite flexural rigidity is assumed for the top plate, so that no bending occurs.

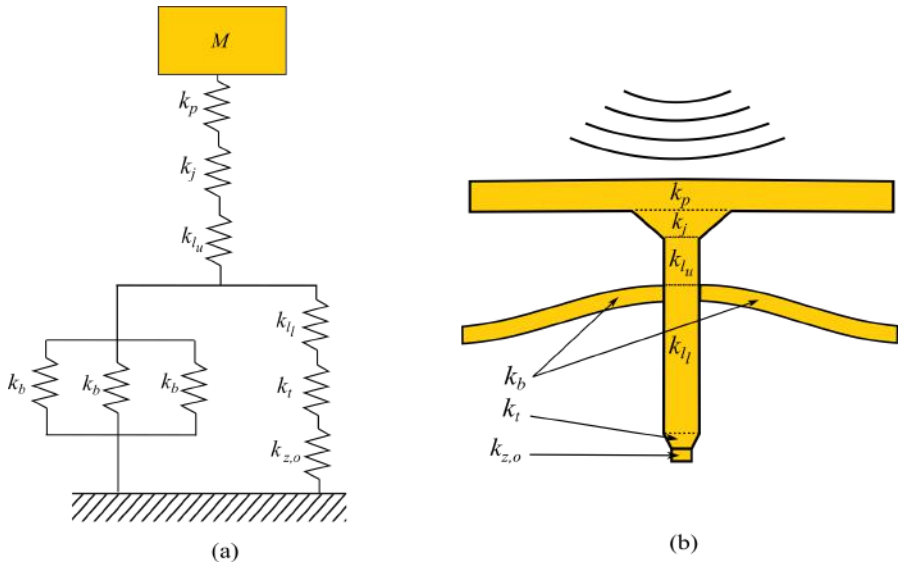

FIGURE 3.13: (a) SDOF mechanical model of the microphone with equivalent system of springs and (b) spring identification within the microphone design (damper not shown for clarity).

Model description

The three small beams realizing the preload spring, each of stiffness k_b, connect directly the pillar to the rigid microphone chassis. The beams are characterized by the same mechanical boundary conditions, thus, the related model springs are in parallel configuration. The contact point between the beams and the pillar defines the junction of the model springs, represented by the horizontal bar in Fig. 3.13. Traversing the moving structure from the junction point to the enclosure, the lower pillar section, the pillar tip and the piezoelectric film are encountered. The three elements are modeled as three springs in series configuration, with stiffness k_{l_l}, k_t and $k_{z,o}$, respectively. Traversing the moving structure from the junction point to the top, the upper pillar section, the plate support and the top plate are encountered. Again, the elements are modeled as three springs in series, with stiffness k_{l_u}, k_j and k_p, respectively.

The apparently complex structure of springs can be transformed into a single equivalent spring exploiting well-known series and parallel operations. As a result, the structure of Fig. 3.11 is obtained.

The lumped mass simply corresponds to the sum of the masses of the plate, the plate support, the pillar, the tip, and the beams realizing the preload spring. The beams are clamped at one end and their mass do not participate entirely to the vibration. Hence, only half of the the beams mass is considered. The mass of the piezoelectric film is negligible. The total mass is thus given by:

$$m = m_p + m_j + m_l + m_t + \frac{3}{2} \cdot m_b \tag{3.14}$$

The evaluation of the springs stiffness is more elaborated, being dependent on both the mechanical constraints and loading conditions. When a uniform pressure load is applied on the top plate, the element stack constituted by the top plate, plate support, pillar, tip, and piezoelectric film, can be considered uniformly axially loaded. In this case, each mechanical element supports the load over its entire cross-section, exhibiting pure compression or elongation. The top plate is assumed to have infinite flexural rigidity and behaves as the other components. The equivalent spring stiffness is given by the ratio of the force applied to the cross-section and the resulting displacement, mediated by the element Young modulus. The simplest case occurs when the cross-section of the element is constant. In this case, the associated spring constant is given by:

$$k_x = \frac{YA}{t} \tag{3.15}$$

where Y is the Young modulus of the material, while A and t are the cross-sectional area and the thickness of the element, respectively. The springs associated with the top plate, pillar (upper and lower sections) and piezoelectric film take this form, namely, k_p, k_{l_u}, k_{l_l} and $k_{z,o}$. For instance:

$$k_{l_u} = \frac{Y_{l_u} A_l}{t_{l_u}} \tag{3.16}$$

where A_l is the pillar cross-sectional area. The mechanical stiffness of the piezoelectric element is generally non-isotropic and dependent on the electrical boundary conditions. For mechanical analysis, a piezoelectric layer without electrodes is considered, corresponding to an open-circuit condition. The elastic constant becomes:

$$k_{z,o} = \frac{c_{33}^{D=0} A_z}{t_z} \tag{3.17}$$

where $c_{33}^{D=0}$ is the 33 component of the stiffness matrix. The piezoelectric definition is specialized in section 3.3.1, where a complete model for multiphysics coupling is defined.

The plate support and the tip are characterized by a truncated cone geometry. In this case, the different cross-sections of the cone have a different rigidity, and a uniform load would cause a variable strain throughout the element. The equivalent spring stiffness can be computed according to an integral method as shown in [79], leading to:

$$k_x = \frac{\pi Y r_1 r_2}{t} \tag{3.18}$$

where r_1 and r_2 are the radii of the two bases of the truncated cone. The springs associated with the plate support and the tip take this form, namely, k_j and k_t.

The stiffness k_b of each beam constituting the preload spring can be derived from the analysis of its free body diagram, as shown in 3.14.

A fixed constraint is applied at one end, modeling the rigid connection of the beam to the microphone chassis. A roller constraint is instead assumed at the other end, where the beam is connected to the pillar, and is free to move vertically. Each beam is loaded at the pillar position by a given force F_b, resulting from the load exerted on

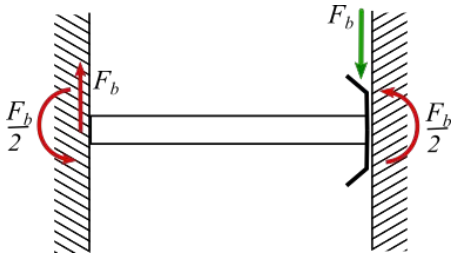

FIGURE 3.14: Free body diagram of a single beam of the preload spring

the top plate. According to the described model, the maximum vertical displacement occurring at the end of the beam is equal to:

$$w = \frac{F_b l_b^3}{12 Y_b I_b} \tag{3.19}$$

where Y_b is the Young Modulus of the beam, l_b its length and I_b its moment of inertia. For a rectangular cross-section, the moment of inertia becomes:

$$I_b = \frac{b_b t_b^3}{12} \tag{3.20}$$

where b_b and t_b are the beam width and thickness, respectively. The beam stiffness at the pillar junction is the ratio between the applied force and the resulting displacement:

$$k_b = \frac{F_b}{w} = \frac{12 Y_b I_b}{l_b^3} \tag{3.21}$$

Each beam is loaded at the pillar position by a fraction of the total force F exerted on the top plate. Due to symmetry considerations, a configuration of N equally distributed beams would result in a force equal to $F_b = F/N$ applied at each beam end. With $N = 3$, the equivalent stiffness of the whole preload spring is thus:

$$k_s = \frac{F}{w} = \sum_{i=1}^{3} k_{b_i} = \frac{36 Y_b I_b}{l_b^3} \tag{3.22}$$

Equivalent electrical circuit

The SDOF mechanical model suitable for multiphysics coupling, along with its electrical equivalent, are shown in Fig. 3.15. The piezoelectric terminals can be connected to the two-port piezoelectric circuit described in section 3.3.1. The equivalent stiffness terms are:

$$k_u = \frac{1}{\frac{1}{k_{l_u}} + \frac{1}{k_j} + \frac{1}{k_p}} \tag{3.23}$$

$$k_d = \frac{1}{\frac{1}{k_{l_l}} + \frac{1}{k_t}} \tag{3.24}$$

The total equivalent stiffness of the SDOF model (Fig. 3.11) is:

$$k = \frac{k_u k_{ds}}{k_u + k_{ds}} \tag{3.25}$$

with:

$$k_{ds} = k_s + \frac{k_d k_{z,o}}{k_d + k_{z,o}} \tag{3.26}$$

The equivalent electrical circuit is simply derived with $L^M = m$, $R^M = b$, and $C_i^M = 1/k_i$.

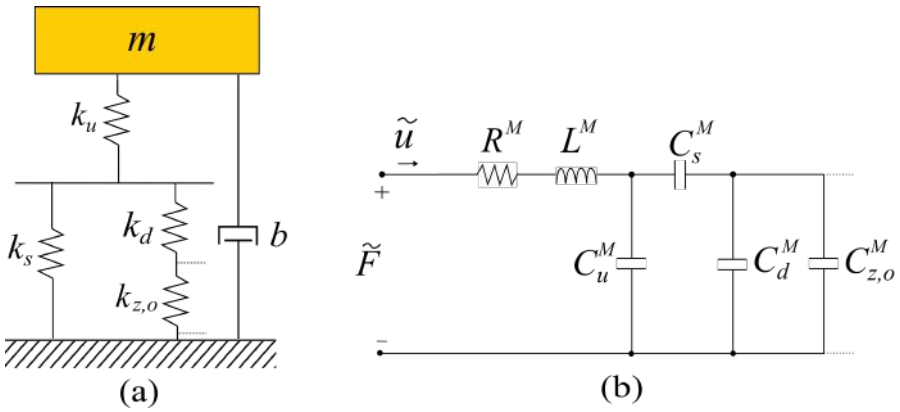

FIGURE 3.15: Model of piezoelectric microphone suitable for multi-physics coupling. (a) Mechanical model and (b) equivalent electrical circuit.

3.2.3 SDOF mechanical model of bending plate

In this section, the plate bending behavior is modeled through an equivalent SDOF mechanical system. A proper modeling of this behavior is required to identify correctly the microphone frequency response. The main tangible effect of the plate deflection is a shift of the resonant modes of the system, causing in turn a modification of the microphone performance. The frequency corresponding to the first resonant mode, in particular, defines an upper limit for the operational bandwidth of the microphone. Close to this frequency, the relationship between the applied acoustic load and the mechanical response becomes highly non-linear, determining in turn a non-linear sensitivity.

The lumped elements of the two DOF model are identified as shown in Fig. 3.12b. The additional SDOF model is associated with the section of the plate free to deflect, external to the pillar joint and having annular cross-section. This area will be called annular plate henceforth for convenience.

The quantification of the additional lumped elements, associated with the annular plate, is complicated by the behavior of the plate during bending. The uniform loading of the plate causes a deflection with a nearly parabolic profile, characterized by a vertical displacement that varies for each point of the plate cross-section. Hence, a complete description of the plate vibration would require, in principle, multiple (infinite) degrees of freedom.

The generalized SDOF method can be adopted to approximate the first mode of vibration of the annular plate through equivalent lumped elements [80]. The constituted

model can then be coupled to the SDOF model associated with the remaining part of the microphone mechanics, similar to that analyzed in section 3.2.2.

Generalized SDOF method

The method assumes a deflection profile consistent with the eigenshape characterizing the first fundamental frequency, allowing a description of the vibration problem through a single generalized coordinate. The displacement w at every point of the plate annular cross-section is given by:

$$w(r,t) = z(t)f(r) \tag{3.27}$$

with r being the radial direction, z the generalized coordinate and $f(r)$ the assumed deflection profile. The symmetry of the annular plate allows expressing the shape function $f(r)$ with the sole dependency on the radial coordinate r. A reference radius r_0 is selected, such that $f(r_0) = 1$ and $w(r_0,t) = z(t)$. The coordinate z is thus related to the actual displacement magnitude at the reference radius. In the following, the outer radius is considered as reference, hence $r_0 = r_o$.

Neglecting damping, the motion is controlled uniquely by z as:

$$\tilde{m}\ddot{z} + \tilde{k}z = \tilde{P} \tag{3.28}$$

where $\tilde{m}$ is the generalized mass, $\tilde{k}$ the generalized stiffness and $\tilde{P}$ the generalized load, defined as:

$$\tilde{m} = \mu \int_0^{2\pi} \int_{r_i}^{r_o} f(r)^2 r \, dr \, d\theta \tag{3.29}$$

$$\tilde{k} = D \int_0^{2\pi} \int_{r_i}^{r_o} (f''(r))^2 r \, dr \, d\theta \tag{3.30}$$

$$\tilde{P} = p \int_0^{2\pi} \int_{r_i}^{r_o} f(r) r \, dr \, d\theta \tag{3.31}$$

where μ is the area density of the plate, D the flexural stiffness, p the uniform distributed load. For practical purposes, the generalized stiffness can be approximated as [81]:

$$\tilde{k} = k \frac{1}{A} \int_0^{2\pi} \int_{r_i}^{r_o} f(r) r \, dr \, d\theta \tag{3.32}$$

with k being the stiffness at the reference radius r_o, defined as the ratio between the total applied load and the resulting displacement. For a uniform distributed load p applied over the area A it becomes:

$$k = \frac{pA}{z_{f=0}} = \frac{F}{z_{f=0}} \tag{3.33}$$

where $z_{f=0}$ is the static deflection. Substituting Eqs. 3.29, 3.31 and 3.32 into Eq. 3.28 and multiplying by A, the following equation of motion is obtained:

$$\beta m_{ap} \ddot{z} + kz = F \tag{3.34}$$

where m_{ap} is the total mass of the annular plate and:

$$\beta = \frac{\int_0^{2\pi} \int_{r_i}^{r_o} f(r)^2 r \, dr \, d\theta}{\int_0^{2\pi} \int_{r_i}^{r_o} f(r) r \, dr \, d\theta} \tag{3.35}$$

The parameters of the equivalent SDOF model are the mass βm_{ap} and the stiffness k. The model is characterized by the same resonance frequency and reference displacement as the real system. In quasi-static conditions (i.e. $\ddot{z} \approx 0$), in fact, the displacement is given by $z = F/k$.

The evaluation of β requires the definition of the shape $f(r)$. The displacement profile is mainly determined by the mechanical constraints, defining the slope and deflection of the element at the boundaries. The annular plate can be considered clamped at $r = r_i$ and free at $r = r_o$. Hence, the deflection shape of a cantilever beam is assumed as [80]:

$$f(r) = \frac{3(r - r_i)^2}{2(r_o - r_i)^2} - \frac{(r - r_i)^3}{2(r_o - r_i)^3} \tag{3.36}$$

The quantity β becomes:

$$\beta = \frac{49\alpha + 215}{112\alpha + 308} \tag{3.37}$$

where $\alpha = r_i/r_o$ is comprised between 0 and 1.

The stiffness k is determined according to the static deflection of the plate at $r = r_o$, upon application of a uniform pressure p. The maximum deflection of the annular plate at $r = r_o$ is given by:

$$w(r_o) = \frac{k_1 p r_o^4}{D} \tag{3.38}$$

where k_1 depends on the ratio r_i/r_o and is comprised between 0 and 1 [82]. The stiffness k is thus:

$$k = \frac{AD}{k_1 r_o^4} \tag{3.39}$$

3.2.4 Final two DOF mechanical model of the microphone

Model description

The SDOF models of sections 3.2.2 and 3.2.3 are coupled together to realize the two DOF mechanical system. In the process, the mass and stiffness of the plate is distributed to the lumped-elements according to the clamping conditions. The lumped components of the two DOF model are given by (see also 3.2.2):

$$m_1 = \beta m_{ap} = \frac{49\alpha + 215}{112\alpha + 308} m_{ap} \tag{3.40}$$

$$k_1 = \frac{AD}{k_1 r_o^4} \tag{3.41}$$

$$m_2 = (m_p - m_{ap}) + m_j + m_l + m_t + \frac{3}{2} \cdot m_b \tag{3.42}$$

$$k_2 = \frac{k_u k_{ds}}{k_u + k_{ds}} \tag{3.43}$$

Electrical circuit

The equivalent electrical circuit model is shown in Fig. 3.16. A rigorous translation of the mechanical model would require two input ports, coupled to the forces acting separately on the two lumped masses, according to the respective plate cross-sections. However, the electrical circuit is simplified by assuming the total force being applied to m_1, allowing for the definition of a single electrical port coupled to the acoustic domain. The approximation is justified by the following observations. First, the system modes of vibration are load-independent [77], meaning that the same resonance frequencies are obtained by applying the total force on a single mass. Second, the quasi-static behavior is preserved, since the piezoelectric element undergoes the same total force. The two features characterizing the microphone mechanical response in the operating bandwidth are thus retained, allowing for the aforementioned simplification.

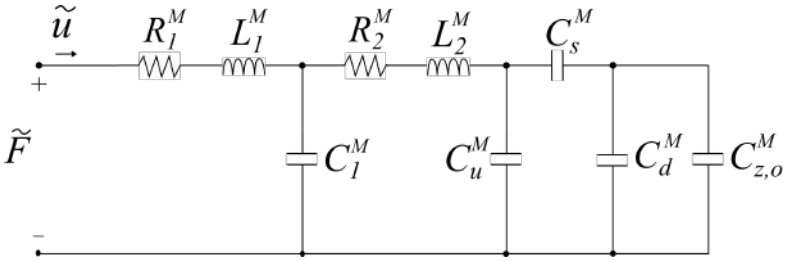

FIGURE 3.16: Equivalent electrical circuit of two DOF mechanical model of the microphone

Model validation

A FEM model of the microphone has been developed in COMSOL Multiphysics 5.3a for the validation of the circuit of Fig. 3.16. A three-dimensional (3D) model is selected, in agreement with the asymmetric system structure due to the preload spring. The model comprises the entire mechanical structure and solves for the displacement field.

The geometry is equivalent to that of the full microphone model, shown in Fig. 3.20. The materials associated with the moving structure and the piezoelectric layer are ABS and PVDF, respectively. The bottom enclosure is considered rigid.

Figure 3.17 shows the fundamental resonance frequency of the microphone as a function of the top plate thickness. All the other geometrical parameters are kept fixed during the analysis. The behavior of the decoupled SDOF models is added as a reference. The 2 DOF model agrees with simulation results and captures correctly the transition between the two asymptotic behaviors, described by the SDOF models. For very low thickness values, the largest displacements are observed in the plate periphery during bending. For high thickness values, the bending stiffness of the plate (i.e.D)

is very high, and the microphone behaves as a rigid piston. In this condition, the dynamics is correctly described by the SDOF microphone model with rigid plate.

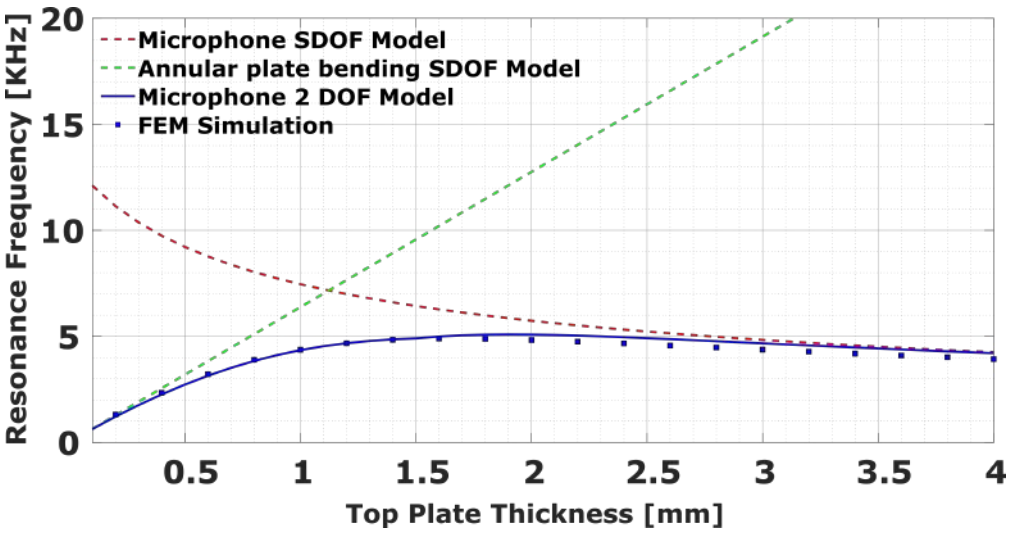

FIGURE 3.17: Mechanical resonance frequency of the microphone as a function of the top plate thickness.

3.3 Piezoelectric modeling

In this section, the electrical circuit implementing the microphone piezoelectric transduction is derived. A piezoelectric transducer is generally modeled as a two-port electrical network, coupling together the mechanical and the electrical domains [69], [83]. The network implements a scalar form of the piezoelectric constitutive equations, derived from the simplification of the complex tensorial relationships. To this purpose, a uniaxial stress state is generally assumed, as experienced by an unconstrained piezoelectric element subject to a vertical load. The piezoelectric film operating within the microphone assembly is instead clamped to a rigid substrate, generating a complex stress state within the material.

In the following, the circuit model of a piezoelectric transducer is first discussed. An effective piezoelectric coefficient for the clamped-film condition is then derived, suitable for integration with the aforementioned circuit.

3.3.1 Piezoelectric circuit model

The electrical model of a piezoelectric transducer is derived starting from the “strain-charge" form of the linear constitutive equations, reported here for convenience:

$$D = d\sigma + e_\sigma E \tag{3.44}$$

$$\varepsilon = s_E \sigma + d^T E \tag{3.45}$$

The linearity assumption is reasonable for microphone applications, considering the very small dynamic variations of both mechanical and electrical quantities. A

scalar form is obtained by imposing a set of electromechanical simplifying assumptions, which eliminate the couplings between orthogonal directions, as described in section 1.1.1. When uniaxially stressed thin films are considered, as in this case, then $\boldsymbol{E} = E_3$, $\boldsymbol{e} = e_{33}$, $\boldsymbol{\sigma} = \sigma_i$ and $\boldsymbol{s_E} = s_{ii}$.

Equations 3.44 and 3.45 in scalar form can be further manipulated as [69], [83]:

$$V = -\frac{1}{jwC_z^E} i + \frac{d}{C_z^E} F \tag{3.46}$$

$$F = \frac{1}{jwC_z^M} v + \frac{d}{C_z^M} V \tag{3.47}$$

where V is the voltage, F the internal force, v the velocity and i the electrical current. The force F is defined positive in compression. C_z^E and C_z^M are the electrical capacitance and mechanical compliance, respectively, given by:

$$C_z^E = \frac{e_\sigma A}{t} \tag{3.48}$$

$$C_z^M = \frac{t}{Y_E A} \tag{3.49}$$

where A is the cross-sectional area of the piezoelectric element, such that $\sigma A = -F$, t the thickness in the direction orthogonal to A, and Y_E the Young Modulus in short-circuit conditions. C_z^E is the electrical capacitance measured when the piezoelectric film is free to deform, such that no internal stress (force) is developed. C_z^M is the mechanical compliance measured when the piezoelectric film terminals are short-circuited.

It is worth noticing that C_z^E refers to the electrical capacitance of a simple parallel plate capacitor. A more elaborated and precise capacitance formulation can be derived by taking into account the fringing field, according to the specific geometrical configuration. However, the microphones fabricated in this thesis work are characterized by an equivalent electrical capacitance in which the side length (~1 mm) is much bigger than the separation distance, corresponding to the piezoelectric film thickness t (~40 µm, see chapter 4 for details). In this condition, fringing field effects can be reasonably neglected in favor of the simpler, classical formulation of Eq. 3.48 [84].

The constitutive equations 3.46 and 3.47 can be implemented with a two-port network, as represented in Fig. 3.18, where:

$$C_{z,o}^M = \frac{t}{Y_D A} = C_z^M - \frac{d^2}{C_z^E} \tag{3.50}$$

represents the mechanical compliance measured when the piezoelectric film terminals are open-circuited.

The two ports represent the mechanical and the electrical terminals, respectively. When used as sensor, a force or velocity is applied at the mechanical port and a voltage or current is measured at the electrical port. When used as an actuator, the opposite situation applies.

As anticipated, the network correctly models a condition of uniaxial stress. Assuming open-circuit boundary conditions at the electrical terminals, the voltage is:

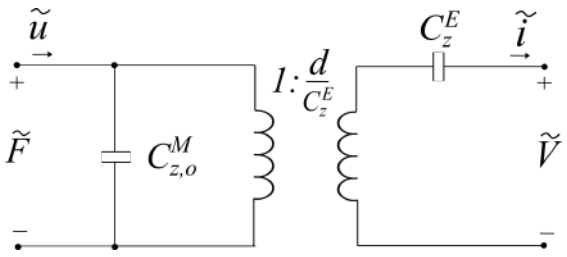

FIGURE 3.18: Two-port circuit model of piezoelectric transducer

$$V_{OC} = \frac{d\sigma t}{e} \tag{3.51}$$

which represents the typical result adopted for piezoelectric sensing applications [85]. However, when the piezoelectric element is used as a sensor, the complete stress state of the material affects the electrical domain. Hence, the uniaxial stress approximation of the model is accurate only if the piezoelectric element is not restrained during traction or compression.

3.3.2 Effective piezoelectric coefficient of clamped thin film

The microphone piezoelectric film is clamped to a rigid substrate and experiences a complex stress state during operation. In the following, an effective piezoelectric coefficient valid for orthotropic piezoelectric materials, like PVDF, is derived. The coefficient can then be adopted in the circuit of Fig. 3.18. The coefficient of interest is defined as:

$$d_{33,f} = \frac{D_3}{\sigma_3}|_{E_3=0} = d_{31}\frac{\sigma_1}{\sigma_3} + d_{32}\frac{\sigma_2}{\sigma_3} + d_{33} \tag{3.52}$$

where $s_{i,j}$ are the mechanical compliances in short-circuit condition. Similarly to the usual piezoelectric coefficient d_{33}, the effective coefficient $d_{33,f}$ relates the electrical displacement in the thickness direction to the mechanical stress in the cross-section orthogonal to the load. Differently from d_{33}, however, the contribution of the in-plane stress components is considered.

The stress ratios in Eq. 3.52 can be conveniently expressed in terms of the piezoelectric material parameters, by assuming an orthotropic piezoelectric film, like PVDF, perfectly bonded to a stiff substrate. Due to strain continuity, the two materials will experience a common lateral strain at the interface [86]. If the substrate has i) higher Young Modulus and ii) higher thickness, such lateral strain will be approximately equivalent to the free lateral strain of the substrate [87]. The limited film thickness permits to assume a uniform lateral strain on the vertical direction. Assuming an isotropic substrate we have:

$$\varepsilon_1 = \varepsilon_2 = -\nu_s \cdot \varepsilon_{3_s} = -\nu_s \cdot \frac{\sigma_3}{Y_s} = \sigma_3 \cdot s_{12_s} \tag{3.53}$$

where ε_1 and ε_2 are the in-plane strains of the film and the substrate, ν_s is the substrate Poisson's ratio and Y_s its Young Modulus.

With these assumptions, the piezoelectric constitutive equation 3.45 with $E = 0$ can be rearranged as:

$$s_{11}\frac{\sigma_1}{\sigma_3} + s_{12}\frac{\sigma_2}{\sigma_3} + s_{13} = -\frac{\nu_s}{Y_s} = k \tag{3.54}$$

$$s_{12}\frac{\sigma_1}{\sigma_3} + s_{22}\frac{\sigma_2}{\sigma_3} + s_{23} = -\frac{\nu_s}{Y_s} = k \tag{3.55}$$

which provides the solutions:

$$\frac{\sigma_1}{\sigma_3} = \frac{k(s_{22} - s_{12}) + s_{12}s_{23} - s_{22}s_{13}}{s_{11}s_{22} - s_{12}^2} \tag{3.56}$$

$$\frac{\sigma_2}{\sigma_3} = \frac{k(s_{11} - s_{12}) + s_{12}s_{13} - s_{11}s_{23}}{s_{11}s_{22} - s_{12}^2} \tag{3.57}$$

The coefficient $d_{33,f}$ can be adopted in place of d_{33} in the circuit model of Fig. 3.18. In addition, the clamped piezoelectric film operates in 33 mode, hence $Y_E = c_{33}^{E=0}$ in Eq. 3.49.

3.4 Final microphone circuit model

The complete lumped-element circuit model of the piezoelectric microphone is shown in Fig. 3.19

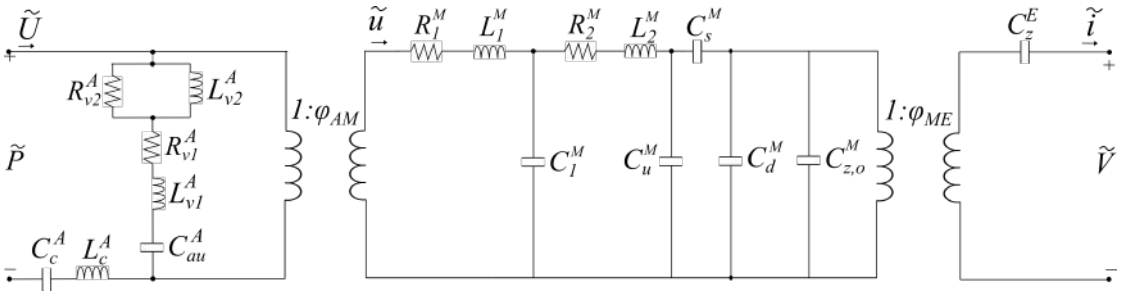

FIGURE 3.19: Circuit model of the piezoelectric microphone.

The circuit is obtained by assembling the sub-circuits analyzed in the previous sections, with the additional correction described in 3.4.1. The turn ratio of the transformer coupling the acoustical and mechanical domains is simply given by:

$$\phi_{AM} = A_p \tag{3.58}$$

where A_p is the cross-sectional area of the plate. The turn-ratio of the transformer coupling the mechanical and electrical domains is derived in section 3.3.1 and is equivalent to:

$$\phi_{ME} = \frac{d_{33_f}}{C_z^E} \tag{3.59}$$

3.4.1 Acousto-mechanical coupling correction

The coupling between the acoustic and mechanical domains should consider also the force imparted to the mechanical structure even when a complete pressure equalization

occurs. The internal plate section area, affected by the chamber pressure, does not correspond to the plate section area exposed to the external acoustic stimulus. To a first approximation, the section of plate aligned with the pillar should always provide a plateau force equal to:

$$F_{au} = PA_{pl} \tag{3.60}$$

where P is the incident pressure and A_{pl} is the cross-sectional area of the pillar.

A superposition of the two acousto-mechanical coupling mechanisms, considered separately, is impractical. Instead, the asymptotic behavior of the acoustic circuit is corrected, to provide the plateau force to the mechanical side even in condition of perfect chamber pressure equalization. An additional capacitance C_{au} is added as:

$$C_{au} = \frac{1-\beta}{\beta} C_c \tag{3.61}$$

where $\beta = A_{pl}/A_p$, corresponding to the ratio between the pillar and plate cross-sections.

3.4.2 FEM validation

FEM model description

The complete circuit is validated against FEM simulations of the open-circuit sensitivity. A complete 3D model of the microphone has been developed with COMSOL Multiphysics 5.3a. The model includes the acoustical, mechanical and electrical domains. Figure 3.20a depicts the final geometry. The microphone is modeled as being already assembled, with the target preload. This allows the definition of a single object, to avoid highly nonlinear mechanical contact and friction phenomena between separated domains. Such modeling choice represents a faithful representation of the physical reality, since the assembled microphone is characterized by physical parts that maintain constant contact during operation.

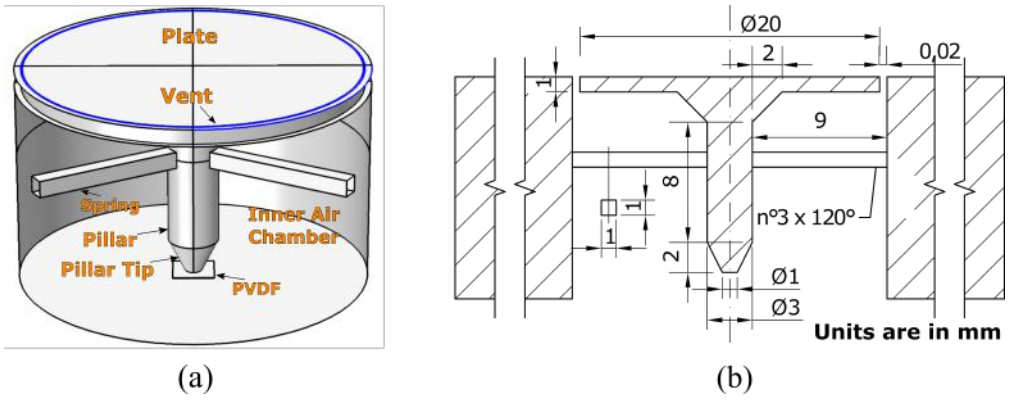

FIGURE 3.20: FEM geometry of the piezoelectric microphone. (a) 3D geometry representation (b) reference dimensions. The vent width is exaggerated for clarity.

The solid mechanics equations providing the displacement field are solved in all the structure except for the fluid-related domains. Electrostatic physics is solved in the

piezoelectric layer and electrodes, to capture the electrical response. Thermoviscous acoustics equations are solved in the vent area. The internal chamber is instead coupled to the simpler pressure acoustics physics, which neglects thermoviscous losses.

An acoustic-structure multiphysics coupling is added to the bottom surface of the top plate. The coupling captures the load exerted on the plate by the pressure developed within the internal chamber, as a result of equalization phenomena. A coupling is also added at the interface between the vent gap and the plate to account for the air damping. Finally, structural damping is added to the solid structure, with an isotropic loss factor ($\tan\delta$) of 0.02 associated with both ABS [88] and PVDF [89].

The solution of the thermoviscous acoustics equations represents by far the most computationally intensive activity, particularly for complex 3D models with many coupled physics. The meshing of the vent area is thus performed with ad-hoc strategies, to correctly capture the physical phenomena while retaining manageable computational complexity. For each frequency, the mesh is adapted to the boundary layer thickness in which thermoviscous effects develop, as shown in Fig. 3.21. In this way, a solution is always computed in several points in the radial direction and within the boundary layer, capturing correctly the phenomenon. At the same time, the meshing becomes coarser within the bulk, where a uniform acoustic field is present.

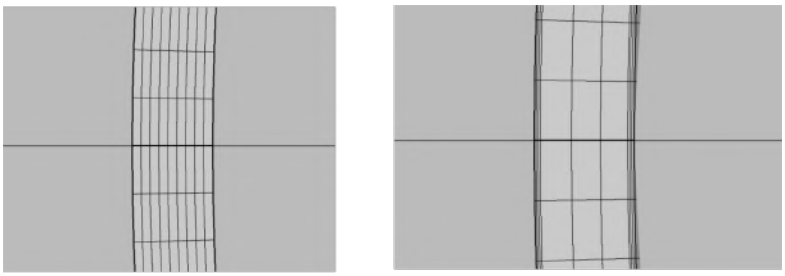

FIGURE 3.21: Meshing of the microphone vent according to the viscous boundary layer size. (a) Meshing at 20 Hz and (b) meshing at 20 KHz.

Validation

The open-circuit sensitivity of the lumped-element circuit model is validated against FEM simulations, for different microphone geometrical configurations. The vent width, plate thickness and tip radius are varied starting from the defined reference geometry of Fig. 3.20. In particular, each geometrical parameter is varied individually, while maintaining all the others fixed and consistent with the dimensions specified in Fig. 3.20b. The effects of the selected critical parameters on the microphone performance can then be evaluated and discussed. Table 3.1 shows the main material parameters used in both circuit and FEM simulations.

3.4.3 Discussion

Figure 3.22 depicts the computed microphone sensitivity for several values of vent width, plate thickness and tip radius. Overall, the circuit model provides correct results. The main model deficiency is represented by the inability to capture mechanical

antiresonances, situated outside of the microphone working bandwidth. As discussed in section 3.2.4, however, this design choice allows for a great simplification of the circuit model, avoiding multiple couplings (i.e. transformers) between the acoustic and mechanical branches.

The microphone vent creates, as expected, a detrimental high-pass filtering effect. The phenomenon affects increasingly higher frequencies for larger vent widths. Indeed, the vent and the chamber define an equalization time constant, which reduces when the vent width itself increases. For the target configuration, a challenging width of approximately 20 µm is required to ensure a cut-off frequency around 20 Hz, preserving the audio bandwidth.

Unfortunately, the vent width limit of 20 µm is hardly relaxed by means of geometrical tunings. The thermoviscous effects within the vent are substantially independent from the radii of the annulus, as analyzed in chapter 2. Moreover, the tuning of the equalization cut-off through larger chambers is largely impractical.

The effect of the plate thickness on the microphone response is largely discussed in section 3.2.4. Low thickness values decrease the fundamental resonance of the system because of excessive plate bending displacements. Similarly, high thickness values are detrimental, since the benefits of the increased flexural rigidity are nullified by the excessive mass.

The pillar tip radius is related to the solicited piezoelectric area and, in turn, to the area ratio of the microphone. A larger radius causes, as expected, a reduction of the microphone open-circuit sensitivity. Increasing the radius from 0.5 mm to 1.5 mm causes a reduction of the area ratio by approximately a factor 10 , as evidenced by the approximate 20 dB drop in the simulation.

Symbol	Description	Value	Unit
	ABS		
ρ_0	Density	1040	[Kg/m^3]
Y	Young Modulus	2.2	[GPa]
ν	Poisson's Ratio	0.35	[-]
	PVDF		
ρ_0	Density	1780	[Kg/m^3]
ϵ_r	Relative Permittivity (isotropic)	13	-
d_{31}, d_{32}, d_{33}	Piezoelectric Strain Constants	$25, 4, -35$	[pC/N]
d_{33_f}	Piezoelectric Strain Constant (clamped)	-11.9	[pC/N]
s_{11}, s_{22}, s_{33}	Short-Circuit Elastic Compliances (E=0)	$0.3, 0.33, 1.09$	[1/GPa]
s_{12}, s_{13}, s_{23}		$-0.13, -0.17, -0.17$	
c_{33}	Short-Circuit stiffness (E=0)	1.25	[GPa]
	Air		
ρ_0	Density	1.18	[Kg/m^3]
μ	Dynamic viscosity	18.6	[µPa s^{-1}]
γ	Adiabatic index	1.4	-

TABLE 3.1: Parameter values used for FEM and circuital simulations

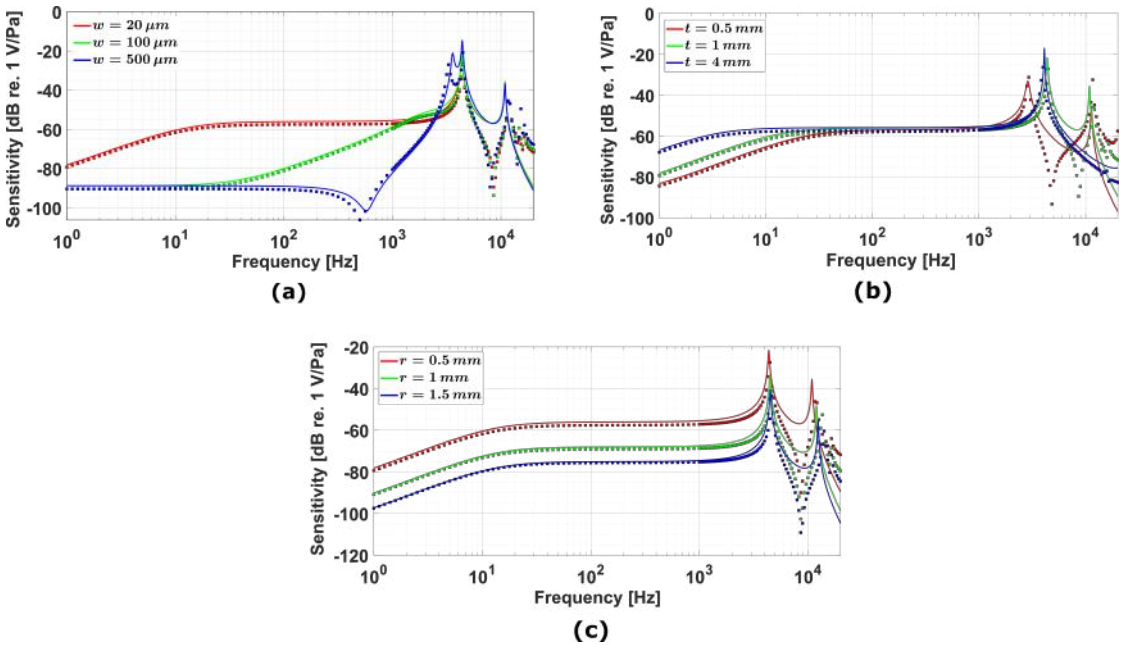

FIGURE 3.22: Circuit models (lines) and FEM-simulated (symbols) microphone sensitivity frequency response. The curves are computed according to the lumped-element circuit of Fig. 3.19. Several geometrical parameters are swept, starting from the reference configuration of Fig. 3.20b. Each parameter is varied individually, while maintaining all the others fixed and consistent with the geometric dimensions specified in Fig. 3.20b. Frequency response for different (a) vent widths w (b) plate thicknesses t and (c) tip radius r.

Chapter 4

Fabrication and Characterization of 3D-Printed Microphones

In this chapter, the fabrication and characterization of 3D-printed single-pillar microphones is described. The modeling insights of chapter 2 and 3 evidenced that the annular aperture (i.e. vent) constitutes the most critical component for a correct microphone operation. Three prototypes with variable vent width are thus realized to confirm the hypothesis. The sample with the smallest vent, trimmed by laser cutting, shows the best performance among the characterized samples, in agreement with the models.

4.1 Microphones fabrication

The microphone fabrication and assembly process is summarized in Fig. 4.1. CAD models of the mechanical part are designed in Solidworks (a) for 3D-printing, including the chassis, top plate, pillar and preload spring (b,c). A custom PCB is fabricated (d), integrating both the PVDF film and the conditioning circuitry. Finally, the microphone is assembled (e) by preloading the structure with a metallic bottom enclosure. In the following, the various fabrication steps are detailed.

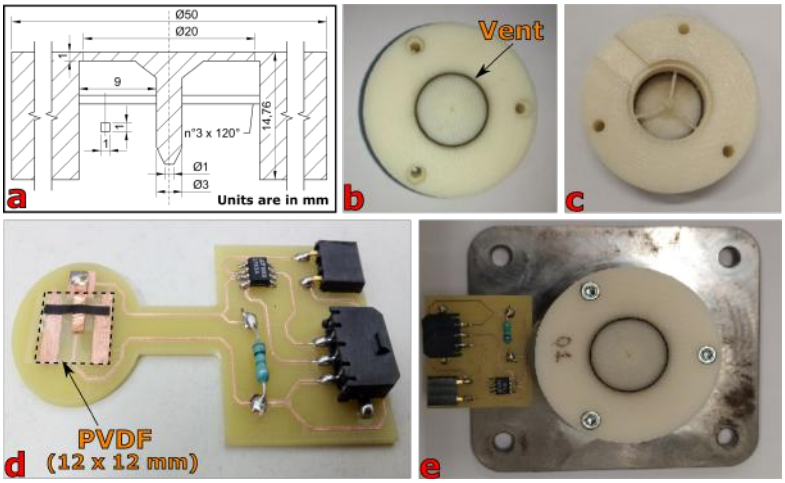

FIGURE 4.1: Fabrication and assembly process of the 3D-printed single-pillar piezoelectric microphone (laser-trimmed prototype taken as representative). (a) Section view of 3D-printed element, with geometrical dimensions in millimeters. (b) Top view and (c) bottom view of printed object. (d) PCB with PVDF film (left) and conditioning circuitry (right). (e) Assembly of the microphone.

4.1.1 3D-printed microphone

3D-Printer selection

A Stratasys Fortus 250mc (FDM) and a FormLabs Forms2 (SLA) 3D-printers were available for device fabrication (see section 1.2.2).

The Forms2 printer is characterized by higher resolutions and is generally better suited for the reproduction of fine details. However, the SLA technique requires the creation of a support structure for the object during fabrication, limiting the allowed geometrical complexity. The number and position of the supports is aided by a dedicated 3D-printer software and represents an important design step. The analysis showed that the target microphone geometry could not be correctly supported, particularly in the cavity, where the preload spring is present.

The more versatile Fortus 250mc was then selected as target 3D-printer. The printer deposits ABS plastic, model ABSplus-P430. A layer thickness of 0.254 mm and 100% infill (i.e. full solid) were selected for printing. The 100% infill parameter ensures that the mechanical properties of the printed details are preserved.

3D-printed prototypes

Three prototypes with vent thicknesses of 500 µm, 250 µm and 100 µm are targeted for fabrication and subsequent characterization. The other geometrical parameters are not varied between samples, to avoid the influence of additional factors in the experimental results. The reference design is shown in Fig. 4.1a.

The microphone design privileges sensitivity, by pushing the ratio between the top plate area and the pillar tip section area. This design choice is in agreement with the simulation results of section 3.4.2, which highlight how the tip radius, strictly connected to the area ratio, influences the sensitivity. Simultaneously, the microphone bandwidth is not significantly affected, unless the tip radius reaches extremely small values. The target circular top plate has a diameter of 20 mm (area of 314.16 mm^2), while the tip has a diameter of 1 mm (area of 0.785 mm^2), providing an area ratio of 400 The pillar tip diameter is selected as the smallest one able to guarantee satisfactory results, in order to guarantee sufficient voltage sensitivity. In this sense, preliminary tests showed that a diameter greater than the minimum printer specifications is required to obtain a nearly flat tip surface.

The width values of 500 µm and 250 µm are either compatible or very close to the 3D-printer clearance specification of 310 mm. The corresponding vent is thus foreseen within the 3D CAD design.

Figure 4.2 depicts the 3D-printed prototype with a vent width of 250 µm. The sample demonstrates satisfactory printing quality. Further inspection of the vent area through a microscope revealed no appreciable contact with the chassis.

The vent width of 100 µm requires a precision that lies too far beyond the printer clearance specification. The vent is instead realized through laser cutting, as described in 4.1.1. In such case, the top plate and the chassis are printed connected, without the gap required for the correct system mobility (see Fig. 4.1a). The plate is then released from the chassis through a subsequent circular laser-cut operation.

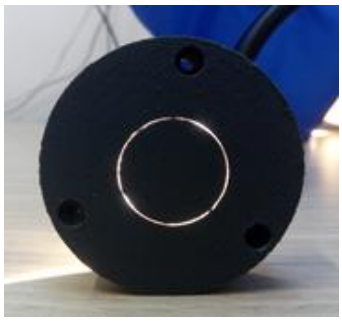

FIGURE 4.2: 3D-printed prototype with vent width of 250 µm

Laser trimming

The circular laser-cut operation is performed by an EKSPLA Atlantic UV1 ultrafast laser, able to produce a 355 nm UV beam with pulse duration below 10 ps. The pulse repetition rate (PRR) is 100 kHz and the pulse energy 10 µJ. The laser beam is focused through a 104 mm f-theta lens with a nominal spot diameter of 7 µm. The 1 mm thick plate is cut in the thickness direction through 20 steps of 250 cycles each, at a scanning speed of 125 mm/s. At every step, the focus is shifted on the z-axis by 50 µm. The process is repeated 10 times, increasing the cutting radius of 10 µm at every step to obtain a gap width of 100 µm in the radial direction. The target gap spacing provides the required tolerance during the assembly to avoid friction.

Figure 4.3 depicts the trimmed prototype having a vent width of 100 µm.

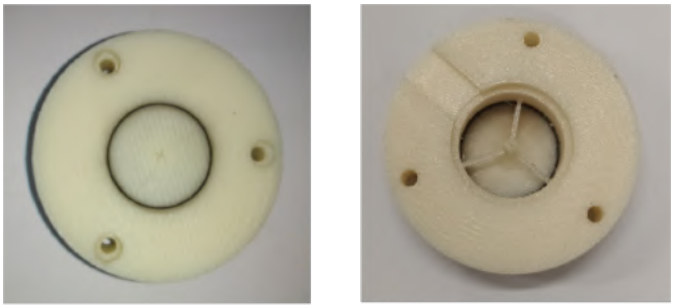

FIGURE 4.3: 3D-printed prototype trimmed by laser cutting, having vent width of 100 µm. (a) Top view and (b) bottom view.

4.1.2 Printed Circuit Board (PCB) design

A Printed Circuit Board (PCB) was designed to implement the electrical part of the sensor and simultaneously provide a rigid substrate for the moving part of the 3D-printed element. The piezoelectric film is bonded to one side of the PCB. The active area of the film is placed in contact with the pillar during the assembly of the device. The film is also electrically connected to the integrated conditioning circuit, realized on the other side of the PCB, as shown in Fig. 4.1d. The PCB is milled and cut through a LPKF ProtoMat S63.

The piezoelectric layer is a Polyvinylidene Fluoride (PVDF) thin film from Kureha, with a thickness of 39 µm. The notable piezoelectric voltage coefficients of PVDF are suitable for the voltage sensitivity enhancement strategy described in section 1.4 [90].

The PVDF film is bonded on the PCB with M-Bond 200 adhesive. A small circular copper pad of 1 mm diameter implements the bottom electrode. The top electrode is realized with a copper tape strip, having approximately the same width as the bottom pad diameter. The copper tape is soldered on one side onto a square copper pad, providing an electrical connection for the voltage buffer which implements the conditioning circuitry.

Conditioning circuitry

The buffer is realized with a low-noise operational amplifier model LT1793, as shown in Fig. 4.4. The operational amplifier is characterized by an input resistance and capacitance of 100 TΩ and 1.5 pF, respectively. A resistance R_{dc} of 1 GΩ provides a DC path to ground. The measured sensor capacitance is 12 pF, resulting in a lower cutoff frequency below 20 Hz.

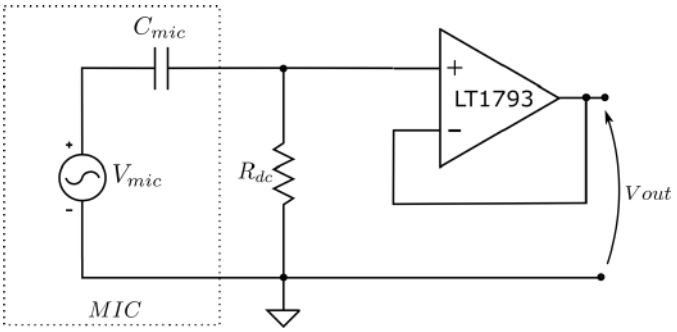

FIGURE 4.4: Simplified schematic of microphone conditioning circuitry.

Preload and assembly

A metallic bottom enclosure with a circular boss of 250 µm at the center enables the preload mechanism, by pushing upward the moving part during the assembly of the device 4.1e. The estimated preload stress on PVDF is 0.32 MPa, significantly lower than the yield stress of 30 MPa [91]. The preload establishes a static operating point well below the non-linear region, thereby avoiding alterations of the dynamic behaviour.

4.2 Acoustic characterization

4.2.1 Measurement setup

Figure 4.5 depicts the experimental setup used for the characterization of the free-field microphone sensitivity.The characterization is performed by comparison with a working standard microphone, according to the standard IEC 610948 [92]. A Zoom UAC-8 sound card is used to manage the input and output signals (I/O interface). The sound card is controlled by the ITAToolbox [93] in MATLAB. The signal driving the loudspeaker is amplified by a Crown 1202 power amplifier. The reference pressure signal at

the sample location is measured with a Brüel&Kjær 2250 phonometer, equipped with a calibrated Brüel&Kjær 4189 microphone. The voltage signals produced by both the Brüel&Kjær microphone and the 3D-printed microphone are simultaneously acquired by the sound card.

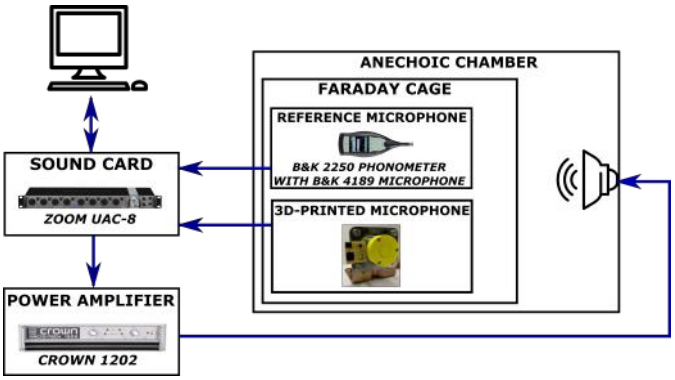

FIGURE 4.5: Acoustic characterization setup. A Zoom UAC-8 sound card is used as input/output (I/O) interface. The loudspeaker signal is amplified through a Crown 1202 amplifier. Voltage signals from both the reference and the 3D-printed microphones are simultaneously acquired.

Both the microphones are arranged inside an anechoic chamber ($1.4 \times 1.5 \times 1.7\,\mathrm{m}^3$), on-axis with the loudspeaker and at 1-meter distance, to ensure far-field conditions. A grounded Faraday cage minimizes critical electromagnetic interferences.

4.2.2 Sensitivity frequency response

The sensitivity of the microphone as a function of frequency has been analyzed with both experimental measurements and multiphysics simulations. The Exponential Sine Sweep (ESS) technique [94] is adopted for the characterization of the microphone sensitivity frequency response. An ESS voltage spanning from 300 Hz to 10000 Hz in 20 seconds is applied to the loudspeaker. The measurement range is limited downwards by the effectiveness of the anechoic chamber and upwards by the loudspeaker frequency response. The instantaneous voltage is acquired from both the microphones and the frequency response of the 3D-printed microphone is finally computed according to the ESS technique.

Sensitivity comparison

Figure 4.6 shows a comparison of the sensitivity measured for the three prototypes, having vent width equal to 500 µm, 250 µm and 100 µm, respectively. The results of simulations performed with the circuit model described in chapter 3 are added for comparison. The circuit model components values, used for simulations, are determined by setting the underlying geometrical parameters consistent with the fabricated samples. The fabricated samples geometrical dimensions are reported in Fig. 4.1a. Notice that, besides the variable vent width, all the dimensions are consistent with the reference configuration of Fig. 3.20b, adopted for circuit model validation.

Overall good agreement is observed between measurements and simulations. A reduction of the vent width causes an improvement of the sensitivity in the low-frequency

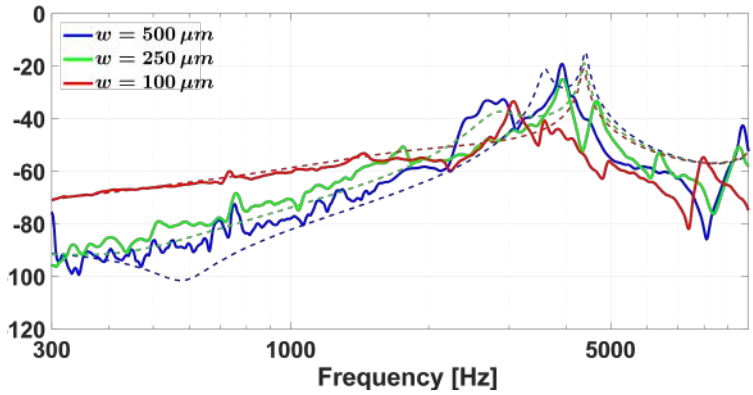

FIGURE 4.6: Experimental measurements (solid line) and circuit model simulation (dashed line) of the microphones sensitivity frequency response, in the range 300 Hz - 10 KHz.

region, as expected. The prototype trimmed by laser cutting shows the best performance among the analyzed samples.

A slight mismatch of the resonance frequency can however be observed between measurements and circuit simulations. The close agreement between the circuit model and FEM simulations, performed in the validation section 3.4.2 of chapter 3, suggests that the discrepancy is attributable to phenomena not accounted within the model itself. Indeed, the model considers a rather idealized structure, necessary to limit the complexity in favor of manageability. Hence, the causes of the mismatch should be investigated in the non-idealities of the fabricated device.

In the following, the frequency response of the best performing laser-cut microphone is analyzed in more detail, together with an inspection of the causes for the resonance shift.

Sensitivity of laser-cut microphone

The measured frequency response of the laser-cut microphone is reported in Fig. 4.7 together with FEM simulations. The sensitivity is equal to 1 mV/Pa ($\pm$ 6 dB) in the bandwidth 500 $-$2500 Hz (-60$\pm$ 6 dB rel. 1 V/Pa). A 20 dB/decade slope is observed at low frequency, most likely due to the high-pass filtering effect of the circular vent, a phenomenon observed during the analysis of chapter 3. A mechanical resonance is also observed at about 3.1 kHz, with a resonance damping ratio of $\zeta = 0.0193$, estimated according to the half-power method [77].

A complete 3D model of the microphone has been developed with COMSOL Multiphysics 5.3a to better investigate the resonance shift behavior. The model includes the mechanical, acoustical, and electrical domains, as described in section 3.4.2. The required mechanical and electrical material parameters are taken from the manufacturer's datasheet [95] and literature [96], [97].

A harmonic pressure load of 1 Pa amplitude is applied to both the top plate and the vent to emulate the acoustic stimulus. Fig. 4.7 shows the simulation results of the open-circuit sensitivity frequency response, considering both the ideal (perfectly on axis) and a tilted configuration (0.2° axial tilt) of the moving part. The simulations

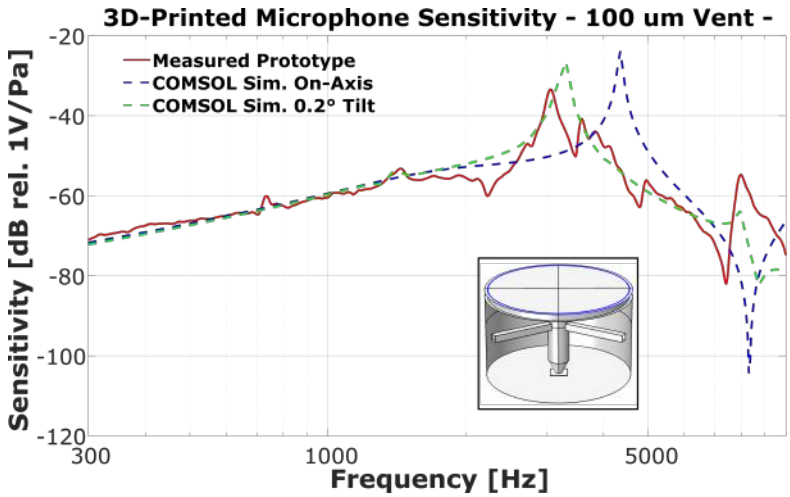

FIGURE 4.7: COMSOL simulations and measurement of the laser-cut microphone sensitivity frequency response, in the frequency range 300 Hz - 10 KHz. The inset shows the COMSOL geometry (one side hidden).

reveal a sensitivity of 1 V/Pa (± 6 dB) in the bandwidth 500 −2000 Hz and an approximate 20 dB/decade slope at lower frequencies, in accordance with experimental results.

The on-axis configuration shows a damped resonance at 4.34 kHz, as confirmed by a further eigenfrequency analysis. Such eigenfrequency is characterized by a symmetrical bending of the top plate periphery with respect to the center, due to its limited flexural rigidity. The resonance is also in agreement with circuit simulations.

Interestingly, the resonance frequency is overestimated. The lower resonance frequency shown in the experimental results is compatible with a 0.2° axial tilt of the moving part, shifting the resonance to 3.27 kHz. The rotation causes a reduction of the contact area between the tip and the PVDF film, which decreases their equivalent dynamic stiffness (k, see section 3.2.2). According to the model, the spring constant associated to the pillar tip, in particular, plays a major role in determining the overall stiffness of the structure. Hence, a significant variation results in a shift of the system resonance. If the system is approximated with a SDOF model, the resonance frequency is given by:

$$f_{res} = \frac{1}{2\pi}\sqrt{\frac{k}{m}} \tag{4.1}$$

highlighting that a reduction of the equivalent stiffness implies a shift of the resonance downwards, assuming that the moving mass is not altered. Although the actual system vibration is more complex than the simple SDOF, as analyzed in chapter 3, the qualitative assessment remains valid.

The contact area reduction is not accompanied by an equivalent electrode patterning, so no significant sensitivity variation is expected. While the piezoelectric film is stressed on a smaller area, the total generated charge remains unaltered, being related to the total force acting on the plate, according to Eq. 1.12. Since the electrical capacitance is also unaffected, the expected open circuit voltage is the same as that of the on-axis configuration (see Eq. 1.14).

Geometrical imperfection of the 3D-printed ABS part can easily bring to the tilted condition during preload, particularly if they involve the pillar tip or the flexural spring.

For instance, unequal spring beams would exert different forces on the moving part during preload, causing a small rotation as a result.

Overall, good agreement is observed between simulations and measurements, suggesting that the relevant physical mechanisms have been captured.

4.2.3 Linearity of laser-cut microphone

Linearity represents a desirable characteristic of most sensors, including microphones [98]. Linearity is determined by measuring the sensitivity of the microphone at increasing sound pressure levels. The pressure range is selected to guarantee a reliable overall measurement. Such range is limited downwards by the electronic noise of the microphone and upwards by the loudspeaker harmonic distortion.

Figure 4.8 shows the measured linearity data, together with the linear regression line. The plot shows that the 3D-printed microphone is characterized by an almost perfect linear response within the measurable range.

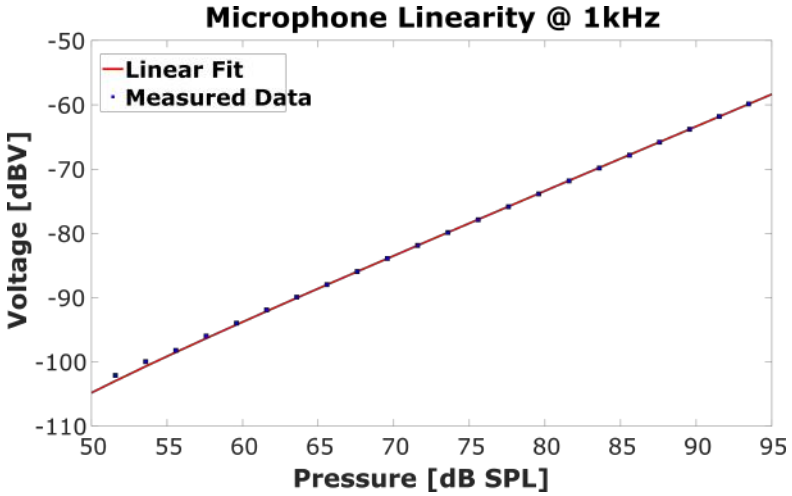

FIGURE 4.8: Measured linearity of the fabricated laser-cut microphone at 1 kHz.

4.3 Discussion

The laser-cut sample shows an open-circuit voltage sensitivity of 1 mV/Pa ($\pm$ 6 dB) in the bandwidth 500 $-$2000 Hz, about 36 times (31.1 dB) greater than the sensitivity of the microphone in [45], which exploits the same design principles. The sensitivity improvement is guaranteed by the increased area ratio between the top plate and the pillar, and is greater than the active area scaling (see Table 4.1). In this regard, 3D-printing and laser-cutting technologies allowed pushing the design parameters while maintaining limited fabrication complexity.The device sensitivity is comparable to other existing microphones (see Table 4.1). In addition, 3D-printing guarantees low cost and reduced realization complexity, high production speed and considerable design flexibility.

The measured mechanical resonance of about 3.1 kHz and the decaying sensitivity at low frequencies limit the operating bandwidth, and thus the potential applications of the fabricated sensor (e.g. voice or active noise control). The bandwidth is mainly

limited by mechanical factors. The upper limit is set by the fundamental resonance of the system, caused by the low top plate flexural rigidity and the low stiffness of the pillar tip, accentuated by potential fabrication defects. The plate stiffness can be increased by acting on the geometry (e.g. thickness or shape) and material (e.g. Kevlar). The tip contact problem can be addressed through higher printing resolutions and a better spring design (e.g., planar). The pressure equalization phenomena affect lower frequencies and can be tackled through smaller gaps, which requires a more precise system assembly due to the reduced tolerances.

The described drawbacks are however related to the implemented design, whose main purpose is to investigate the potential of the fabrication technique while focusing the device sensitivity. A multiobjective modeling and optimization is likely to improve the results, particularly in terms of frequency response. The observed results indicate that the realization of 3D-printed microphones is feasible, and may lead to the realization of custom designs. These aspects become particularly significant when compared to other fabrication technologies, such as MEMS, in which device customization implies a significant increase of the production cost.

Type	Reference	Technology	Sensitivity (mV/Pa)	A.A. (μm^2) [a]	Bandwidth (Hz) [b]
S	Proposed	Piezoelectric Pillars - PVDF	1	314	500-2500
S	[45]	Piezoelectric Pillars - PVDF	0.0278	56.7	10-20000
S	[10]	Piezoelectric MEMS - PZT	0.001166	10.5	10-6700
S	[99]	Piezoelectric MEMS - ZnO	1	4	200-5000
C	Dytran2013d	Piezoelectric Ceramic	0.290	≈ 191	0.3-5000
C	ShureSM58	Dynamic	1.85	≈ 507	50-15000

[a] The active area (A. A.) is defined as the sensor area exposed to the acoustic pressure, which affects the sensitivity (e.g., top plate).

[b] The bandwidth is the measured frequency range where the sensitivity is $\pm$ 6 dB with respect to 1 KHz

TABLE 4.1: Comparison of Microphones from Scientific Literature [S] and Commercial [C].

Chapter 5

Conclusions

The evolution of printing techniques, together with the synthesis of novel piezoelectric materials, enable the rapid and flexible development of low-cost piezoelectric sensors. The adoption of printing technology for piezoelectric microphones fabrication represents a novelty, with little (or nonexistent) prior art. Nevertheless, their combination presents unique advantages. The rapid prototyping enabled by printing techniques streamlines the development chain and facilitates the effective exploration of custom designs. In addition, the fabrication process is made cheaper and faster. By virtue of these considerations, it may represent a complementary solution with respect to the dominant MEMS fabrication technology, characterized by a rigid development scheme, which requires high production volumes for cost mitigation. At the same time, device customizations translate in significant costs and are discouraged.

This thesis contributes to distinct topics of printed piezoelectric microphones, concerning in particular the fabrication, modeling and engineering of these devices. The obtained results constitute a baseline useful for further development.

The proposed single-pillar microphone design represents one of the first attempts to combine piezoelectric microphone technology and 3D-printing fabrication. The pillar-based approach allows for a design compatible with 3D-printing, while maintaining a competitive microphone voltage sensitivity. The overall device fabrication is simplified by 3D-printing most of the mechanical structure as a single element. As a result, a piezoelectric microphone can be fabricated through a fast, efficient and cost-effective process. This aspect provides an edge over alternative fabrication methods, which require either high-cost equipment (i.e. MEMS) or convoluted manufacturing procedures.

The microphone design is characterized by an annular aperture (i.e. vent) which ensures the correct system mobility and avoids detrimental force dissipations. An original, comprehensive study is performed to analyze the acoustic propagation in annular waveguides, including thermoviscous effects. A simple lumped-element circuit model is derived as a result, useful to accelerate both the analysis and engineering of devices having elements with annular cross-section, including the proposed microphone design. To this regard, acoustic losses in the vent are functional to avoid dynamic pressure equalization phenomena.

An original multiphysics circuit model of the 3D-printed piezoelectric microphone is proposed. The model couples together the involved acoustic, mechanical, and electrical domains by means of equivalent electrical analogies. The model allows for a deeper physical understanding of the single device elements and their effect on the overall

system behavior. Hence, it represents a useful tool for a further development and engineering of the printed piezoelectric microphone technology. The proposed model recognized the vent gap, the top plate thickness and the pillar tip radius as critical parameters for the performance of the device, particularly in terms of sensitivity and bandwidth.

Finally, 3D-printed microphones have been fabricated and characterized. The prototype trimmed by laser cutting, in particular, is denoted by appreciable bandwidth and sensitivity and is among the first working examples of 3D-printed piezoelectric microphones.

However, there is still significant room for improvement. The microphone bandwidth can be increased by exploiting the latest advancements of 3D-printing technology. The targeted deposition of light, rigid materials on the critical elements (e.g. plate) allows for a shift of the device resonance upwards. Some recent printers, like the Markforged X7 [100], are indeed able to selectively add a reinforcement fiber, like Kevlar or Carbon, within a base plastic material, such as Onyx or Nylon. As a result, the printed microphone would be characterized by targeted elements of increased rigidity, according to the functional needs. As already discussed, the top plate and the pillar tip are perfect candidates for reinforcement. A light and stiff material would provide an augmented elastic stiffness (k) without altering the overall mass, hence effectively increasing the fundamental frequency of the system and thus the bandwidth.

Simultaneously, a reduction of the 3D-printer clearance specification would allow the fabrication of smaller vents, resulting in the extension of the bandwidth at lower frequencies. At the current state, this solution seems to be more challenging than the previously described reinforcement strategy. To the author knowledge, no printer is currently able to effectively produce a clearance of approximately 20 µm, required to reach the lower limit of the audio bandwidth of 20 Hz. This thesis work demonstrated that the adoption of an average FDM 3D-printer for microphone fabrication requires a laser trimming step, in order to obtain acceptable results. Improvements could be attained by adopting more advanced 3D-printers and, in particular, printing techniques with higher resolutions and lower clearance specifications, such as laser sintering (SLS). The improvement may enable, in particular, the fabrication of working microphones without the need for a laser trimming procedure.

Appendix A

LRF propagation model in annular waveguides

The basic equations governing thermoviscous acoustic wave propagation are the Navier-Stokes equation, the continuity equation, the energy equation, and the equation of state for an ideal gas [70]. The governing equations can be linearized and expressed in the frequency domain as:

$$i\omega\rho_0\tilde{\mathbf{v}} = -\nabla\tilde{P} + (\mu' + \mu)\nabla(\nabla\cdot\tilde{\mathbf{v}} + \mu\Delta\tilde{\mathbf{v}}) \tag{A.1}$$

$$i\omega\tilde{\rho} + \rho_0\nabla\cdot\tilde{\mathbf{v}} = 0 \tag{A.2}$$

$$i\omega\rho_0 C_P\tilde{T} = i\omega\tilde{P} + \kappa\Delta\tilde{T} \tag{A.3}$$

$$\frac{\tilde{P}}{P_0} = \frac{\tilde{\rho}}{\rho_0} + \frac{\tilde{T}}{T_0} \tag{A.4}$$

The different terms are described in Table 1. Equations A.1 to A.4 are valid if 1) the total density, temperature, and pressure are characterized by small harmonic perturbations around their mean value and 2) no mean flow is present (no steady component of velocity $\mathbf{v}$:

$$\rho = \rho_0 + \tilde{\rho}e^{i\omega t}, \qquad \tilde{\rho} \ll \rho_0 \tag{A.5}$$

$$T = T_0 + \tilde{T}e^{i\omega t}, \qquad \tilde{T} \ll T_0 \tag{A.6}$$

$$P = P_0 + \tilde{P}e^{i\omega t}, \qquad \tilde{P} \ll P_0 \tag{A.7}$$

$$i\mathbf{v} = \tilde{\mathbf{v}}e^{i\omega t} \tag{A.8}$$

The low-reduced-frequency (LRF) model allows simplifying the governing equations, by splitting the operators into their contribution in propagation directions and constrained directions [64]. According to the cylindrical coordinates in Fig. 2.1, x and r represent the propagation and constrained directions, respectively. The governing equations in LRF form become:

$$i\frac{\tilde{v}_x}{c_0} = -\frac{1}{k\gamma P_0}\frac{\partial \tilde{P}}{\partial x} + \frac{1}{s^2 c_0}\left[\frac{\partial^2 \tilde{v}_x}{\partial r^2} + \frac{1}{r}\frac{\partial \tilde{v}_x}{\partial r}\right] \tag{A.9}$$

$$i\frac{\tilde{\rho}}{\rho_0} = -\frac{1}{kc_0}\left[\frac{\partial \tilde{v}_r}{\partial r} + \frac{\tilde{v}_r}{r} + \frac{\partial \tilde{v}_x}{\partial x}\right] \tag{A.10}$$

$$i\frac{\tilde{T}}{T_0} = i\left[\frac{\gamma-1}{\gamma}\right]\frac{\tilde{P}}{P_0} + \frac{1}{s_t^2 T_0}\left[\frac{\partial^2 T}{\partial r^2} + \frac{1}{r}\frac{\partial T}{\partial r}\right] \tag{A.11}$$

$$\frac{\partial \tilde{P}}{\partial r} = 0 \tag{A.12}$$

$$\frac{\tilde{P}}{P_0} = \frac{\tilde{\rho}}{\rho_0} + \frac{\tilde{T}}{T_0} \tag{A.13}$$

where (see Table A.1):

$$k = \frac{\omega}{c_0} \tag{A.14}$$

$$s = \frac{1}{\delta_V} = \sqrt{\frac{\omega\rho_0}{\mu}} \tag{A.15}$$

$$s_t = s\sqrt{Pr} \tag{A.16}$$

$$\xi = \frac{\mu'}{\mu} \tag{A.17}$$

$$\gamma = \frac{C_P}{C_V} \tag{A.18}$$

Both Eq. A.9 and A.11 can be solved according to the methodology outlined in [64] for the cylindrical tube, resulting in the solutions:

$$\tilde{v}_x = -\frac{i}{\omega\rho_0}\frac{\partial \tilde{P}}{\partial x}A(s,r) \tag{A.19}$$

$$\tilde{T} = \frac{T_0}{P_0}\left[\frac{1-\gamma}{\gamma}\right]\tilde{P}A(s_t,r) \tag{A.20}$$

in which the function $A(z,r)$ is defined as:

$$A(z,r) = -A_1(z)J_0(i\sqrt{i}zr) - A_2(z)Y_0(i\sqrt{i}zr) - 1 \tag{A.21}$$

$$A_1(z) = \frac{Y_0(i\sqrt{i}zr_i) - Y_0(i\sqrt{i}zr_o)}{Y_0(i\sqrt{i}zr_o)J_0(i\sqrt{i}zr_i) - Y_0(i\sqrt{i}zr_i)J_0(i\sqrt{i}zr_o)} \tag{A.22}$$

$$A_2(z) = \frac{J_0(i\sqrt{i}zr_o) - J_0(i\sqrt{i}zr_i)}{Y_0(i\sqrt{i}zr_o)J_0(i\sqrt{i}zr_i) - Y_0(i\sqrt{i}zr_i)J_0(i\sqrt{i}zr_o)} \tag{A.23}$$

Where J_0 and Y_0 are the Bessel functions of order 0 of the first and second kind, respectively.

The solution is obtained by imposing no-slip and isothermal boundary conditions at the walls:

$$\tilde{v}_x(r_i) = \tilde{v}_x(r_o) = 0 \tag{A.24}$$

$$\tilde{T}(r_i) = \tilde{T}(r_o) = 0 \tag{A.25}$$

Substituting Eq.A.20 in A.13 yields the solution for density:

$$\tilde{\rho} = \frac{\rho_0}{P_0}\tilde{P}\left[1 + \frac{\gamma - 1}{\gamma}A(s_t, r)\right] \tag{A.26}$$

Finally, substitution of the solutions A.19 and A.26 into the continuity equation A.10 and averaging in the radial direction through integration provides the Helmholtz wave equation:

$$\frac{\partial^2 \tilde{P}}{\partial x^2} - k^2\Gamma^2\tilde{P} = 0 \tag{A.27}$$

where:

$$\Gamma = \sqrt{\frac{\gamma + (\gamma - 1)B(s_t)}{B(s)}} \tag{A.28}$$

$$B_A(z) = \frac{2}{r_o^2 - r_i^2}\frac{i}{\sqrt{iz}}[F_1(z) + F_2(z)] - 1 \tag{A.29}$$

$$F_1(z) = A_1(z)[r_o J_1(i\sqrt{iz}r_o) - r_i J_1(i\sqrt{iz}r_i)] \tag{A.30}$$

Symbol	Description	Unit
P	Pressure	[Pa]
v	Particle velocity	[m/s]
ρ	Density	[kg/m^3]
T	Temperature	[K]
μ	Dynamic viscosity	[Pa s]
μ'	Volume viscosity	[Pa s]
C_P	Specific heat at constant pressure	[J/(K kg)]
C_V	Specific heat at constant volume	[J/(K kg)]
κ	Thermal conductivity	[W/(K m)]
k	Wave number	[1/m]
s	Shear wave number	[1/m]
s_t	Thermal wave number	[1/m]
Pr	Prandtl number	-
γ	Adiabatic index	-
ξ	Viscosity ratio	-
δ_V	Viscous boundary layer thickness	[m]

TABLE A.1: Definition of symbols encountered within the analytical expressions

$$F_2(z) = A_2(z)[r_o Y_1(i\sqrt{i}zr_o) - r_i Y_1(i\sqrt{i}zr_i)] \tag{A.31}$$

The term γ accounts for viscous and thermal effects. When $\Re(\Gamma) = 0$ and $\Im(\Gamma) = 1$, wave propagation becomes inviscid and adiabatic (free-air propagation). The B function encapsulates the geometry-related part of the solution. The result appears to be consistent with [101], upon application of analogous boundary conditions.

The validity of the analytical result is restricted by the assumptions of the LRF model [70]. The acoustic wavelength should be large compared to the width w and to the boundary layer thickness δ_V, according to Eqs. A.32 and A.33:

$$\tilde{k} = lk = wk \ll 1 \tag{A.32}$$

$$\frac{k}{s} = k\delta_V \ll 1 \tag{A.33}$$

Appendix B

Two-port network model of an acoustic waveguide with thermoviscous wave propagation

An acoustic waveguide can be modeled as an equivalent electrical transmission line, characterized by the propagation constant q and the characteristic impedance Z_0 [71].

A waveguide section of length L can be further specified as a two-port network, associating to each waveguide end (port) a pressure-velocity pair ($\tilde{P}_i$, $\tilde{v}_i$). The network can be described according to the z-parameters matrix as:

$$\begin{bmatrix} \tilde{P}_1 \\ \tilde{P}_2 \end{bmatrix} = \begin{bmatrix} \frac{Z_0}{\tanh(qL)} & \frac{Z_0}{\sinh(qL)} \\ \frac{Z_0}{\sinh(qL)} & \frac{Z_0}{\tanh(qL)} \end{bmatrix} \cdot \begin{bmatrix} \tilde{v}_1 \\ \tilde{v}_2 \end{bmatrix} \tag{B.1}$$

The waveguide section can also be equivalently modelled as the T-Network of Fig. 2.4b, implementing the description of Eq. B.1. The network is characterized by a series impedance Z_s and a parallel impedance Z_p:

$$Z_s = iZ_0[\cot(iqL) - \csc(iqL)] \tag{B.2}$$

$$Z_p = iZ_0 \csc(iqL) \tag{B.3}$$

The propagation constant q can be derived directly from Eq. A.27, which presents the same form as the wave equation of a lossy electrical transmission line. Hence:

$$q = k\Gamma = k\sqrt{\frac{\gamma + (\gamma - 1)B(s_t)}{B(s)}} \tag{B.4}$$

The characteristic impedance Z_0 is, by definition, the ratio between a single (forward or reflected) pressure wave and the related particle velocity wave along the transmission line. The solution for pressure is obtained from Eq. A.27 as:

$$\tilde{P}(x) = C_1 e^{-qx} + C_2 e^{+qx} \tag{B.5}$$

The particle velocity component in the propagation direction x is [70]:

$$\tilde{v}_x(x, c) = -\frac{i}{\omega \rho_0} \frac{\partial \tilde{P}}{\partial x} A(s, c) \tag{B.6}$$

where c denotes the constrained direction. For the annular waveguide, c corresponds to the radial direction r (Eq. A.19). By averaging the velocity in the constrained direction, we obtain:

$$\bar{v}_x(x) = -\frac{i}{\omega\rho_0}\frac{\partial\tilde{P}}{\partial x}B(s) \tag{B.7}$$

Substituting Eq. B.5 into Eq. B.7 we obtain:

$$\bar{v}_x(x) = \frac{iqB(s)}{\omega\rho_0}(C_1e^{-qx} + C_2e^{+qx}) \tag{B.8}$$

The characteristic impedance Z_0 is thus:

$$Z_0 = \frac{\tilde{P}^+}{\bar{v}_x^+} = -\frac{i\omega\rho_0}{qB(s)} \tag{B.9}$$

Appendix C

Derivation of annular waveguide lumped-element circuit model

The circuit model with linear electrical components is obtained from the T-Network model (Fig. 2.4b) for the waveguide having rectangular layers geometry, through approximation of the impedances Z_s and Z_p of Eqs. B.2 and B.3. The approximation provides simplified analytical expressions of the impedances, which can be directly implemented by the target circuit.

The Laurent series expansion of the cotangent and cosecant functions provides:

$$Z_s = qZ_0\frac{L}{2} \tag{C.1}$$

$$Z_p = Z_{p,1} + Z_{p,2} \tag{C.2}$$

where:

$$Z_{p,1} = \frac{Z_0}{q}\frac{1}{L} \tag{C.3}$$

$$Z_{p,2} = -\frac{1}{3}Z_s \tag{C.4}$$

According to Eqs. B.8 and B.9, the expressions for qZ_0 and $\frac{Z_0}{q}$ are:

$$qZ_0 = -\frac{i\omega\rho_0}{B_Y(s)} \tag{C.5}$$

$$\frac{Z_0}{q} = -\frac{iP_0\gamma}{\omega[\gamma + (\gamma - 1)B_Y(s_t)]} \tag{C.6}$$

where:

$$B_Y(z) = \frac{2\tanh\left(\frac{\sqrt{i}tz}{2}\right)}{\sqrt{i}tz} - 1 \tag{C.7}$$

is the B function of the rectangular layers geometry, with t being the gap thickness. The hyperbolic tangent can effectively be approximated, in the whole domain, by rational functions of a given order (Padé approximants). In particular, the Padé approximants can capture the horizontal asymptotes of the hyperbolic tangent (for both the real and imaginary components).

The order of the Padé approximant is chosen such that Z_s and Z_p of Eqs. C.1 and C.2 can effectively be implemented by an equivalent circuit model with linear passive components. The hyperbolic tangent of the function B_Y in Eq. C.5 is approximated with a Padé rational function of order [5/4], having form:

$$\tanh(x) = \frac{x(1 + a_1 x^2 + a_2 x^4)}{1 + b_1 x^2 + b_2 x^4} \tag{C.8}$$

with $a_1 = 1/9$, $a_2 = 1/945$, $b_1 = 4/9$, and $b_2 = -a_2 = -1/945$. The coefficient b_2 is modified with respect to the regular expansion, in order to impose the correct asymptotic value of B_Y. Substitution of Eqs. C.5, C.7, and C.8 into Eq. C.1 provides:

$$Z_s = \frac{f_1 + i\omega f_2 - \omega^2 f_3}{1 + i\omega f_4} \tag{C.9}$$

where f_1, f_2, f_3, and f_4 are frequency-independent terms. Equation C.9 can be directly implemented with the second-order circuit having equivalent impedance equal to (see Fig. C.1):

$$Z_s = \frac{R_{s,1} + i\omega \left(L_{s,1} + L_{s,2} + \frac{R_{s,1} L_{s,2}}{R_{s,2}} \right) - \omega^2 \frac{L_{s,1} L_{s,2}}{R_{s,2}}}{1 + i\omega \frac{L_{s,2}}{R_{s,2}}} \tag{C.10}$$

where:

$$R_{s,1} = \frac{6\mu L}{t^2} \tag{C.11}$$

$$L_{s,1} = \frac{\rho_0 L}{2} \tag{C.12}$$

$$R_{s,2} = \frac{9\mu L}{t^2} \tag{C.13}$$

$$L_{s,2} = \frac{\rho_0 L}{10} \tag{C.14}$$

The hyperbolic tangent of the function B_Y in Eq. C.6 is approximated with a Padé rational function of order [3/2], having form:

$$\tanh(x) = \frac{x(1 + a_1 x^2)}{1 + b_1 x^2} \tag{C.15}$$

with $a_1 = 1/15$, and $b_1 = -a_1 = -1/15$. The coefficient b_1 is modified with respect to the regular expansion, in order to impose the correct asymptotic value of B_Y. Substitution of Eqs. C.6, C.7, and C.15 into Eq. C.3 provides:

$$Z_{p,1} = \frac{1 + i\omega g_1}{i\omega g_2 - \omega^2 g_3} \tag{C.16}$$

where g_1, g_2, and g_3 are frequency-independent terms. Equation C.16 can be directly implemented with the second-order circuit having equivalent impedance equal to (see Fig. C.1):

$$Z_{p,1} = \frac{1 + i\omega R_{p,3}(C_{p,1} + C_{p,2})}{i\omega C_{p,1} - \omega^2 R_{p,3} C_{p,1} C_{p,2}} \tag{C.17}$$

where:

$$R_{p,3} = \frac{t^2 Pr P_0 \rho_0 (\gamma - 1)}{12\gamma\mu L} \tag{C.18}$$

$$C_{p,1} = \frac{L}{P_0} \tag{C.19}$$

$$C_{p,2} = \frac{L}{P_0(\gamma - 1)} \tag{C.20}$$

Finally, Eq. C.4 is implemented by a linear circuit with equivalent impedance described by Eq. C.10, where (see Fig. C.1):

$$R_{p,1} = -\frac{2\mu L}{t^2} \tag{C.21}$$

$$L_{p,1} = -\frac{\rho_0 L}{6} \tag{C.22}$$

$$R_{p,2} = -\frac{3\mu L}{t^2} \tag{C.23}$$

$$L_{p,2} = -\frac{\rho_0 L}{30} \tag{C.24}$$

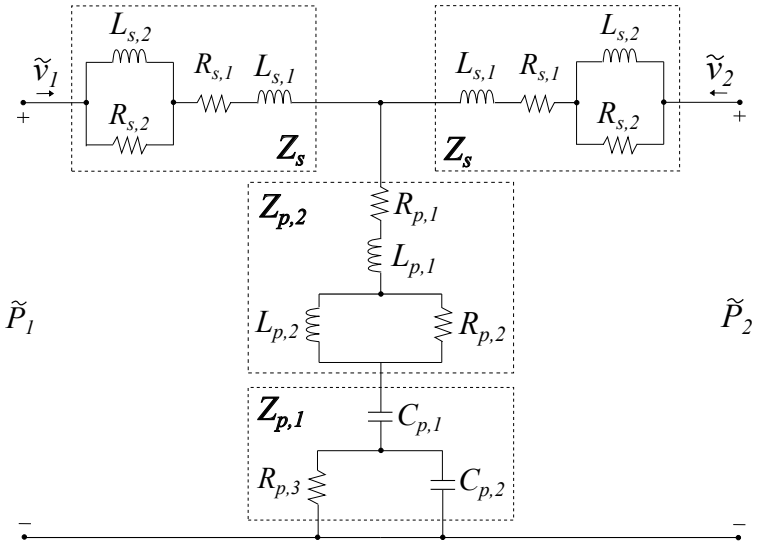

FIGURE C.1: Simplified circuit model of a waveguide section of length L having rectangular layers geometry. The T-network impedances Z_s and Z_p are approximated as networks of linear electrical components, according to Eqs. C.1 and C.2

Bibliography

[1] D. T. Martin, J. Liu, K. Kadirvel, R. M. Fox, M. Sheplak, and T. Nishida, "A micromachined dual-backplate capacitive microphone for aeroacoustic measurements," *Journal of Microelectromechanical Systems*, vol. 16, no. 6, pp. 1289–1302, 2007, ISSN: 10577157. DOI: 10.1109/JMEMS.2007.909234.

[2] A. L. Williams, "Piezoelectric Microphones," *Journal of the Society of Motion Picture Engineers*, vol. 23, no. 4, pp. 196–209, Oct. 1934, ISSN: 0097-5834. DOI: 10.5594/J05439.

[3] J. Medill, "A miniature piezoelectric microphone," *Transactions of the IRE Professional Group on Audio*, vol. AU-1, no. 6, pp. 7–10, Nov. 1953, ISSN: 2168-2968. DOI: 10.1109/T-SP.1953.28160.

[4] E. Fukada and T. Sakurai, *Piezoelectricity in Polarized Poly(vinylidene fluoride) Films*, 1970. DOI: 10.1295/polymj.2.656.

[5] G. M. Sessler, "Piezoelectricity in polyvinylidenefluoride," *The Journal of the Acoustical Society of America*, vol. 70, no. 6, pp. 1596–1608, Dec. 1981, ISSN: 0001-4966. DOI: 10.1121/1.387225.

[6] R. Lerch, "Electroacoustic transducers using piezoelectric polyvinylidenefluoride films," *The Journal of the Acoustical Society of America*, vol. 66, no. 4, pp. 952–954, Oct. 1979, ISSN: 0001-4966. DOI: 10.1121/1.383416. [Online]. Available: http://asa.scitation.org/doi/10.1121/1.383416.

[7] R. Lerch and G. M. Sessler, "Microphones with rigidly supported piezopolymer membranes," *The Journal of the Acoustical Society of America*, vol. 67, no. 4, pp. 1379–1381, Apr. 1980, ISSN: 0001-4966. DOI: 10.1121/1.384136.

[8] M. Toda, "Theory of curved, clamped, piezoelectric film, air-borne transducers," *IEEE Transactions on Ultrasonics, Ferroelectrics, and Frequency Control*, vol. 47, no. 6, pp. 1421–1431, 2000, ISSN: 08853010. DOI: 10.1109/58.883531.

[9] M. Royer, J. O. Holmen, M. A. Wurm, O. S. Aadland, and M. Glenn, "ZnO on Si integrated acoustic sensor," *Sensors and Actuators*, vol. 4, no. C, pp. 357–362, 1983, ISSN: 02506874. DOI: 10.1016/0250-6874(83)85044-6.

[10] S. Horowitz, T. Nishida, L. Cattafesta, and M. Sheplak, "A micromachined piezoelectric microphone for aeroacoustics applications," *Technical Digest - Solid-State Sensors, Actuators, and Microsystems Workshop*, no. January, pp. 31–36, 2006. DOI: 10.1121/1.2785040.

[11] M. D. Williams, B. A. Griffin, T. N. Reagan, J. R. Underbrink, and M. Sheplak, "An AlN MEMS piezoelectric microphone for aeroacoustic applications," *Journal of Microelectromechanical Systems*, vol. 21, no. 2, pp. 270–283, 2012, ISSN: 10577157. DOI: 10.1109/JMEMS.2011.2176921.

[12] J. Li, C. Wang, W. Ren, and J. Ma, "ZnO thin film piezoelectric micromachined microphone with symmetric composite vibrating diaphragm," *Smart Materials and Structures*, vol. 26, no. 5, 2017, ISSN: 1361665X. DOI: 10.1088/1361-665X/aa6ae9.

[13] Vesper Technologies Inc., *Vm1000 Low-noise Bottom Port Microphone Data Sheet*, 2017.

[14] A. Wolter, A. Herrmann, G. Yildiz, H. Schenk, and H. Lakner, "Designing MEMS for manufacturing," *Optomechatronic Micro/Nano Components, Devices, and Systems*, vol. 5604, no. October, p. 74, 2004, ISSN: 0277786X. DOI: 10.1117/12.580902.

[15] T. A. Campbell and O. S. Ivanova, "Additive Manufacturing As a Disruptive Technology: Implications of Three-Dimensional Printing," *Technology & Innovation*, vol. 15, no. 1, pp. 67–79, 2013, ISSN: 19498241. DOI: 10.3727/194982413x13608676060655.

[16] M. Saari, B. Xia, B. Cox, P. S. Krueger, A. L. Cohen, and E. Richer, "Fabrication and Analysis of a Composite 3D Printed Capacitive Force Sensor," *3D Printing and Additive Manufacturing*, vol. 3, no. 3, pp. 137–141, 2016, ISSN: 23297670. DOI: 10.1089/3dp.2016.0021.

[17] E. Suaste-Gómez, G. Rodríguez-Roldán, H. Reyes-Cruz, and O. Terán-Jiménez, "Developing an ear prosthesis fabricated in polyvinylidene fluoride by a 3D printer with sensory intrinsic properties of pressure and temperature," *Sensors (Switzerland)*, vol. 16, no. 3, pp. 1–11, 2016, ISSN: 14248220. DOI: 10.3390/s16030332.

[18] S. Y. Wu, C. Yang, W. Hsu, and L. Lin, "RF wireless lc tank sensors fabricated by 3D additive manufacturing," *2015 Transducers - 2015 18th International Conference on Solid-State Sensors, Actuators and Microsystems, TRANSDUCERS 2015*, pp. 2208–2211, 2015. DOI: 10.1109/TRANSDUCERS.2015.7181399.

[19] I. Nassar, H. Tsang, and T. Weller, "3D printed wideband harmonic transceiver for embedded passive wireless monitoring," *Electronics Letters*, vol. 50, no. 22, pp. 1609–1611, 2014, ISSN: 00135194. DOI: 10.1049/el.2014.0769.

[20] R. I. Haque, E. Ogam, C. Loussert, P. Benaben, and X. Boddaert, "Fabrication of capacitive acoustic resonators combining 3D printing and 2D inkjet printing techniques," *Sensors (Switzerland)*, vol. 15, no. 10, pp. 26 018–26 038, 2015, ISSN: 14248220. DOI: 10.3390/s151026018.

[21] A. Leblanc and A. Lavie, "Three-dimensional-printed membrane-type acoustic metamaterial for low frequency sound attenuation," *The Journal of the Acoustical Society of America*, vol. 141, no. 6, EL538–EL542, 2017, ISSN: 0001-4966. DOI: 10.1121/1.4984623.

[22] D. I. Woodward, C. P. Purssell, D. R. Billson, D. A. Hutchins, and S. J. Leigh, "Additively-manufactured piezoelectric devices," *Physica Status Solidi (A) Applications and Materials Science*, vol. 212, no. 10, pp. 2107–2113, 2015, ISSN: 18626319. DOI: 10.1002/pssa.201532272.

[23] B. Tiller, A. Reid, B. Zhu, J. Guerreiro, R. Domingo-Roca, J. Curt Jackson, and J. F. Windmill, "Piezoelectric microphone via a digital light processing 3D printing process," *Materials and Design*, vol. 165, p. 107 593, 2019, ISSN: 18734197. DOI: 10.1016/j.matdes.2019.107593.

[24] J. Xu, M. J. Dapino, D. Gallego-Perez, and D. Hansford, "Microphone based on Polyvinylidene Fluoride (PVDF) micro-pillars and patterned electrodes," *Sensors and Actuators, A: Physical*, vol. 153, no. 1, pp. 24–32, 2009, ISSN: 09244247. DOI: 10.1016/j.sna.2009.04.008. arXiv: arXiv:1011.1669v3.

[25] A. Sorrentino, Y. Ricci, D. Castagnetti, and L. Larcher, "Design, prototyping and validation of a new PVDF acoustic sensor," in *Proceedings of 30th International Conference on Adaptive Structures and Technologies, ICAST 2019*, 2019, pp. 71–72.

[26] Y. Ricci, P. La Torraca, and L. Larcher, "Circuit model for thermoviscous propagation in annular waveguides," *SUBMITTED TO: Journal of the Acoustical Society of America (Status: Accept subject to minor revisions)*, 2021.

[27] Y. Ricci, A. Sorrentino, P. La Torraca, L. Cattani, M. Cotogno, G. Cantarella, L. Orazi, D. Castagnetti, P. Lugli, and L. Larcher, "Design and Fabrication of a Pillar-Based Piezoelectric Microphone Exploiting 3D-Printing Technology," *IEEE Sensors Letters*, vol. 5, no. 2, pp. 1–4, Feb. 2021, ISSN: 2475-1472. DOI: 10.1109/LSENS.2021.3053209.

[28] R. S. Dahiya and M. Valle, *Robotic Tactile Sensing*, 1. Dordrecht: Springer Netherlands, 2013, vol. 11, ISBN: 978-94-007-0578-4. DOI: 10.1007/978-94-007-0579-1.

[29] B. Jaffe, W. R. Cook, and H. Jaffe, *Piezoeletric ceramics*. 1971, vol. 3, p. 317, ISBN: 0123795508. DOI: 77-153538.

[30] A. H. Meitzler, H. F. Tiersten, A. W. Warner, D. Berlincourt, G. A. Coquin, and F. S. Welsh, "An American National Standard: IEEE Standard on Piezoelectricity," 1987.

[31] B. Gusarov, E. Gusarova, B. Viala, L. Gimeno, and O. Cugat, "PVDF piezoelectric voltage coefficient in situ measurements as a function of applied stress," *Journal of Applied Polymer Science*, vol. 133, no. 14, Apr. 2016, ISSN: 00218995. DOI: 10.1002/app.43248. [Online]. Available: http://doi.wiley.com/10.1002/app.43248.

[32] Hong-Jin Zhao, Tian-Ling Ren, Jian-She Liu, Li-Tian Liu, and Zhi-Jian Li, "Fabrication of high-quality PZT-based piezoelectric microphone," in *TRANSDUCERS '03. 12th International Conference on Solid-State Sensors, Actuators and Microsystems. Digest of Technical Papers (Cat. No.03TH8664)*, vol. 1, IEEE, 2003, pp. 234–237, ISBN: 0-7803-7731-1. DOI: 10.1109/SENSOR.2003.1215296.

[33] R. G. Polcawich, "A Piezoelectric MEMS Microphone Based on Lead Zirconate Titanate (PZT) Thin Films," US Dept of the Army, Tech. Rep. ARL-TR-3387, Nov. 2004. DOI: 10.21236/ADA429041. [Online]. Available: http://www.dtic.mil/docs/citations/ADA429041.

[34] R. Ried, Eun Sok Kim, D. Hong, and R. Muller, "Piezoelectric microphone with on-chip CMOS circuits," *Journal of Microelectromechanical Systems*, vol. 2, no. 3, pp. 111–120, 1993, ISSN: 10577157. DOI: 10.1109/84.260255. [Online]. Available: http://ieeexplore.ieee.org/document/260255/.

[35] M. Prasad, V. Sahula, and V. K. Khanna, "Design and Fabrication of Si-Diaphragm, ZnO Piezoelectric Film-Based MEMS Acoustic Sensor Using SOI Wafers," *IEEE Transactions on Semiconductor Manufacturing*, vol. 26, no. 2, pp. 233–241, May 2013, ISSN: 0894-6507. DOI: 10.1109/TSM.2013.2238956.

[36] W. S. Lee and S. S. Lee, "Piezoelectric microphone built on circular diaphragm," *Sensors and Actuators, A: Physical*, vol. 144, no. 2, pp. 367–373, 2008, ISSN: 09244247. DOI: 10.1016/j.sna.2008.02.001.

[37] R. S. Fazzio, T. Lamers, O. Buccafusca, A. Goel, and W. Dauksher, "Design and Performance of Aluminum Nitride Piezoelectric Microphones," in *TRANSDUCERS 2007 - 2007 International Solid-State Sensors, Actuators and Microsystems Conference*, vol. 3, IEEE, 2007, pp. 1255–1258, ISBN: 1-4244-0841-5. DOI: 10.1109/SENSOR.2007.4300365. [Online]. Available: http://ieeexplore.ieee.org/document/4300365/.

[38] J. Segovia-Fernandez, S. Sonmezoglu, S. T. Block, Y. Kusano, J. M. Tsai, R. Amirtharajah, and D. A. Horsley, "Monolithic piezoelectric Aluminum Nitride MEMS-CMOS microphone," *TRANSDUCERS 2017 - 19th International Conference on Solid-State Sensors, Actuators and Microsystems*, pp. 414–417, 2017. DOI: 10.1109/TRANSDUCERS.2017.7994075.

[39] B. İlik, A. Koyuncuoğlu, H. Uluşan, S. Chamanian, D. Işık, Ö. Şardan-Sukas, and H. Külah, "Thin Film PZT Acoustic Sensor for Fully Implantable Cochlear Implants," *Proceedings*, vol. 1, no. 4, p. 366, Aug. 2017. DOI: 10.3390/proceedings1040366. [Online]. Available: http://www.mdpi.com/2504-3900/1/4/366.

[40] P. K. Panda and B. Sahoo, "PZT to lead free piezo ceramics: A review," *Ferroelectrics*, vol. 474, no. 1, pp. 128–143, 2015, ISSN: 15635112. DOI: 10.1080/00150193.2015.997146.

[41] Y. Hu, W. Kang, Y. Fang, L. Xie, L. Qiu, and T. Jin, "Piezoelectric poly(vinylidene fluoride) (PVDF) polymer-based sensor for wrist motion signal detection," *Applied Sciences (Switzerland)*, vol. 8, no. 5, 2018, ISSN: 20763417. DOI: 10.3390/app8050836.

[42] L. Ruan, X. Yao, Y. Chang, L. Zhou, G. Qin, and X. Zhang, "Properties and applications of the β phase poly(vinylidene fluoride)," *Polymers*, vol. 10, no. 3, pp. 1–27, 2018, ISSN: 20734360. DOI: 10.3390/polym10030228.

[43] P. Ueberschlag, "PVDF piezoelectric polymer," *Sensor Review*, vol. 21, no. 2, pp. 118–125, 2001, ISSN: 02602288. DOI: 10.1108/02602280110388315.

[44] J. Xu, M. J. Dapino, D. Gallego-Perez, and D. Hansford, "Validation and Characterization of an Acoustic Sensor Based on PVDF Micropillars and Patterned Electrodes," in *ASME 2010 Conference on Smart Materials, Adaptive Structures and Intelligent Systems, Volume 2*, ASMEDC, Jan. 2010, pp. 451–459, ISBN: 978-0-7918-4416-8. DOI: 10.1115/SMASIS2010-3843.

[45] J. Xu, L. M. Headings, and M. J. Dapino, "High Sensitivity Polyvinylidene Fluoride Microphone Based on Area Ratio Amplification and Minimal Capacitance," *IEEE Sensors Journal*, vol. 15, no. 5, pp. 2839–2847, 2015, ISSN: 1530437X. DOI: 10.1109/JSEN.2014.2379636.

[46] K. S. Ramadan, D. Sameoto, and S. Evoy, "A review of piezoelectric polymers as functional materials for electromechanical transducers," *Smart Materials and Structures*, vol. 23, no. 3, 2014, ISSN: 09641726. DOI: 10.1088/0964-1726/23/3/033001.

[47] Bruel&Kjaer, "Microphone Handbook," vol. 1, p. 155, 2019. DOI: 10.1201/b18817-5.

[48] Seung S. Lee, R. Ried, and R. White, "Piezoelectric cantilever microphone and microspeaker," *Journal of Microelectromechanical Systems*, vol. 5, no. 4, pp. 238–242, 1996, ISSN: 10577157. DOI: 10.1109/84.546403.

[49] S. S. Lee and R. M. White, "Piezoelectric cantilever acoustic transducer," *Journal of Micromechanics and Microengineering*, vol. 8, no. 3, pp. 230–238, Sep. 1998, ISSN: 0960-1317. DOI: 10.1088/0960-1317/8/3/009.

[50] R. Littrell and K. Grosh, "Modeling and characterization of cantilever-based MEMS piezoelectric sensors and actuators," *Journal of Microelectromechanical Systems*, vol. 21, no. 2, pp. 406–413, 2012, ISSN: 10577157. DOI: 10.1109/JMEMS.2011.2174419.

[51] S. Timoshenko and S. Woinowsky-Krieger, *Theory of Plates and Shells*, 2nd Editio. McGraw-Hill College, 1959.

[52] A. F. Bower, *Applied Mechanics of Solids*, 483. CRC Press, Oct. 2009, vol. 112, pp. 211–212, ISBN: 9780429193323. DOI: 10.1201/9781439802489. [Online]. Available: https://www.taylorfrancis.com/books/9781439802489.

[53] J. Sirohi and I. Chopra, "Fundamental understanding of piezoelectric strain sensors," *Journal of Intelligent Material Systems and Structures*, vol. 11, no. 4, pp. 246–257, 2000, ISSN: 1045389X. DOI: 10.1106/8BFB-GC8P-XQ47-YCQ0.

[54] R. Caliò, U. B. Rongala, D. Camboni, M. Milazzo, C. Stefanini, G. de Petris, and C. M. Oddo, "Piezoelectric Energy Harvesting Solutions," *Sensors*, vol. 14, no. 3, pp. 4755–4790, 2014, ISSN: 1424-8220. DOI: 10.3390/s140304755. [Online]. Available: http://www.mdpi.com/1424-8220/14/3/4755/.

[55] J. W. Strutt, *The Theory of Sound, Volume II*. Cambridge University Press, 2011, ISBN: 9781139058094. DOI: 10.1017/CBO9781139058094. [Online]. Available: http://ebooks.cambridge.org/ref/id/CBO9781139058094.

[56] P. V. Kungurtsev and M. P. Juniper, "Adjoint-based shape optimization of the microchannels in an inkjet printhead," *Journal of Fluid Mechanics*, vol. 871, pp. 113–138, 2019, ISSN: 14697645. DOI: 10.1017/jfm.2019.271.

[57] R. Christensen, "Topology Optimization of Thermoviscous Acoustics in Tubes and Slits with Hearing Aid Applications," in *COMSOL conference Rotterdam*, 2017.

[58] T. Veijola, "Compact models for squeezed-film dampers with inertial and rarefied gas effects," *Journal of Micromechanics and Microengineering*, vol. 14, no. 7, pp. 1109–1118, 2004, ISSN: 09601317. DOI: 10.1088/0960-1317/14/7/034.

[59] V. Naderyan, R. Raspet, C. J. Hickey, and M. Mohammadi, "Acoustic end corrections for micro-perforated plates," *The Journal of the Acoustical Society of America*, vol. 146, no. 4, EL399–EL404, 2019, ISSN: 0001-4966. DOI: 10.1121/1.5129560.

[60] D. Homentcovschi, R. N. Miles, P. V. Loeppert, and A. J. Zuckerwar, "A microacoustic analysis including viscosity and thermal conductivity to model the effect of the protective cap on the acoustic response of a MEMS microphone," *Microsystem Technologies*, vol. 20, no. 2, pp. 265–272, Feb. 2014, ISSN: 0946-7076. DOI: 10.1007/s00542-013-1800-5. arXiv: NIHMS150003. [Online]. Available: https://www.ncbi.nlm.nih.gov/pmc/articles/PMC3624763/pdf/nihms412728.pdf%20http://link.springer.com/10.1007/s00542-013-1800-5.

[61] V. Cutanda-Henríquez and P. Juhl, "Modelling measurement microphones using BEM with visco-thermal losses.," *Joint Baltic-Nordic Acoustics Meeting*, 2012.

[62] W. M. Beltman, Y. H. Wijnant, and M. J. Nijhof, "An overview of models for viscothermal wave propagation, including fluid structure interaction," *Proceedings - European Conference on Noise Control*, pp. 3275–3280, 2008, ISSN: 22265147. DOI: 10.1121/1.2934166.

[63] H. A. Scarton and W. T. Rouleau, "Axisymmetric waves in compressible Newtonian liquids contained in rigid tubes: Steady-periodic mode shapes and dispersion by the method of eigenvalleys," *Journal of Fluid Mechanics*, vol. 58, no. 3, pp. 595–621, 1973, ISSN: 14697645. DOI: 10.1017/S0022112073002351.

[64] H. Tijdeman, "On the propagation of sound waves in cylindrical tubes," *Journal of Sound and Vibration*, vol. 39, no. 1, pp. 1–33, Mar. 1975, ISSN: 0022460X. DOI: 10.1016/S0022-460X(75)80206-9.

[65] V. F. Kozlov, A. V. Fedorov, and N. D. Malmuth, "Acoustic properties of rarefied gases inside pores of simple geometries," *The Journal of the Acoustical Society of America*, vol. 117, no. 6, pp. 3402–3411, 2005, ISSN: 0001-4966. DOI: 10.1121/1.1893428.

[66] T. Veijola, "A two-port model for wave propagation along a long circular microchannel," *Microfluidics and Nanofluidics*, vol. 3, no. 3, pp. 359–368, 2007, ISSN: 16134982. DOI: 10.1007/s10404-007-0159-2.

[67] Y. A. Cengel and J. M. Cimbala, *Fluid Mechanics: Fundamentals and Applications*, 3rd ed. 2014, p. 1031, ISBN: 9780073380322. [Online]. Available: http://highered.mheducation.com/sites/0073380326/information%7B%5C_%7Dcenter%7B%5C_%7Dview0/index.html.

[68] G. Karniadakis, B. Ali, and N. Aluru, *Microflows and Nanoflows: Fundamentals and Simulation*, Springer, Ed. 2005, vol. 29, p. 818.

[69] L. L. Beranek and T. Mellow, *Acoustics: Sound Fields and Transducers*, 2. Elsevier, 2012, ISBN: 9780123914217. DOI: 10.1016/C2011-0-05897-0.

[70] W. BELTMAN, "VISCOTHERMAL WAVE PROPAGATION INCLUDING ACOUSTO-ELASTIC INTERACTION, PART II: APPLICATIONS," *Journal of Sound and Vibration*, vol. 227, no. 3, pp. 587–609, Oct. 1999, ISSN: 0022460X. DOI: 10.1006/jsvi.1999.2356.

[71] E. C. Jordan and C. L. Andrews, "Electromagnetic Waves and Radiating Systems," *American Journal of Physics*, vol. 19, no. 8, pp. 477–478, Nov. 1951, ISSN: 0002-9505. DOI: 10.1119/1.1933056. [Online]. Available: http://aapt.scitation.org/doi/10.1119/1.1933056.

[72] J. Backus, "Acoustic impedance of an annular capillary," *The Journal of the Acoustical Society of America*, vol. 58, no. 5, pp. 1078–1081, Nov. 1975, ISSN: 0001-4966. DOI: 10.1121/1.380767. [Online]. Available: http://asa.scitation.org/doi/10.1121/1.380767.

[73] H. F. Olson, *Elements of Acoustical Engineering*. D. Van Nostrand Company, Inc., Apr. 1947, p. 539.

[74] J. B. W. Webber, "A bi-symmetric log transformation for wide-range data," *Measurement Science and Technology*, vol. 24, no. 2, 2013, ISSN: 13616501. DOI: 10.1088/0957-0233/24/2/027001.

[75] L. Kinsler, *Fundamentals of Acoustics*. Wiley, 1999, p. 560.

[76] G. P. Ward, R. K. Lovelock, A. R. Murray, A. P. Hibbins, J. R. Sambles, and J. D. Smith, "Boundary-Layer Effects on Acoustic Transmission Through Narrow Slit Cavities," *Physical Review Letters*, vol. 115, no. 4, pp. 1–5, 2015, ISSN: 10797114. DOI: 10.1103/PhysRevLett.115.044302.

[77] D. J. Inman, *Engineering Vibration*, 4th Editio. Pearson, 2013, ISBN: 0132871696.

[78] T. Gabrielson, "Mechanical-thermal noise in micromachined acoustic and vibration sensors," *IEEE Transactions on Electron Devices*, vol. 40, no. 5, pp. 903–909, May 1993, ISSN: 00189383. DOI: 10.1109/16.210197.

[79] J. M. Gere and B. J. Goodno, *Mechanics of Materials*, 4th. 2012, p. 1056.

[80] A. K. Chopra, *Dynamics of Structures*, 5th. Pearson, 2011, p. 992.

[81] H. Bachmann, W. J. Ammann, F. Deischl, J. Eisenmann, I. Floegl, G. H. Hirsch, G. K. Klein, G. J. Lande, O. Mahrenholtz, and H. G. Natke, *Vibration problems in structures practical guidelines*.

[82] W. C. Young and R. G. Budynas, *Roark's Formulas for Stress and Strain*, 7th Editio. 2001, p. 467.

[83] R. P. Paganelli, A. Romani, A. Golfarelli, M. Magi, E. Sangiorgi, and M. Tartagni, "Modeling and characterization of piezoelectric transducers by means of scattering parameters. Part I: Theory," *Sensors and Actuators, A: Physical*, vol. 160, no. 1-2, pp. 9–18, 2010, ISSN: 09244247. DOI: 10.1016/j.sna.2010.03.006. [Online]. Available: http://dx.doi.org/10.1016/j.sna.2010.03.006.

[84] X. Chen, Z. Zhang, S. Yu, and T. G. Zsurzsan, "Fringing Effect Analysis of Parallel Plate Capacitors for Capacitive Power Transfer Application," *2019 IEEE 4th International Future Energy Electronics Conference, IFEEC 2019*, 2019. DOI: 10.1109/IFEEC47410.2019.9015111.

[85] S. Park, X. Guan, Y. Kim, F. (X. Creighton, E. Wei, I. Kymissis, H. H. Nakajima, and E. S. Olson, "PVDF-Based Piezoelectric Microphone for Sound Detection Inside the Cochlea: Toward Totally Implantable Cochlear Implants," *Trends in Hearing*, vol. 22, pp. 1–11, 2018, ISSN: 23312165. DOI: 10.1177/2331216518774450.

[86] J. Dundurs and D. A. Sotiropoulos, "On stress conditions and computations at bi-material interfaces," *Computational Mechanics*, vol. 21, pp. 300–305, 1998.

[87] K. Lefki and G. J. M. Dormans, "Measurement of piezoelectric coefficients of ferroelectric thin films," *Journal of Applied Physics*, vol. 76, no. 3, pp. 1764–1767, Aug. 1994, ISSN: 0021-8979. DOI: 10.1063/1.357693.

[88] A. Arivazhagan and S. H. Masood, "Dynamic Mechanical Properties of ABS Material Processed by Fused Deposition Modelling," *International Journal of Engineering Research and Applications (IJERA)*, vol. 2, no. 3, pp. 2009–2014, 2012, ISSN: 1941-7020. DOI: 10.3844/ajeassp.2014.307.315. [Online]. Available: http://www.ijera.com/papers/Vol2%7B%5C_%7Dissue3/LZ2320092014.pdf.

[89] V. Sencadas, S. Lanceros-Méndez, and J. F. Mano, "Characterization of poled and non-poled β-PVDF films using thermal analysis techniques," *Thermochimica Acta*, vol. 424, no. 1-2, pp. 201–207, 2004, ISSN: 00406031. DOI: 10.1016/j.tca.2004.06.006.

[90] P. Gaudenzi, *Smart Structures: Physical Behaviour, Mathematical Modelling and Applications*. 2009, ISBN: 9780470059821. DOI: 10.1002/9780470682401.

[91] A. Vinogradov and F. Holloway, "Electro-mechanical properties of the piezoelectric polymer PVDF," *Ferroelectrics*, vol. 226, no. 1-4, pp. 169–181, 1999, ISSN: 00150193. DOI: 10.1080/00150199908230298.

[92] IEC 61094-8:2012, *Measurement Microphones. Part 8: Methods for Determining the Free-Field Sensitivity of Working Standard Microphones by Comparison*, 2012.

[93] M. Berzborn, R. Bomhardt, J. Klein, J. G. Richter, and M. Vorländer, "The ITA-Toolbox : An Open Source MATLAB Toolbox for Acoustic Measurements and Signal Processing," *German Annual Conference on Acoustics (DAGA)*, pp. 222–225, 2017.

[94] A. Farina, "Simultaneous measurement of impulse response and distortion with a swept-sine technique," *Journal of the Audio Engineering Society*, 2000.

[95] Stratasys, *ABSPlus-P430*. [Online]. Available: https://support.stratasys.com/en/materials/fdm-materials/absplus-p430.

[96] H. Schewe, "Piezoelectricity of Uniaxially Oriented Polyvinylidene Fluoride.," *Ultrasonics Symposium Proceedings*, vol. 1, pp. 519–524, 1982, ISSN: 00905607. DOI: 10.1109/ultsym.1982.197881.

[97] H. Miki, R. Sugii, Y. Kawabata, and S. Tsuchitani, "Lithographic micropatterning on the β-PVDF film using reactive ion etching aim for high-resolution skin sensors," *IEEJ Transactions on Electrical and Electronic Engineering*, vol. 14, no. 10, pp. 1575–1577, 2019, ISSN: 19314981. DOI: 10.1002/tee.22978.

[98] R.-A. Pallas and J. Webster, *Sensors and Signal Conditioning, Second Edition*. Tsinghua University Press, 2003, p. 608, ISBN: 7-302-07305-8.

[99] X. Wang, Z. Liu, and T. Zhang, "Flexible Sensing Electronics for Wearable/Attachable Health Monitoring," *Small*, vol. 13, no. 25, pp. 1–19, 2017, ISSN: 16136829. DOI: 10.1002/smll.201602790.

[100] Markforged, "Markforged Material Datasheet," p. 1, 2019. [Online]. Available: https://markforged.com/datasheets.

[101] M. Hannink, "Acoustic Resonators for the Reduction of Sound Radiation and Transmission," Ph.D. dissertation, 2007, p. 167, ISBN: 9789036524902. [Online]. Available: internal-pdf://76.27.248.245/Acoustic%20Resonators%20for%20The%20Reduction%20of%20Sound.pdf.

Acknowledgements

I would like to express my gratitude to my tutor, **Prof. Giovanni Verzellesi**, and my co-tutor, **Prof. Luca Larcher**, which supported me with helpful advices during this journey. Also, I would like to thank **Prof. Alessandro Bertacchini**, **Marco Lasagni**, **Gabriele Sereni** and **Michele Cotogno** for their constant assistance during laboratory work in Tecnopolo.

A special thank goes to **Paolo La Torraca** for his comprehensive support during the last three years of Ph.D. I would like to thank the present and past staff of the ELECOM Laboratory in Reggio Emilia: **Valerio Lunardelli**, **Behnood Dianat**, **Domenico Pepe**, **Giulia Orecchini**, and **Luca Aluigi**.

I would like to acknowledge the support of **Prof. Paolo Lugli** and **Giuseppe Cantarella** from the Free University of Bozen (Italy).

Also, I acknowledge ASK industries S.P.A. for financial support and technical assistance. Part of the research activity has been supported by the Italian Ministry of Economic Development fund for the sustainable growth, project "Vehicle Active Sound Management" under grant agreement B48I15000130008.

Most importantly, I would like to express my most sincere gratitude to **Giulia**. Thank you for your patience and your support in these years. Together with you, this journey has been enriched with meanings that would otherwise be unattainable.